UNIVERSITY OF OXFORD
D. PHIL. THESIS

Magmatism and Volcanism on Io

Daniel C. Spencer

Supervisors: Prof. Richard F. Katz and Prof. Ian J. Hewitt

A thesis submitted for the degree of Doctor of Philosophy

Department of Earth Sciences

University College

Declaration of Authorship

I, Daniel C. Spencer, declare that this project, titled 'Magmatism and Volcanism on Io' and the work presented in it are my own. I hereby certify that the work presented in this project is all my own unaided work and that all material obtained from published or unpublished sources of any type, including the internet, have been fully acknowledged at the proper point in the text and included in the list of references.

Signed:

Date: 01/04/2021

Abstract

Global volcanism has implications for planetary evolution far beyond the surface features that we observe. Magmatic and volcanic processes control the structural, thermal and compositional evolutions of the bodies where they operates. Jupiter's moon Io, the most volcanically active body in the Solar System, is an extreme 'end-member' that allows us to investigate the effects of planetary magmatism and volcanism in relative isolation of other processes. Previous research has generally investigated melting and magmatism within Io's partially-molten mantle separately from the volcanic systems in its lithosphere. In this thesis I present a suite of models that move beyond previous works by coupling mantle melting and magmatism to lithospheric evolution and volcanism. With this approach I show that magmatic intrusions within Io's lithosphere are a fundamental part of the global heat balance, delivering significant mass and energy to the lithosphere and controlling its thickness. As well as transporting heat, magmatism and volcanism also transport chemical species. With the inclusion of a simple chemical system, I show how magmatism and volcanism control Io's compositional evolution, leading to a layered mantle structure and the generation of ultra-high-temperature magmas in the deep mantle that can explain Io's highest temperature eruptions. Finally, the structural implications of magmatism and volcanism can be related to underlying tidal heating; I show how tidal heating distributions can be inferred from improved observations of long-wavelength lithospheric thicknesses and topography.

Acknowledgements

I am hugely grateful to Richard Katz for his support, insight, and vision throughout this project. Rich's mentorship has enabled me to grow as both a scientist and as a communicator. I am also grateful to Ian Hewitt, whose ability to cut to the heart of a problem has helped advance this project at some of its most difficult junctures. I also thank all the other scientists who have provided help and advice throughout this project: Philip England, Francis Nimmo, Laszlo Kestay, David May, Tim Lichtenberg, John Rudge, Katherine de Kleer, Ray Pierrehumbert, John Spencer, James Bryson, David Rees Jones, Sally Gibson, and Jon Wade.

I thank my examiners, Jerome Neufeld and Jon Blundy, for their time in reading my thesis, and for the fascinating discussion they provided during my viva voce.

The work in this thesis would not have been possible without my friends at home and in Oxford. In particular I thank Thomas Breithaupt for being my constant ally throughout, from teaching me MATLAB to gossiping over coffee, and everything in between. I also thank Nick Trundle, who has cheered me on from day one. To list but a few of the many other friends who have supported me in my time at Oxford I thank Nik, Leo, Rellie, workshop (fit) James King, Sophie, Ellen, Oli, Bernd, Claire, and Sam.

I thank my family, who always provided an ear when I needed to moan, and celebrated all of the small victories. They were, and continue to be my rock.

My thanks goes to the Department of Earth Sciences and University College for assisting me throughout my DPhil, providing the solid foundation upon which I could conduct this work. I also specifically thank my funders, the Oxford-Radcliffe Scholarship (and all of its donors) and the Department of Earth Sciences.

Most importantly, I thank my partner Emily. Her love and support has got me through my lowest points, and accompanied me at my highest. I simply couldn't have done it without her. I also give my thanks to Mandy, Nick, and Tom for taking me in when lockdown hit; I couldn't have asked for a better setting to conclude this project than next to Emily in their dining room.

Contents

CHAPTER 1

Introduction

Heat transport mechanisms play a pre-eminent role in the evolution of planetary bodies. Volcanism, perhaps the most dynamic of these, is not merely the eruption of molten rock onto the surface of a body, but is also a pathway for heat and chemical species to move from the interior to the exterior. Planetary-scale volcanic activity also allows the transfer of large amounts of energy, and is thought to have played an important role in the evolution of the early Earth (Moore and Webb, 2013) and Venus (Moore et al., 2017), exoplanets (Lourenço et al., 2018), planetesimals, and icy moons like Europa and Enceladus (Keane et al., 2020). By affecting large proportions of planetary interiors, far below the surface features that we observe, planetary volcanism leads to compositional evolution and the formation of atmospheres. Indeed with its role in the generation of Earth's atmosphere, volcanism contributed significantly to the emergence of life. Conversely, volcanism on Venus has lead to what appears to be a thoroughly uninhabitable surface. Understanding the role that volcanism plays in the evolution of planetary interiors and surfaces is of vital importance to understanding how it may facilitate or prevent the emergence of habitable environments.

This thesis focuses on the most volcanically active body in the Solar System, Jupiter's moon

Io. Slightly larger than our Moon, Io is an extreme ‘end-member’ that allows us to investigate magmatism and volcanism in relative isolation from other processes. With virtually no atmosphere, no plate-tectonics, and a relative wealth of observations, it is the perfect staging point for an investigation into how magmatism and volcanism control planetary evolution. By understanding how these processes dominate Io’s structural, thermal, and chemical evolution, we can start to understand their more transient effects throughout the Solar System and beyond.

Io is also particularly interesting because of the source of the heat that drives its volcanism: tidal heating. Tidal heating is a process of fundamental importance in the Solar System (de Kleer et al., 2019b), not least because it has generated water oceans inside Enceladus (Spencer and Nimmo, 2013) and Europa (Carr et al., 1998) that potentially harbour life. Io’s volcanism provides a direct window into its interior, allowing a joint investigation of magmatism, volcanism, and tidal heating in a way not possible with any other body.

In this chapter I will introduce Io, giving a brief history of its observation and presenting its key characteristics together with the works that have described and constrained them. I will then discuss some of the main open questions in the Io research landscape, covering those that I will tackle in this thesis, as well as those that I will not. I will conclude with an outline of this thesis.

1.1 The Galilean satellites of Jupiter

The Galilean satellites are Jupiter’s four largest moons: Io, Europa, Ganymede, and Callisto, so named for their discovery by Galileo Galilei in the 15th Century. The Jupiter system is often informally referred to as a mini-solar-system because of the similar trends that can be observed between the Jovian satellites and the Solar System planets. The Galilean satellites are progressively enriched in volatiles with distance from Jupiter, in a similar manner to the increasing volatile content of bodies with distance from the Sun, yielding a density decrease with distance from Jupiter (table 1.1). The Galilean satellites also experience progressively smaller gravitational tides with distance from Jupiter. Io is the closest Galilean satellite to Jupiter, and has received enough internal heating throughout its history to differentiate into an iron-rich core and a silicate shell. Indeed present day tidal forces result in its pervasive silicate melting and surface volcanism.

1.2 A brief history of exploration

1.2.1 The Voyager 1 era

The extreme tidal heating of Io was first predicted by Peale et al. (1979), who proposed that its Laplace resonance with Ganymede and Europa (see section 2.1) — first discovered in 1771 by Pierre-Simon Laplace — would lead to significant internal heating. They were proven spectacularly correct a few months later when *Voyager 1* first observed Io's volcanic terrains and over 10 km high mountains (left hand side of figure 1.1, Morabito et al., 1979).

Voyager 1 revealed that Io's surface is rich in sulphur allotropes and sulphur dioxide (Smith et al., 1979). This led to debate as to whether Io's surface was dominantly silicate (Carr et al., 1979) or composed of primary sulphur compounds (Sagan, 1979). After infra-red data revealed the high surface heat flux however, it was established that sulphur compounds would be too weak to support Io's topography, and the silicate nature of the near-surface was established (Clow and Carr, 1980). As the flight of NASA's flagship Jupiter orbiter *Galileo* approached, eruption temperatures were constrained to be over 1000 K, well above the boiling point of sulphur (Blaney et al., 1995), and as Lopes and Spencer put it "the case for silicate volcanism as the dominant mechanism at work in Io's hot crust was soundly established" (Lopes and Spencer, 2007, p.27).

Table 1.1: Bulk physical properties and orbital characteristic of the Galilean satellites

Galilean satellites	Mass (10^{20} kg)	Radius (km)	Mean density (kg/m^3)	Semi-major axis (10^3 km)	Orbital period (days)	Orbital eccentricity
Io	893.2	1821.5	3530	421.8	1.769	0.004
Europa	480.0	1560.8	3010	671.1	3.551	0.009
Ganymede	1481.9	2631.2	1940	1070.4	7.155	0.001
Callisto	1075.9	2419.3	1830	1882.7	16.689	0.007

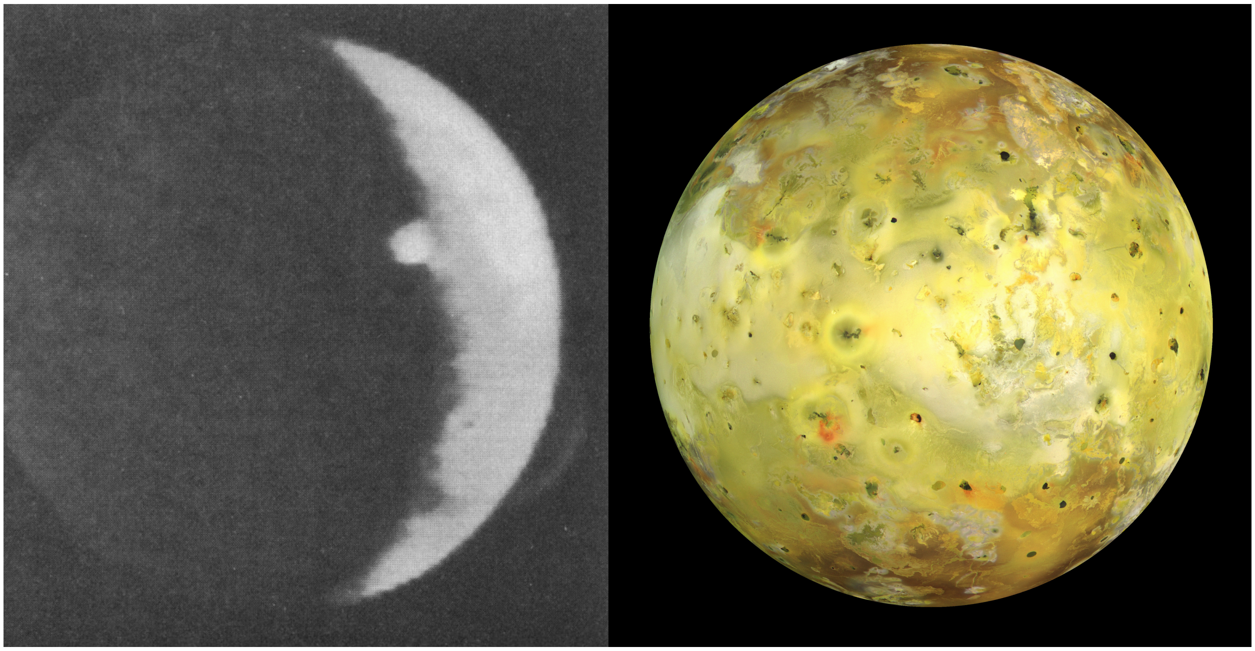

Figure 1.1: Left: ‘The discovery photo’ taken by *Voyager 1*, showing the first evidence of active volcanism on an extra-terrestrial body (Morabito et al., 1979). Note that *Voyager* took significantly higher resultion images than that shown here. Right: True colour image taken by *Galileo* in 1999.

1.2.2 The Galileo era

The *Galileo* mission revolutionised Io research (right hand side of figure 1.1). Initial *Galileo* observations indicated widespread ultramafic volcanism, estimating the Pillan eruption to be 1870 ± 25 K (McEwen et al., 1998). Over time these temperatures were revised down to ~ 1600 K (Keszthelyi et al., 2007), but nonetheless it became clear that Io's eruptions are dominantly mafic to ultramafic silicate lavas. Again we can turn to Lopes and Spencer who noted (Lopes and Spencer, 2007, p.292)

> "...so far we have no proof that sulfur-dominated volcanic flows exist. This question can probably only be answered by high-resolution spacecraft observations capable of measuring the peak temperatures of active flows."

Indeed the following decade provided no evidence of primary sulphur volcanism, despite sulphur's obvious role in providing the yellow, red, and green hues that dominate the surface (figure 1.1).

In many regards we are still in the *Galileo* era of Io observation, despite the end of the *Galileo* mission in 2003. No new mission has provided anywhere near as much data on Io as *Galileo* did. Earth-based observational campaigns are, however, enabling continued monitoring and cataloguing of eruption events, in particular the 2013–2018 observational campaign utilising the Keck and Geimini N telescopes in Hawaii (de Kleer et al., 2019a). Improving Earth-based observations are providing significant insight into secular variation in volcanic activity, and with new observational techniques (e.g., Davies et al., 2016, 2017) robust lava temperature and composition data are within reach. These advances, together with new missions to the Jupiter system (*JUICE*, *Europa Clipper*, and the proposed *Io Volcano Observer*), demonstrate that we may be about to enter a new era of Io research.

1.3 The composition and basic structure of Io

A good starting point for a geophysical description of a planetary body is in considering its bulk composition and structure. The predominantly mafic to ultramafic character of Io's volcanism, and the silicate nature of its lithosphere were well established before the flight of *Galileo*. Gravity data from *Galileo* placed the average density at ~ 3528 kg/m^3, which implies a silicate/iron bulk composition. Classic solutions for the shape and gravity field (quantified by the tidal Love numbers, see section 2.1) of a homogenous body are inconsistent with Io's observed shape and gravity field, which implies that it has differentiated into an iron-rich core and a silicate mantle.

Whilst we can ascertain that Io has differentiated, the sizes and compositions of the core and mantle are not uniquely constrained. Moore et al. (2007) presented the family of results for core/mantle densities and sizes that are compatible with Io's mass and Love numbers (reproduced in figure 1.2). The range of possible core densities comes from the potential incorporation of a light element into the iron core. This light element is typically assumed to be sulphur given the abundance of sulphur at the surface. The more sulphur there is in the core, the lower its density and so the greater its size must be in order to match the mass and Love number constraints. It is most likely that the core density lies between that of pure Fe and FeS (figure 1.2), and throughout this thesis I take a commonly used intermediate value of 7640 kg/m^3 (Bierson and Nimmo, 2016). This corresponds to a core radius of ~ 700 km.

Present shape and gravity data can only tell us this much because as more layers are added to a model, the solutions become less and less constrained. The density of Io's mantle is constrained to be between about $3000 - 3300$ kg/m^3, assuming that it does not have an extremely large and sulphur rich core (figure 1.2). This is a relatively strong constraint on density, but given that we don't know the temperature it is not straightforward to turn this into a composition. Sohl et al. (2002) used equation of state data and an assumption of a

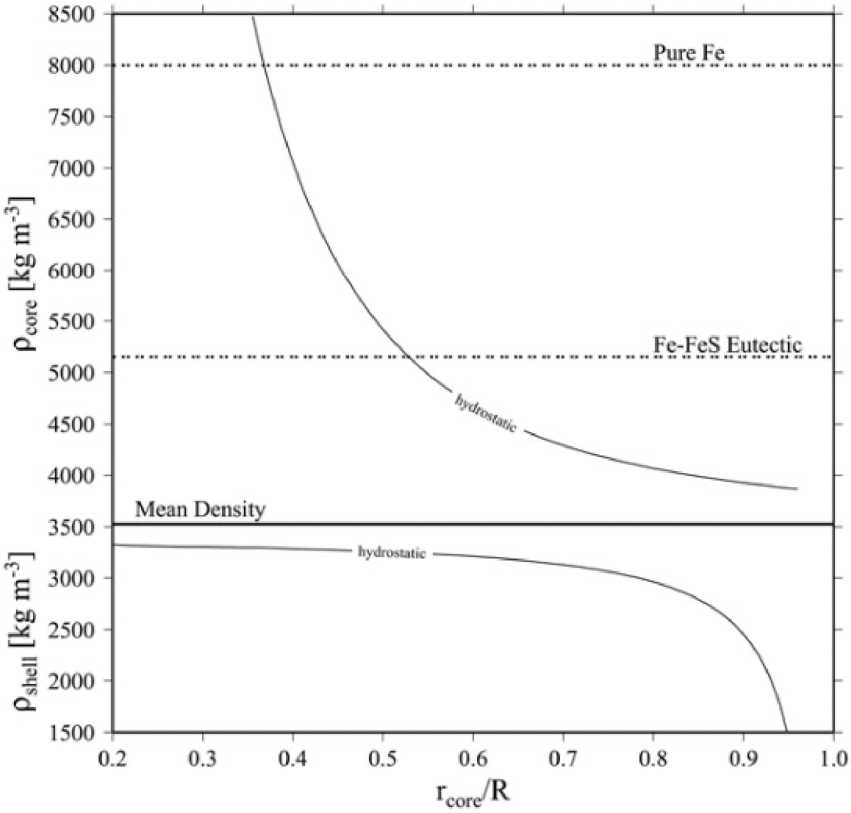

Figure 1.2: Two-layer models of Io that are consistent with observed Love numbers and the bulk density, reproduced from Moore et al. (2007). These models assume that Io's shape is roughly hydrostatic, consistent with the high surface heat flow.

pure olivine mantle to estimate the forsterite content of the mantle to be between 76 and 85 wt%, but this is about as far as the field has come in this direction. Simply put, better gravity data are required to further constrain interior structure based on these shape/gravity techniques.

1.4 Surface volcanism on Io

Having broadly established what Io is made of and its basic structure, we can turn to a discussion of the most obvious process controlling its evolution: volcanism. The surface is crater free and covered in volcanic features, indicating ongoing global resurfacing. There are three main areas that, together, describe Io's volcanism. The first — which I have already touched on — is the temperature and composition of erupta. The other two areas consider the style of volcanic activity, and the distribution of volcanic activity. In this section I will discuss all three, providing a picture Io's volcanic activity.

1.4.1 Eruption temperatures and compositions

As I have discussed, it appears that Io's lavas are mafic to ultramafic, but discerning their temperatures is not straight-forward. The difficulty in ascertaining the erupta temperatures ultimately comes from the difficulty in observing the cooling history of flows. Infra-red data are used to estimate lava temperatures through the application of a cooling model. With some assumptions about the style of volcanism (see below), a time-series of infra-red measurements can be fit with a cooling model, which can be used to extrapolate back to an eruption temperature (e.g., Keszthelyi et al., 2007). In order to do this requires a somewhat serendipitous eruption that is within line-of-sight of a ground-based infra-red telescope at a number of points early after lava emplacement. The cold surface of Io makes this even more difficult as lavas cool extremely quickly upon eruption. The complexity of this procedure is why works can frequently only present lower limits on eruption temperatures.

Despite these complications, there does appear to be significant variability in eruption temperatures. Most eruptions are consistent with basaltic-like temperatures on the order of 1300 K (McEwen et al., 1998), but rarer 'outburst' eruptions (see below) appear to have much higher temperatures, with lower bounds as high as 1900 K (de Kleer et al., 2014). Whether this is a true dichotomy or if temperatures range between these two values is unclear, it is nonetheless apparent that Io's volcanism is hot, mafic, and non-uniform.

1.4.2 Styles of volcanic eruption

There are three predominant eruption styles observed on Io. The first are the extensive flow dominated eruptions. These eruptions emplace magma relatively slowly over the course of a number of years and generate huge flow fields hundreds of kilometres in extent. The Amirani flow field (figure 1.3) is an example of one of these. New eruptions are seen at the edges of the flow field where lava breaks through the cooling crust. Magma is presumably fed to these features through lava tubes (Davies et al., 2017). Given the huge areal extent of these features, it seems likely that they play a significant role in resurfacing. The temperatures of these flow dominated eruptions seem to be consistent with terrestrial basalts (Davies et al., 2017).

The second type of eruptions are termed 'intra-patera' eruption (Lopes and Spencer, 2007). These eruptions are confined within volcanic paterae, which are similar to terrestrial calderas (Radebaugh et al., 2001) and are found in great number across Io (most of the dark 'spots' seen on Io's surface are at the sites of these paterae, figure 1.1). Intra-patera eruptions tend to be overturning lava lakes with quasi-periodic activity (de Kleer and de Pater, 2016). Similar to flow dominated eruptions, intra-patera eruptions seem to be consistent with basaltic temperatures (de Kleer et al., 2017). Loki is the archetypal intra-patera volcano and is the most eruptive volcano in the Solar System (de Kleer et al., 2017), contributing about 15% of Io's global heat loss (Spencer et al., 2000). Intra-patera eruptions can occur with or without associated dust/gas plumes, but the effusive parts of these eruptions appear to be well confined within the paterae. This implies that these eruptions do not significantly contribute to resurfacing despite their important role in global heat loss.

The third and final type of volcanic activity observed on Io are the explosive eruptions. These eruptions tend to occur at paterae or fissures, but are much shorter lived than intra-patera eruptions, with a large amount of energy going toward the formation of large pyroclasic plumes. These plumes can reach > 200 km in height above the surface of Io (as seen in the

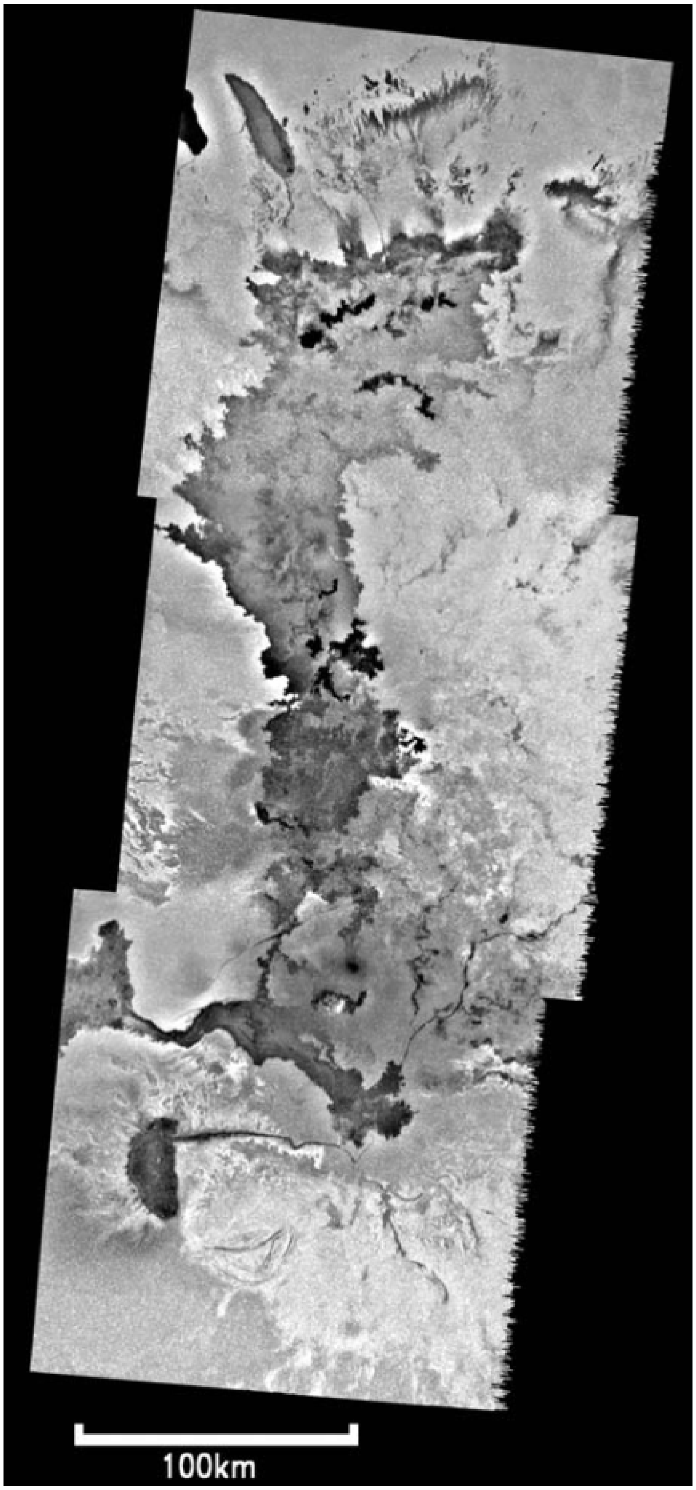

Figure 1.3: The Amirani flow field, imaged by the *Galileo* solid-state imager (SSI) in Feb 2000.

'discovery photo' in figure 1.1). These explosive eruptions produce both pyroclastic deposits as well as dark lava flow fields (Lopes and Spencer, 2007). It is these eruptions that result in the ring structures seen on Io's surface, with plume material following ballistic trajectories. The rare, most powerful explosive eruptions are termed 'outburst' eruptions, and are defined as events that double the global infra-red flux at the $4.5-5.0$ µm wavelength range (de Kleer et al., 2014). The highest eruption temperature estimates come from these outbursts, with the present highest estimate being ≥ 1900 K (de Kleer et al., 2014), indicative of ultramafic, komatiite like eruption compositions (Williams et al., 2000).

1.4.3 Volcanic activity distributions

A large amount of work has been dedicated to analysing the distribution of Io's hotspots, volcanic features, and volcanic activity. These works generally analyse a catalogue of eruption events, or a catalogue of eruption features, in order to determine if there are regions with higher rates of volcanism (e.g., Ross et al., 1990; Kirchoff et al., 2011; Hamilton et al., 2013; Rathbun et al., 2018; Cantrall et al., 2018). A lot of time is spent deciding what features/events to include in these analyses with relatively little consensus in the community both on what features should be included and on what activity distributions they imply. On the one hand, by counting volcanic units and constructs, formerly eruptive regions could be identified, but on the other hand, if eruptive features are erased by subsequent eruptions, more active regions may not show more features (these trade-offs are discussed in Rathbun et al., 2018).

Some recent works propose that there are higher rates of volcanic activity near the equator (Cantrall et al., 2018), with others proposing the opposite, advocating greater activity at the poles (Rathbun et al., 2018). Part of the difficulty here is that there is a significant observational bias against polar observations, which cannot generally be observed with ground-based systems. Rathbun et al. (2018) included new data from the *Juno* mission, which is in an initially polar orbit around Jupiter and so can make occasional observations of Io's poles, which goes some way to addressing this observational bias. Ultimately, far more observations of the polar regions are needed to accurately ascertain whether any latitudes on Io are systematically less active. Certainly there does not appear to be a systematic region that is inactive, and so at least at leading order we can say that the volcanism is global.

Considering the temperatures, compositions, eruption styles, and global distribution of Io's volcanism we can start to piece together a picture of its global, large scale volcanism. Io's volcanism is mafic to ultramafic, with a range of explosive and effusive activity. Large flow fields and explosive eruptions appear to do most of the resurfacing on Io, but intra-patera eruptions may be dominating heat flow. Sulphur clearly plays a role in the volcanic systems, but it is not necessarily clear how deep this association goes. How this picture of volcanism that we have obtained over the last 40 years relates to long-timescale evolution is a significant open question; as is the role of sulphur. In this thesis I will address some of the broader questions about long-timescale resurfacing, but there are also a multitude of interesting volcanological research avenues that could be explored in this system.

1.5 Tidal dissipation

Tidal dissipation (or tidal heating) is the process that is supplying energy to Io, and thus is the driving force behind its activity. This fundamental planetary process is an important component of this thesis and I will spend some time discussing details of its operation in Chapter 2, but here I will provide an overview of its importance to Io.

Tidal dissipation occurs when a satellite undergoes time-dependent deformation. In the case of Io this time dependent deformation is caused by its eccentric orbit, which is maintained by its Laplace resonance with Europa and Ganymede. There are different ways to calculate the rate of tidal heating within a body, and I will cover these in Chapter 2, but for now it is enough to know that the total heating rate can be estimated from orbital characteristics and the gravitational Love number. Lainey et al. (2009) estimated the total heating rate in Io to be $9.33 \pm 1.87 \times 10^{13}$ W. If Io is losing heat at the rate that it is dissipated (we believe it is, see section 1.6.2), and if this heat is lost uniformly across at the surface, it corresponds to a surface heat flux of ~ 2.4 W/m^2, which is about two orders of magnitude greater than the average surface heat flux on Earth. It is important to note, however, that a number of assumptions go into the the calculation of tidal heating rates (as I shall discuss in section 2.1) and so whilst there is a relatively strong community consensus on this value for the heating rate, it should be treated with some caution.

The total tidal dissipation rate is of course of great importance in the Io story, but so is the distribution of heating. The distribution of tidal heating in a body depends on its internal structure; this is a fundamental point that I will discuss in Chapter 2 and at a number of other points in this thesis. For now it is important to understand that there are two competing models for the distribution of tidal heating within Io. The first assumes that heating is distributed throughout the silicate mantle, with a maximum near the core and a minimum at the surface; this is the distribution expected for a solid, differentiated body and I will refer to it as the 'mantle heating model'. The second model assumes that heating is concentrated within a dissipative asthenosphere just beneath Io's lithosphere, which I will refer to as the 'asthenosphere heating model'. This asthenosphere heating model would be expected to be relevant if Io has a dissipative, low viscosity layer beneath its lithosphere such as a magma ocean — a feature that has been proposed in a number of works (e.g., Khurana et al., 2011) and that I will discuss below. If heating is distributed through the mantle, more dissipation occurs at the poles, and is expected to produce high polar heat fluxes, whereas if heating is concentrated in an asthenosphere, more dissipation occurs at the equator, and is expected to produce high equatorial heat fluxes.

The works analysing the distribution of Io's volcanic activity that I described above have generally done so with an aim of distinguishing these different dissipation models. If there was a bias of volcanic activity toward the equator this would favour an asthenosphere heating model, whereas a bias of activity to the poles would favour a mantle heating model. Unfortunately, as I have discussed there is little consensus in the community on this question and so volcanic activity distributions cannot currently be used to constrain tidal heating distributions. The distribution of tidal heating and its relationship to interior structure is one of the most significant open questions surrounding Io, and indeed planetary science in general.

1.6 Heat transport in Io

The heat transport processes that operate in planetary interiors exert a pre-eminent control on interior structure. Earth's plate tectonics for example — which controls so much of how the outer layers of the Earth operate — is a manifestation of mantle convection, which is the primary means of heat transport in Earth's mantle. By understanding what heat transfer processes are operating in the different regions of a planetary body, we can build a picture of a body's interior structure and dynamics. Tidal dissipation supplies energy to Io, but it is its action alongside the heat transfer processes operating that determine interior structure.

1.6.1 Lithospheric heat transport

Early in the observational history of Io it was clear that its prodigious surface heat flow could not be supported by conduction. The > 10 km mountains first observed by *Voyager 1* could not be supported by the ~ 5 km lithosphere that conduction would imply. O'Reilly and Davies (1981) provided a solution to this problem, proposing the 'heat-pipe' mechanism for heat transport through Io's lithosphere. Volcanic systems provide a rapid, direct means for molten rock to export heat across the lithosphere, upon which it radiates its energy to space.

The continual eruption of this material onto the surface buries the lithosphere downward, producing a lithospheric conveyor belt that advects the cold surface temperatures ($\sim$ 150 K) into the interior. This eruption and burial process leads to the growth of a thick and cold lithosphere capable of supporting Io's mountains.

Strong support for heat-piping lies in the observation that the majority of heat flow from Io's surface comes from volcanic features (Davies et al., 2015). We can estimate the Péclet number in Io's lithosphere (which we'll take to be $h \sim 75$ km thick for this purpose) assuming a resurfacing rate of $v \sim 1.25$ cm/yr (obtained from assuming all heat lost from Io is volcanic, with a temperature drop of 1350 K) and a thermal diffusivity of $\kappa = 10^{-6}$ m^2/s; this yields a Péclet number ($\mathrm{Pe} = vh/\kappa$) of $\sim$ 30, implying that advective heat transfer is about an order of magnitude faster than conductive heat transport. The importance of advective heat transfer implies that most of the lithosphere should be cold and capable of supporting significant topography

As well as facilitating the growth of a lithosphere capable of supporting Io's mountains, heat-piping also explains how these mountains form. The eruption and burial process is happening on a sphere, which means that as the surface is buried, its area must reduce. The burial of the lithosphere causes significant lateral compression, which results in thrust faulting that facilitates the reduction in area, and causes the growth of high mountains (McKinnon et al. (2001), figure 1.4). This hypothesis for mountain building has been refined over time to account for volcanic heat fluxes, thermal stresses, and near-surface extension (Kirchoff and McKinnon, 2009; Kirchoff et al., 2011, 2020), but has remained largely unchanged.

1.6.2 Mantle heat transport

The dominant heat transfer mechanisms within Io's mantle are not as clear as those within its lithosphere. The eruption and burial process described in section 1.6.1 requires a significant magma flux out of the mantle, but does not constrain where this magma forms or how it

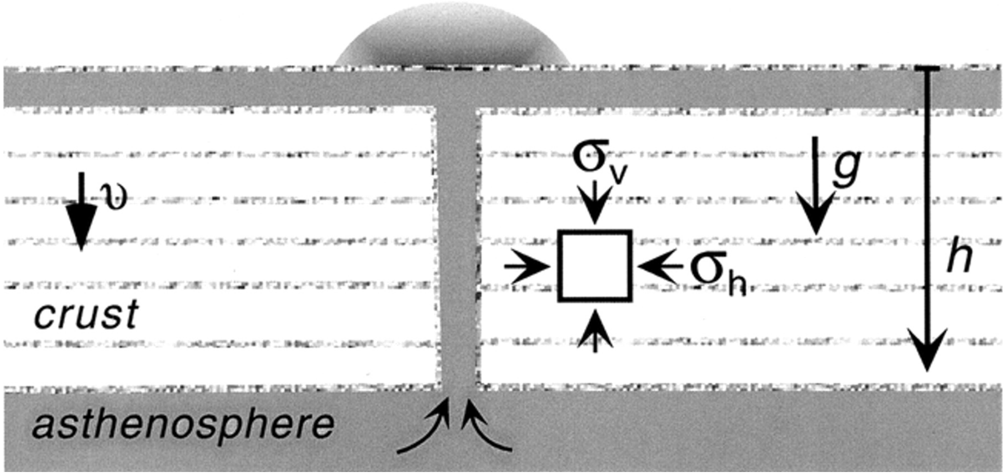

Figure 1.4: Schematic of heat piping and the lateral compressional stress σ_h caused by the eruption and burial process, reproduced from McKinnon et al. (2001).

reaches the base of the lithosphere. Io's estimated tidal heating rate of $\sim 1 \times 10^{14}$ W (Lainey et al., 2009) appears to be in good agreement with total amount of energy being lost from Io's surface. This has been used to infer that Io is in thermal steady state. However, as I noted in section 1.5 there are a number of assumptions involved in the calculation of tidal heating rate that complicate this issue. We do not know whether the heating rate is changing over time, and it is possible (though perhaps unlikely) that the apparent match between the estimated heating rate and the observed surface heat flux is a coincidence. Nonetheless, the assumption of a thermal steady state has dominated the research landscape, and in this thesis I will also make this important and fundamental assumption. It is important to keep in mind, however, that the question of the total tidal heating rate within Io is not fully settled, and won't be until we have a much firmer grasp on its internal structure.

If Io is in thermal steady state then the heat transfer processes in the mantle must be in equilibrium with the tidal dissipation rate, which is not guaranteed given the expected feedbacks between heat transport, rheology, and dissipation (see Chapter 2). Moore (2003) looked for such equilibria using a tidal heating model and heat transport calculations (figure 1.5). One potential heat transport mechanism is convection, which is the heat transport process that dominates in Earth's mantle. In convective heat transport, buoyant material

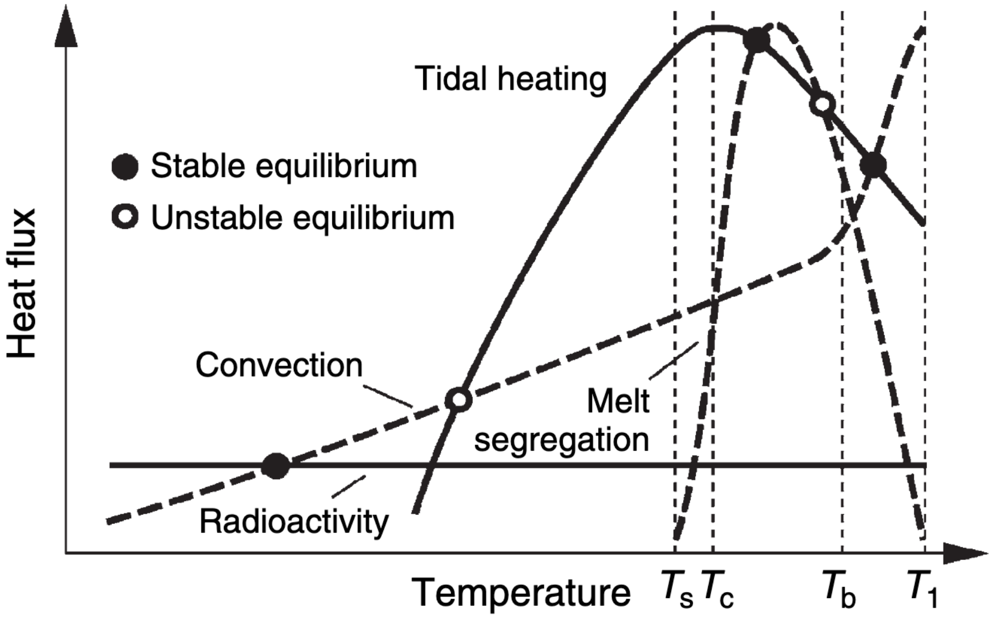

Figure 1.5: Cartoon showing possible thermal equilibria between heat production processes and heat transport processes in a tidally heated body, reproduced from Breuer and Moore (2015). Equilibria between tidal heat production and convective heat transfer cannot match observations of Io's surface heat flux. At temperatures where tidal heating matches the surface heat flux, convection is too inefficient to transport the generated heat. Magmatic segregation can transport energy efficiently at low melt fractions, at which tidal heat production is also high. It is these arguments that have lead to the paradigm view that heat transport in Io's mantle is dominated by magmatic segregation.

transports heat upward, and cold material sinks to replace it. Moore and Webb (2013), however, proposed that when convection is in equilibrium with tidal heating it falls orders of magnitude short of producing the observed surface heat flux. Convective heat transport increases with temperature due to the decreasing viscosity, but tidal heating has a parabolic relationship with temperature (section 2.1), with a maximum just above the solidus (figure 1.5). At temperatures where dissipation is high and can match the observed surface heat flux, the mantle is too viscous to transport the generated heat by convection. This causes the temperature to increase and dissipation to reduce towards the equilibrium value (figure 1.5). Moore (2003) proposed that instead of convection, another more efficient heat transport mechanism must be operating that can transport the observed surface heat flux at lower mantle melt fractions and temperatures. Moore (2003) proposed that buoyant magmatic segregation could be this mechanism.

Buoyant magmatic segregation is a process of central importance to this thesis. I will introduce it fully with an overview of two-phase flow in Chapter 2. For now a qualitative understanding is sufficient; in a magmatically segregating system, heating causes the production of magma, which segregates upward due to buoyancy. Segregating magma carries sensible and latent heat upward, transporting heat out of the deep interior.

The heat transport processes that dominate in Io are thus relatively well understood. Magmatic segregation transport energy out of the partially molten mantle, and volcanic systems carry this energy to the surface. It is important to point out that if a magma ocean is present it may complicate this picture. Heat transport in a magma ocean occurs by turbulent convection, and the importance of such a layer will depend on how much energy is directly dissipated within it. It is also important to note that whilst solid-state convection cannot dominate heat transport in Io's mantle, this does not mean that convection does not occur. There may be thermal or compositional drives for convection that are not removed by the segregation of magma, in which case solid-state convection may exert an important control on Io's internal structure.

1.7 Io as a spherically symmetric body

In this introduction I have spent a lot of time discussing broad, leading-order observations, some time discussing large-scale variations, and very little time discussing high-fidelity, small-scale features. When discussing volcano distributions I noted that a lot of effort has been dedicated to finding patterns in Io's volcanism, but perhaps the simplest conclusion we can draw is that the entire surface is volcanically active. Taking another look at the *Galileo* true-colour image in figure 1.1 we can see that volcanic features cover the entire surface. There are no craters, which implies that resurfacing is global on long-timescales. Indeed the crater free nature of Io's oldest surfaces (the regions of greatest mass wasting) means that they must be younger than $10^6 - 10^7$ years (Lopes and Spencer, 2007). It is also important to remember that at leading order, tidal heating is degree-1 (spherically symmetric). There is certainly nuance in the distribution of heating, and a lot of questions would be addressed by a close knowledge of this distribution, but fundamentally, heating is taking place throughout. There is a great deal of small-scale complexity on Io, but at leading-order, it appears to be a spherically-symmetric body.

As observational fidelity improves, there is a natural drive to build models that investigate increasingly detailed features. Importantly, however, there are a number of open questions surrounding Io's leading order structure, as I shall discuss in the next section. In this thesis (with the exception of Chapter 5) I will make the fundamental assumption that at leading order Io can be treated as a spherically symmetric body. The heterogeneity that is seen on the surface, as well as that expected within the interior, is then considered to be a deviation from this spherical symmetry. In this context, Io's deviations from spherical symmetry can only be understood once the leading order structure is ascertained.

1.8 Open questions

The observations of Io that have been accumulated since *Voyager 1*, together with the now over 40 years of literature surrounding them, paint an intriguing picture of an extraordinarily active world. Nonetheless there are still a number of important open questions. Some of these questions are perhaps out of reach without a dedicated mission (Keane et al., 2020), but some are beginning to be tackled as our observational catalogue and the fidelity of measurements grows. In this thesis I will tackle a small subset of the many interesting avenues of research that Io presents. In this section I will take some time to discuss the primary open questions surrounding Io; I will discuss both those that I will address in this thesis, and those that I will not. It goes without saying that this will not be an exhaustive account of every open question in Io research, and I will focus specifically on geodynamics, structure, and volcanology, not touching on the rich magnetosphere and plasma-physics literature.

1.8.1 The presence or absence of a magma ocean

The single biggest open question surrounding Io is whether it hosts a global, sub-surface magma ocean. There has been an unfortunate lack of clarity in the literature on the definition of a magma ocean (it has been used to describe melt fractions as low as 20%, significantly below matrix disaggregation), but here and throughout this thesis I will consider a magma ocean to be a global layer with melt fractions above disaggregation ($\sim 35\%$) that behaves as a fluid on short timescales. Khurana et al. (2011) used magnetometer data to infer the presence of a global melt layer beneath Io's lithosphere. A conducting fluid layer results in induction in the vicinity of Jupiter's strong magnetic field; this induction can be detected by magnetometers such as that on *Galileo*. Khurana et al. (2011) proposed that a melt fraction of at least 20% over a 50km region was needed to satisfy observations, and whilst I noted above that a 20% melt fraction layer should not be considered a magma ocean, they did favour higher melt fractions exceeding disaggregation. This observation has been challenged in a number of works; Roth et al. (2017) proposed that observations of Io's aurora hotspots are inconsistent with the presence of a magma ocean, and Blöcker et al. (2018) noted that plasma interactions in Io's atmosphere can provide an alternate explanation for induction measurements. This question is being actively investigated by a number of groups and little consensus has yet been reached.

The presence of a magma ocean would raise a number of questions about Io's interior dynamics (as well as for dissipation structure). If this layer is buoyant, how are such vast quantities of magma prevented from erupting all at once, and how can a fluid magma ocean explain the apparent variability in erupted temperatures and compositions? Within this thesis I will not directly tackle the question of whether a magma ocean is present, but I will make some related points. Foremost of these is that I will ask by what mechanisms could a high melt fraction layer within Io be generated. By developing our understanding of magma dynamics within Io, I hope to parallel the advances in magnetohydrodynamics and allow us to move toward an answer to this fundamental question. The fact remains, however, that the best way to ascertain whether a magma ocean is present is to make new geophysical measurements with an orbiting spacecraft (Keane et al., 2020).

1.8.2 Io's dissipation structure

The presence or absence of a magma ocean on Io has significant implications for the distribution of tidal heating. The mechanisms by which tides cause heating are different in solid bodies (e.g., Segatz et al., 1988) and fluid bodies (e.g., Tobie et al., 2005), but it has been argued that a fluid magma ocean in Io would lead to a concentration of heating within such a layer (e.g., Bierson and Nimmo, 2016). This is the origin of the two opposing dissipation models I discussed above. The dissipation structure will exert a leading order control on interior structure and dynamics and so is of fundamental importance to understanding Io's interior. Further, by understanding how tidal heating operates on Io we can gain insights into its operation on other bodies such as Europa, and this relevance is increased if a sub-surface "ocean" is present on Io as it is on Europa.

As I have discussed, some works have tried to address this question by observing the distribution of volcanic activity on Io (e.g., Ross et al., 1990; Kirchoff et al., 2011; Hamilton et al., 2013; Rathbun et al., 2018; Cantrall et al., 2018). Different distributions of tidal heating predict different surface variations in volcanic activity, with asthenosphere dissipation favouring high equatorial activity. The lack of a consensus in this area is perhaps telling. What magnitude of variability in surface eruption rates are we really expecting, and have we been observing Io for long enough to see such variability? Indeed it is unclear whether the short timescale of our observations, the bias against polar observations, and more generally the possibility of lateral magma flow, allow us to utilise this approach. The best way to understand Io's dissipation structure is to develop our understanding of how tidal heating operates in complex three-dimensional bodies, as well as to better understand how dissipation couples to interior dynamics. In this thesis I will spend some tackling this last point, particularly in Chapter 5.

1.8.3 Volcanic resurfacing

A fundamental assumption in the heat-pipe model is that on long timescales, Io is resurfacing uniformly. The presence of volcanic deposits across the surface and the lack of craters support this, but there are still significant questions surrounding the details of how it occurs. In section 1.4.2 I noted that there are three categories of eruption on Io: flow-dominated, explosive, and intra-patera. Flow-dominated eruptions and explosive eruptions resurface relatively large regions, with extensive lava flows in the former and pyroclastic deposits in the latter. Intra-patera eruptions, however, only seem to resurface the floors of the patera in which they occur. This produces something of a problem as intra-patera eruptions appear to be a source of much of Io's current surface heat flow, with the largest, Loki Patera, representing about 15% of the global heat flow (Spencer et al., 2000). Is a significant amount of energy being lost at the surface without resurfacing? If so, what implications does this have for the heat-pipe model, which requires rapid global resurfacing? If the heat-pipe model is correct, on long-timescales volcanoes must either be able to resurface regions far from volcanic edifices, or the positions of volcanoes must change. We simply haven't been observing Io for long enough to know how volcanic resurfacing operates on long-timescales, but there is clearly a complex story here.

1.8.4 Io's sulphur cycle

Whilst it has been clear since the mid-90s that sulphur is not the primary constituent of Io's lavas, it clearly plays an interesting role given the rich sulphur chemistry on the surface. The association of sulphur species with plume and pyroclastic deposits imply that sulphur is playing the role of a volatile in Io's eruptions, and indeed given the lack of water and CO_2 on the surface, it may be the dominant volatile species. We don't know, however, how deep this association goes. Are sulphur compounds simply providing a light dusting on the surface and interacting with lavas only during the eruption process, or are they being cycled through significant portions of the lithosphere? Does sulphur affect melting behaviour by modifying the solidus in an analogous way to water in terrestrial systems? Species like SO_2 are expected to melt or boil in contact with even well cooled silicate lavas, but other species such as the sulphur allotropes may be able to be buried some distance down into the lithosphere, feasibly enabling sulphur to play a role in silicate melting.

The question of sulphur's role in the Io system is almost certainly tied to the oxidation state of the mantle. If Io is not highly oxidised then the stable form of sulphur is likely to be FeS, which has a melting point comparable to basalt. Does buried sulphur form FeS, or is it remobilised before a reaction can take place? If large amounts of dense FeS are formed, what are the implications for dynamics? Do we expect a separate sulphide liquid to form, and if so how does this interact with the volcanic systems? If Io is highly oxidised then sulphur would be expected to form sulphate compounds, be we don't see clear evidence for such compounds at the surface. Zolotov and Fegley (1999) proposed that the oxidation state of Io's mantle lies close to this transition in primary sulphur stability and so it is possible that all of these different species play some role in the sulphur cycle. There has not, to date, been a model that aims to describe the physical and chemical processes of this system.

1.8.5 Magma flow within Io

An area that has seen relatively little work in recent years is the dynamics of magma flow within Io. Since O'Reilly and Davies (1981) presented the heat-pipe model it has remained relatively unchanged. Similarly, since Moore (2001) presented magmatic segregation as a model for heat transport within Io's mantle it has remained largely the same. This is a product of the success of both models in explaining basic observations, as well as the lack of new geophysical data since *Galileo*. Importantly though we have very little understanding of how magmatic segregation in the mantle and lithospheric heat-piping interact. The dynamics at this boundary will have broad consequences for both the mantle and lithosphere, as well as linking to a number of the other open questions I have discussed such as the potential formation of a magma ocean. If a high-melt-fraction layer is present near this boundary, does that imply strong asthenospheric dissipation, or does it imply that magma has difficulty penetrating the base of the lithosphere? Related to this is the question of how buried erupta are recycled back into the mantle. This recycling is a fundamental part of the heat-piping story but no work has aimed to quantify how it works in relation to mantle and lithosphere dynamics.

We also have relatively little understanding of how Io's volcanic systems operate beyond the basic heat-pipe model. The heat-pipe model simply assumes that conduits allow magma to migrate rapidly to the surface, but the variability in eruption styles on Io implies a more complicated story. Intra-patera volcanism appears to be quasi-periodic, potentially implying a tidal control on volcanism (de Kleer and de Pater, 2016), whilst explosive eruptions highlight the potential importance of sulphur as a volatile species. Outburst eruptions complicate this story further; are the highest temperature magmas on Io indicative of a distinct ultramafic source region, or do they demonstrate a lack of lithospheric processing that may have altered the compositions and temperatures of other erupta? A particular leading-order question that has not been addressed is the relative importance of intrusive and extrusive volcanism on Io. Given the sheer volume of material being erupted onto the surface, if anything approaching a comparable amount is freezing intrusively in the lithosphere it would be expected to have significant implications for mass and energy balances, as well as for the interpretation of eruption temperature and composition estimates at the surface.

These questions on the flow of magma within Io's interior, and in particular how mantle magma flow interacts with the lithospheric volcanic systems, are the primary focus of this thesis.

1.9 This thesis

At the start of this introduction I proposed that in order to fully understand how planetary volcanism controls the evolution of planetary bodies requires a parallel investigation of volcanic systems and the melting and melt transfer processes that feed them. A great deal has been achieved by investigating these separately (e.g., O'Reilly and Davies, 1981; Moore, 2001; McKinnon et al., 2001; Bierson and Nimmo, 2016) but to answer the questions posed in the previous section requires a coupled approach. By building models that consider the mantle and lithosphere together, in this thesis I will investigate how processes in each domain affect the other, and how they combine to control Io's thermal, structural, and compositional evolution.

The primary difficulty in coupling mantle magmatism and lithospheric volcanism is the inherently different timescales upon which they operate. Magmatic segregation in the mantle has velocities on the order of millimetres to centimetres per year, and evolves on thousands to millions of year timescales, whereas volcanic systems involve much faster flows that vary on the timescales of days or even hours. In order to resolve flows in volcanic systems as well as in the mantle would quickly become intractable. The approach I will take in this thesis is to parametrise the complex processes of volcanic systems with simple conservation equations.

In Chapter 2 I will provide some of the fundamental background that this thesis is built upon. I will spend some time going into the details of how tidal heating operates and the different approaches typically used in its calculation. I will then introduce some of the fundamental principles of two-phase fluid dynamics, upon which much of the mathematics in this thesis is built; I will do this in two parts, with a discussion of dynamics being followed by a discussion of energy conservation, utilising the enthalpy method (Katz, 2008). This chapter will finish with an overview of how I will couple volcanic systems to mantle magmatism in this thesis.

Armed with this background, in Chapter 3 I develop my parametrisation of Io's volcanic systems in a spherically-symmetric model, showing how mantle magmatism and volcanic systems can be modelled together, and what implications this has for interior structure. In this chapter I show that the eruption and burial process in Io's lithosphere is extremely efficient and, unchecked, predicts the formation of a lithosphere $>$ 600 km thick. I propose that the formation of magmatic intrusions in the lithosphere acts to limit its growth, yielding a thickness in agreement with observations. In Chapter 3 I also show that as solid lithosphere downwells into the mantle, high magma pressures cause the solid to rapidly decompact, feasibly resulting in the production of high melt fractions beneath the lithosphere.

In Chapter 4 I explore the implications of this coupled lithosphere–mantle system for Io's compositional evolution. Previous works considering the compositional evolution of Io have not coupled it to dynamics (e.g., Keszthelyi and McEwen, 1997; Keszthelyi et al., 2007). I am able to investigate this system with my coupled lithosphere-mantle model as it provides a way to model the burial of erupted lavas back into the mantle. With the introduction of a simple compositional system, I show that magmatic segregation and volcanism predict a compositionally stratified mantle. This stratification leads to the generation of refractory, high-temperature magmas in the deep mantle. I propose that if these magmas are able to migrate to the surface, they can explain Io's highest-temperature 'outburst' eruptions (de Pater et al., 2014).

Following this, in Chapter 5 I investigate the implications of spatially variable tidal heating on my coupled lithosphere–mantle model. By combining a three-dimensional tidal heating calculation with a system of one-dimensional column models, I show that variable tidal heating predicts specific lithospheric thickness variations and topography. This provides a new way to probe the tidal heating distribution from robust surface observations, where transient volcanic features have previously been relied upon (e.g., Rathbun et al., 2018).

I then turn to the broader implications, conclusions, limitations, and future work in Chapter 6. The results presented in this thesis have implications far beyond those that I have had time or space to investigate. The framework I have provided for a coupled investigation into magmatism and volcanism can be expanded in a number of directions, including two- and three-dimensional systems, more complex chemical models, secularly cooling bodies, and tidally heated exoplanets.

CHAPTER 2

Background

The work in this thesis builds upon a large amount of previous literature. Much of that surrounding Io was introduced in the previous section, but two areas of central importance to this thesis that I have not yet discussed in sufficient detail are tidal dissipation and two-phase fluid dynamics. Tidal dissipation, as introduced in the previous section, is the process that drives Io's volcanism by providing energy to the system. Two-phase fluid dynamics describes the magma flow processes that transport this energy from the interior to the surface. Given their central importance, I will take some time here to discuss each in the detail relevant for this thesis.

Tidal dissipation is a complex subject that is closely intertwined with orbital dynamics and material science. This thesis does not aim to make advances in the calculation of tidal heating, instead focussing on investigating its effects. Nonetheless, many of the assumptions that this thesis is built upon, as well as many of the questions that I will address, require at least a cursory understanding of how tidal heating operates and its relationship to interior structure and rheology. The first part of this chapter aims to provide the relevant background in this area. Following my discussion of tidal heating I will introduce two-phase fluid dynamics, discussing the modelling approaches that I will utilise throughout this thesis, as well as deriving a number of key equations. I will finish with an overview of how I will couple volcanic systems to mantle magma flow in this thesis.

2.1 Introduction to tidal dissipation

Io's volcanism is driven by tidal dissipation. Tidal dissipation (or tidal heating) is a process of fundamental importance in the Solar System (de Kleer et al., 2019b) from driving Io's volcanism to producing sub-surface oceans on Europa and Enceladus that may harbour life. Gravity raises tides on a satellite because of the gradient in gravitational potential across the body. A gravitational 'bulge' forms at the regions oriented toward and away from the parent because they feel the strongest and weakest gravitational attraction respectively. Io, like almost all major moons in the Solar System, is tidally locked. Tidally locked bodies rotate on their axis once per orbit, and so the same face always points toward the parent. For a tidally locked body in a circular orbit, the tidal bulges are static; there is no time dependent tidal stress, and no tidal heating.

Io and a large number of other satellites, however, are not in circular orbits. For a body in an elliptical orbit, the distance from the satellite to its parent changes as it orbits. At periapsis, when the satellite is closest to its parent, the differential gravity across the satellite is greatest, producing large tidal bulges. At apopasis, when the satellite is furthest from its parent, the differential gravity is weakest, producing small tidal bulges. As a satellite moves through an eccentric (elliptical) orbit, the tidal bulges grow and shrink, producing time dependent deformation (figure 2.1). These are eccentricity tides.

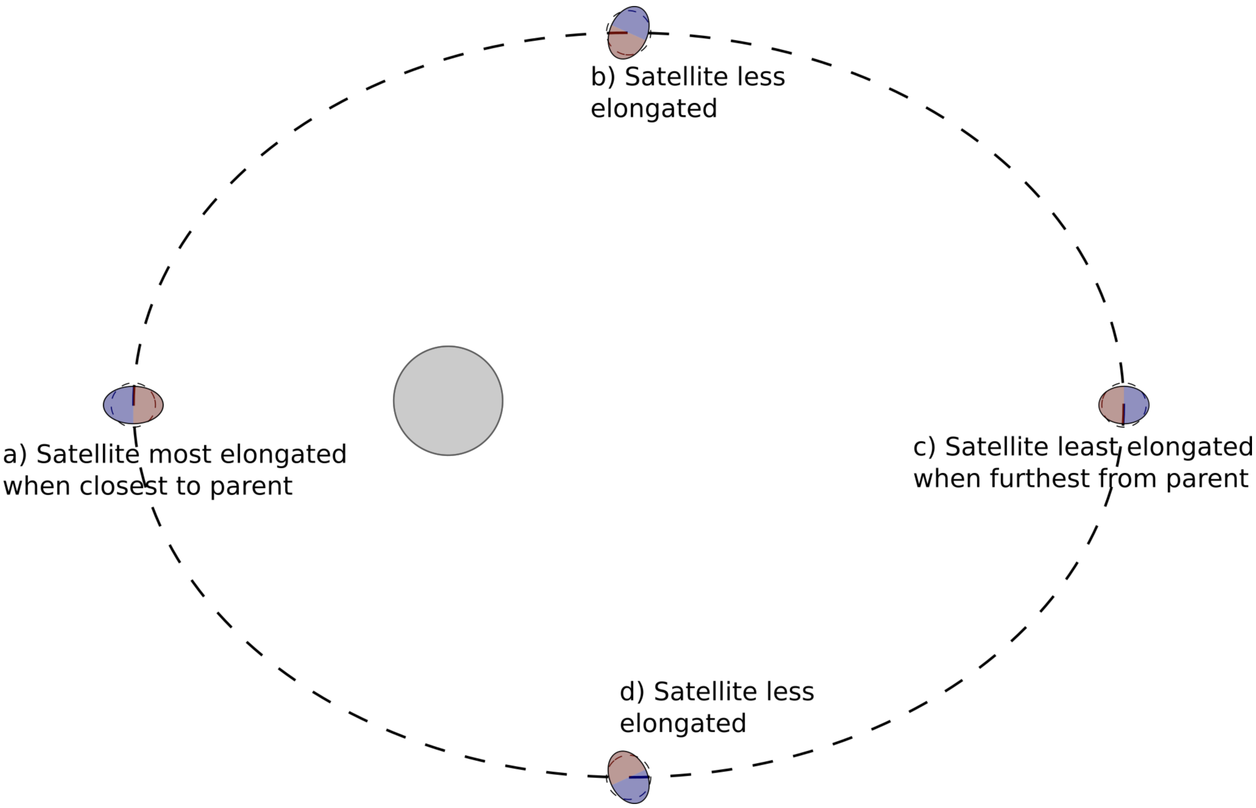

Figure 2.1: Schematic illustrating how an eccentric orbit causes time-dependent tidal deformation.

2.1.1 Tidal dissipation and rheology

The response of a body to deformation depends on its material properties (or ‘rheology’). When an elastic body is deformed, the resultant strain is proportional to the applied stress, and occurs effectively instantaneously. When the stress is removed, the strain is also removed; the deformation is recoverable. For a viscous body, however, strain rate is proportional to stress, and so when the stress is removed, strain rate drops to zero and the deformation is not recovered. How this causes heating can be best understood by considering the energy in the system.

When a body is subjected to stress, energy is put into the system. The work done by a force $\boldsymbol{F}$ in creating a displacement $\boldsymbol{x}$ is given by the dot product $\boldsymbol{F} \cdot \boldsymbol{x}$. In many systems, however, energy is recovered when the deformation is removed, so calculating dissipated energy is not straightforward. Whether (and how much) energy is recovered depends on the body's response. An elastic body recovers its shape, and so the energy is also recovered. A viscous body does not recover its shape, and so the energy is lost. The energy that is not recovered is dissipated within the system, primarily causing heating. Tidal dissipation, therefore, is the loss of energy in a planetary body that arises from a non-elastic response to tidal stress. This is also why tidally locked bodies in a circular orbit are not tidally heated; there is no time dependent tidal stress, and so there is no on-going viscous response.

Most real materials, and indeed the rocks and ices that Solar System moons are a made from, are viscoelastic. A viscoelastic body has an instantaneous elastic response to deformation, as well as a time dependent viscous response. Herein lies the principal difficulty in calculating tidal heating; the energy dissipated in a system depends strongly on the material properties of the system, which are poorly known in planetary bodies. The situation is further complicated by the fact that viscoelastic materials respond differently on different deformation timescales, which makes comparisons difficult between the systems of interest and laboratory experiments that aim to constrain them. In actuality many different rheological models could be assumed, and the choice is usually dependant on the timescales and physical processes being considered. The simplest rheological models treat the deep mantle as a viscous fluid, whereas in tidal calculations a viscoelastic model is commonly used. It is important to point out, however, that neither are an accurate description of the near-surface.

The calculation of tidal heating in a planetary body can typically be approached from two directions. The first and simplest is a calculation that considers a global average of the material properties of the interior. The global tidal dissipation Ψ (units W) caused by eccentricity tides is given by (Segatz et al., 1988; Lainey et al., 2009)

$$\Psi = -\frac{21}{2}\frac{k_2}{Q}\frac{n_m^5 R^5}{G}e^2, \tag{2.1}$$

where R is the radius of the satellite, G is the gravitational constant, e is the orbital eccentricity, k_2 is a tidal Love number, Q is the tidal quality factory, and n_m is the 'mean motion' of the Satellite (the average speed of its orbit). The tidal Love number k_2 quantifies the deformation of the gravity field of a body in response to tides raised by an external forcer, which is clearly a complicated function of the interior structure and material properties of the body. Indeed Murray and Dermott note that the Love numbers (there are two, k_2 and h_2, corresponding to gravity and shape respectively) "are mostly used as a convenient way of cloaking our ignorance of a body's internal structure"(Murray and Dermott, 2000, p.164). The tidal quality factor Q can be thought of as analogous to the quality factor of a simple harmonic oscillator, a low quality factor means that a lot of energy is lost as the body deforms, and a high quality factor means that little energy is lost. Clearly k_2 and Q mask a large amount of complexity, and indeed are usually bundled together in the combined quantity k_2/Q. The calculation of a body's k_2/Q from observations is an involved process, and is reviewed in Lainey (2016). The details of this calculation are not important here, the point is to remember that all methods for calculating tidal heating involve assumptions about the material properties of the body in question.

The other direction from which we can calculate tidal dissipation is to calculate the stress and strain rate tensors throughout a body. The tidal dissipation per unit volume ψ (units W/m^3) in a body averaged over one orbital period P is given by (Beuthe, 2013)

$$\psi = \frac{1}{P}\int_0^P \sigma_{ij}(t)\dot{\varepsilon}_{ij}(t)\mathrm{d}t, \tag{2.2}$$

where σ_{ij} and $\dot{\varepsilon}_{ij}$ are the components of the stress and strain rate tensors, which are time and location dependent, and summation of components is implied. Equation (2.2) comes from the fact that the rate at which stresses do work per unit volume is given by the product $\sigma_{ij}\dot{\varepsilon}_{ij}$ (see Appendix 5.B for a derivation), and implies that if the stress and strain rate are known throughout a body, not only the total tidal heating can be calculated (which is all equation (2.1) yields), but also its distribution. The calculation of the stress and strain rate tensors throughout a tidally deformed body is an involved process that I outline in Appendix 5.B, but for now it is important to note that, as discussed above, the relationships between stress and strain in a deformed body depend on the material properties of the body, as well as its structure.

Equation (2.2) provides some useful intuition into what makes a material dissipative. For a stiff (or rigid) body the strain is limited by elastic stress, which results in low dissipation. Further, if the body is nominally elastic then stress and strain are almost exactly in phase, resulting in no dissipation. For a low viscosity body, however, strain is limited by self-gravitation — a restoring force that acts to maintain hydrostatic equilibrium. This also results in low dissipation, even though the stress and strain may be completely out of phase. A dissipative material will lie in between these end-members; it will be rigid enough that self-gravitation does not significantly limit strain, but weak enough that elastic stresses don't either. An important piece of this puzzle then is to think about what makes a material 'strong' or 'weak'. Temperature can exert a strong control on dissipation because as temperature increases materials weaken — especially if they begin to melt. Thus as a body is heated by tides, its response to those same tides changes. Through these considerations the links between tidal dissipation, heat transport mechanisms, and interior dynamics start to become clear.

Some aspects of how tidal heating operates are well understood, but many are not. One of the key areas in which tidal heating is poorly understood is its relationship to rheology. In order to calculate the stress and strain rate tensors throughout a body, a specific viscoelastic rheological law must be used. The most commonly used viscoelastic law is Maxwell viscoelasticity, but it has been noted since this methodology first emerged that in order to match Io's observed dissipation, a very low shear viscosity of order $10^{13} - 10^{16}$ Pa s is required — much lower than is considered reasonable for a competent silicate body (Bierson and Nimmo, 2016). Steps have been made to address this by investigating empirical rheologies that have some laboratory justification (Bierson and Nimmo, 2016; Renaud and Henning, 2018) but the issue remains largely unresolved; we do not know enough about how rocks respond to deformation on the length-scales or time-scales involved in tidal processes.

Despite this considerable limitation, the general patterns of heating that can be produced by tides on a spherically symmetric body are relatively well known (Beuthe, 2013). These patterns depend on the rheological structure of the body, and for Io two end-members have emerged, which are shown schematically in figure 2.2. If heating is distributed throughout the mantle then the radially integrated heating rate will be highest at the poles, whereas if heating is concentrated in a dissipative asthenosphere then radially integrated heating will be highest at the equator (Segatz et al., 1988; Beuthe, 2013). As discussed in section 1.5, a number of works have aimed to look for these patterns in observations of volcanic activity with little community consensus.

The possible tidal heating patterns predicted for Io themselves depend on some very important assumptions. The calculation of these patterns assumes a symmetry of spherical harmonic coefficients — an assumption that breaks down if the body is not spherically symmetric. Indeed the heating distribution produced within a spherically symmetric body is itself not spherically symmetric, and so when applied back to the body will not result in a spherically symmetric structure. This problem lies at the heart of efforts to couple tidal heating calculations to interior dynamics (including my own in Chapter 5), and we as yet do not know the extent to which the patterns of dissipation would change in a fully three-dimensional calculation. Ultimately the assumption is made that the tidal heating patterns would not change much, at least not in the general prediction of whether heating rate is higher at the poles or equator, and I will continue with this assumption in this thesis.

We see then that there are a number of open questions in the tidal dissipation literature, with potentially significant implications for an investigation into Io's dynamics. Perhaps the foremost of these is the question of what rheological law is appropriate for tidal calculations.

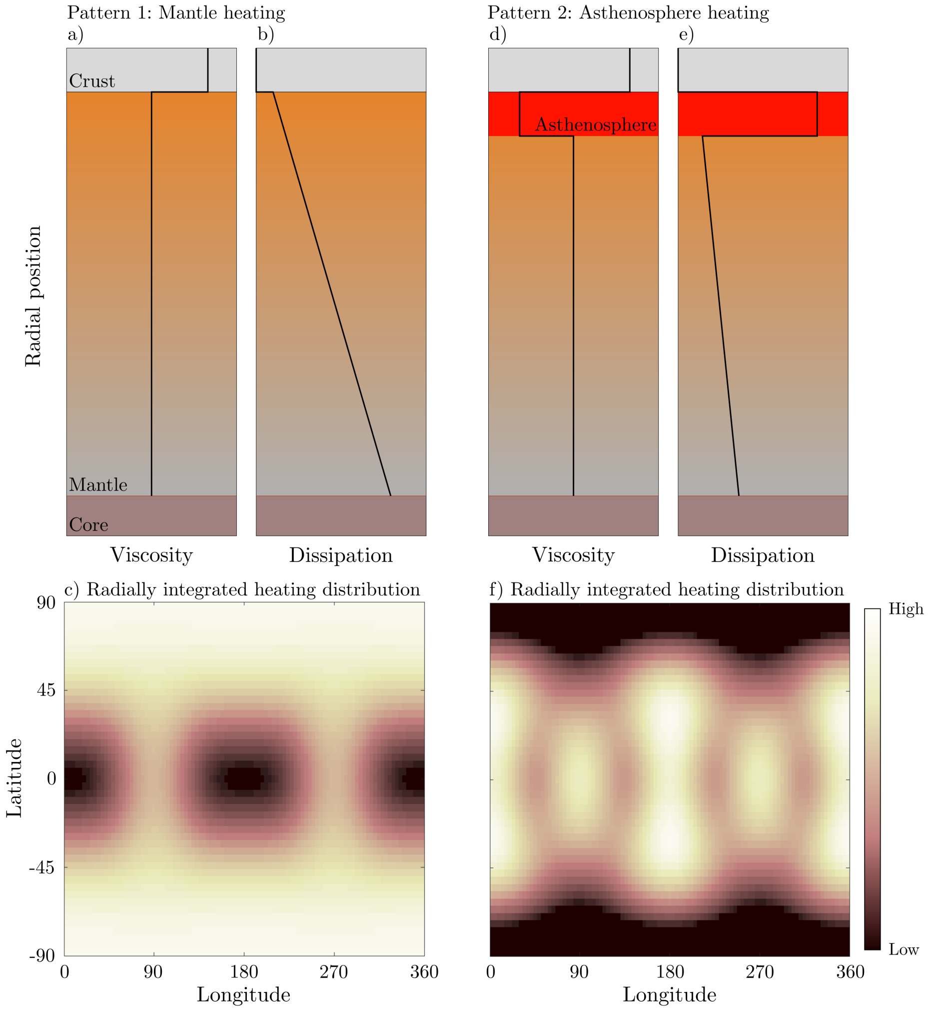

Figure 2.2: Schematic illustrating two plausible radial viscosity and dissipation structures, and the corresponding radially integrated dissipation patterns. The top row shows viscosity and dissipation averaged over spherical shells, and the bottom row shows the radially integrated dissipation rate at the surface. Panels a, b, and c show the case where viscosity is uniform in the mantle, and panels d, e, and f show the case where a low viscosity asthenosphere is present. In general dissipation increases with depth, but the presence of a low viscosity asthenosphere concentrates dissipation in that layer. I assume that the total dissipation is known and constant. Pattern 1 is ‘mantle heating’, where radially integrated dissipation is highest at the poles. Pattern 2 is ‘asthenosphere heating’, where radially integrated dissipation is highest at the equator.

If, for example, the appropriate rheological law results in high dissipation rates in regions of high melt fraction, this will have significant implications for dynamics. Further, a means of calculating dissipation for a non-spherically symmetric body is required to rigorously couple tidal heating and dynamics. Such a method would ideally not come at the cost of orders of magnitude increases in computation time if it is to be coupled to a dynamic model. These complexities, together with the leading-order degree-1 nature of tidal heating motivate my approach for the next two chapters of this thesis in simply taking a constant tidal heating rate. I will show that many of my solutions in the near surface such as eruption rates and lithospheric thicknesses depend only on the radially integrated heating rate and so the effects of this simplification are relatively small. In Chapter 5 I will employ a coupled tidal heating–dynamics model that relies upon the assumptions and falls victim to the limitations discussed here.

2.2 The dynamics of two-phase flow

Buoyant magmatic segregation — a process central to this thesis — is the differential flow of pore-space magma with respect to a solid matrix. In section 1.6.2 I noted that magmatic segregation is thought to be the dominant heat transfer process operating in Io's mantle (Moore, 2001; Breuer and Moore, 2015; Bierson and Nimmo, 2016). Qualitatively this is a process where buoyant magma rises through a solid matrix. A full, quantitative understanding, however, requires a review of the underlying fluid dynamics. In a magmatically segregating system, both the liquid and the solid matrix can flow; this is referred to as two-phase flow. The theoretical models developed in this thesis build upon large amounts of previous work on two-phase fluid dynamics. In this section I will overview the dynamics of two-phase flow and magmatic segregation that are pertinent to this thesis. I will discuss the energy transfers in two-phase flow in the subsequent section.

2.2.1 The representative volume element

At its most fundamental, two-phase flow is the migration of interstitial liquid through complicated pore structures. Modelling fluid migration on the grain-scale quickly becomes intractable when trying to scale up to larger physical systems. In order to derive models for two-phase flow that can be applied at scales much larger than the grain-scale, I adopt a continuum approach. Following a rich history of continuum theories, in order to do so I introduce the concept of a representative volume element (RVE). In this thesis, an RVE is considered as a macroscropic volume that contains a large number of grains, but that is small enough such that continuum scale changes across the volume are approximately linear. This allows us to average over microscopic complexities, and form finite-volume approximations at the continuum scale.

It is important to understand the relationship between the RVE and microscopic quantities like porosity. In a two-phase system we can define an indicator function $\Phi_l(\breve{\boldsymbol{x}})$ that identifies whether liquid is present at a microscopic point $\breve{\boldsymbol{x}}$ within the RVE (the $\breve{}$ symbol denotes a microscopic quantity).

$$\Phi_l \equiv \begin{cases} 1 & \text{if there is liquid at } \breve{\boldsymbol{x}} \\ 0 & \text{if there is solid at } \breve{\boldsymbol{x}}. \end{cases} \tag{2.3}$$

With this we can define the macroscopic porosity ϕ by integrating over the RVE, and normalising by its volume V_{RVE}

$$\phi = \frac{1}{V_{\text{RVE}}} \int_{\text{RVE}} \Phi_l(\breve{\boldsymbol{x}})\ \mathrm{d}^3\breve{\boldsymbol{x}}. \tag{2.4}$$

So we see that the RVE tells us an average of what is occurring at the microscopic level, and so cannot give us information below the scale of the RVE. I note that I don't take the subscript denoting liquid at the macroscopic scale because in a two-phase system, the solid fraction is simply $1 - \phi$.

2.2.2 Conservation of mass

Utilising the concept of the representative volume element, we can write an integral form for conservation of liquid mass

$$\frac{\mathrm{d}}{\mathrm{d}t}\int_{\mathrm{RVE}} \Phi_l \breve{\rho}_l \, \mathrm{d}^3\breve{\boldsymbol{x}} = \int_{\partial\mathrm{RVE}} -\Phi_l \breve{\rho}_l \breve{\boldsymbol{v}}_l \cdot \mathrm{d}\boldsymbol{S} + \int_{\mathcal{I}_{\mathrm{RVE}}} \breve{\rho}_l (\breve{\boldsymbol{v}}_{\mathcal{I}} - \breve{\boldsymbol{v}}_l) \cdot \breve{\boldsymbol{n}}_l \, \mathrm{d}S_{\mathcal{I}}, \tag{2.5}$$

where $\breve{\rho}_l$ is the microscopic liquid density, $\breve{\boldsymbol{v}}_l$ is the microscopic liquid velocity, $\breve{\boldsymbol{v}}_{\mathcal{I}}$ is the velocity of the interface between solid and liquid phases, and $\breve{\boldsymbol{n}}_l$ is the unit vector normal to this phase boundary, pointing into the solid. The first term in equation (2.5) represents the rate of change of the liquid mass in the RVE, the second term represents the rate at which liquid is flowing into the RVE, and the third term represents the rate at which liquid is crossing the moving interface between the two phases. This last term represents melting, and because we assume no 'gaps' can be opened up between the two phases, it must be equal and opposite for the solid. As such, the volumetric melting rate is defined as

$$\Gamma \equiv \frac{1}{V_{\mathrm{RVE}}} \int_{\mathcal{I}_{\mathrm{RVE}}} \breve{\rho}_l (\breve{\boldsymbol{v}}_{\mathcal{I}} - \breve{\boldsymbol{v}}_l) \cdot \breve{\boldsymbol{n}}_l \, \mathrm{d}S_{\mathcal{I}} = -\frac{1}{V_{\mathrm{RVE}}} \int_{\mathcal{I}_{\mathrm{RVE}}} \breve{\rho}_s (\breve{\boldsymbol{v}}_{\mathcal{I}} - \breve{\boldsymbol{v}}_s) \cdot \breve{\boldsymbol{n}}_s \, \mathrm{d}S_{\mathcal{I}}, \tag{2.6}$$

where $\breve{\rho}_s$ is the microscopic solid density, $\breve{\boldsymbol{u}}_s$ is the microscopic solid velocity, and $\breve{\boldsymbol{n}}_s = -\breve{\boldsymbol{n}}_l$. By dividing equation (2.5) by V_{RVE}, utilising the Divergence Theorem, shrinking the size of the RVE to a point in the continuum, and doing the same for the solid phase, we arrive at conservation of mass equations for the liquid and solid phases

$$\frac{\partial \phi \rho_l}{\partial t} + \boldsymbol{\nabla}\cdot(\phi \rho_l \boldsymbol{v}) = \Gamma, \tag{2.7}$$

$$\frac{\partial (1-\phi)\rho_s}{\partial t} + \boldsymbol{\nabla}\cdot[(1-\phi)\rho_s \boldsymbol{u}] = -\Gamma, \tag{2.8}$$

where $\boldsymbol{v}$ and $\boldsymbol{u}$ are the macroscopic liquid and solid velocities respectively. These equations tell us that changes in the solid and liquid fractions are caused by divergences of the solid and liquid fractions respectively, and phase changes (melting or freezing). It is important to note that I have not given a thermodynamic means of calculating the melting rate Γ. If the porosity evolution and phase velocities are known then the melting rate can be inferred, but to use equation (2.7) to calculate porosity evolution requires a closure on the melting rate.

Continuing the discussion of conservation of mass, by making the extended Boussinesq approximation (assuming the phases are mutually incompressible and that densities of the phases are equal and constant except in body force terms, see section 2.2.3), and adding equations (2.7) – (2.8) we get

$$\boldsymbol{\nabla}\cdot \overline{\boldsymbol{v}} = 0, \tag{2.9}$$

where an overline denotes a phase-averaged quantity $\overline{a} = \phi a_l + (1-\phi)a_s$. This is a continuity equation for the two-phase system that tells us that the two-phase system cannot dilate or contract. This can have the trivial solution that the solid and liquid are not moving, but if the segregation flux $\boldsymbol{q} = \phi(\boldsymbol{v} - \boldsymbol{u})$ is non-zero, equation (2.9) can be satisfied with non-zero solid and liquid velocities.

With a non-trivial solution to equation (2.9), it is often illustrative to consider the deformation of one of the individual phases. This is generally done by the introduction of the compaction rate, which is defined as

$$\mathcal{C} \equiv \boldsymbol{\nabla}\cdot \boldsymbol{u}, \tag{2.10}$$

and quantifies the volumetric deformation of the solid phase. The compaction rate is often defined this way but it is important to recognise that a positive compaction rate describes a dilating matrix, and so would perhaps be more accurately described as a ‘decompaction rate’. For consistency with previous literature, however, I take this definition.

2.2.3 The Darcy segregation flux

In section 2.2.2 I showed that mutually incompressible solids and liquids can flow past one-another provided $\boldsymbol{q} = \phi(\boldsymbol{v} - \boldsymbol{u}) \neq 0$, but this doesn't tell us anything about why solids and liquids would flow.

Flow of a liquid is driven by pressure gradients. McKenzie (1984) gives a form of Darcy's Law appropriate for a two-phase medium

$$\boldsymbol{q} = \phi(\boldsymbol{v} - \boldsymbol{u}) = -\frac{k_\phi}{\eta_l}\left(\boldsymbol{\nabla} P_l - \rho_l \boldsymbol{g}\right), \tag{2.11}$$

where P_l is the liquid pressure, η_l is the liquid viscosity, and $k_\phi = K_0\phi^n$ is the matrix permeability in which K_0 is a permeability constant and n is a constant generally taken to be between 2 and 3. Equation (2.11) tells us that the segregation flux $\boldsymbol{q}$ (which I will refer to at times as the Darcy segregation flux or the Darcy flux) is driven by liquid pressure gradients and gravity, and is modulated by the permeability and the liquid viscosity.

Equation (2.11) represents conservation of momentum for the liquid, but of course momentum must also be conserved in the solid phase. In this thesis I follow much of the two-phase fluid dynamics literature by treating the solid matrix as a viscous fluid. This is a poor approximation at low temperatures where brittle processes become important, and as such these processes cannot be investigated using the formulation employed in this thesis (see section 2.4). McKenzie (1984) gives conservation of momentum in the solid as

$$\boldsymbol{\nabla}\cdot 2\eta\dot{\boldsymbol{\varepsilon}}_s + \boldsymbol{\nabla}\,\zeta\mathcal{C} = \boldsymbol{\nabla}\,P_l - \overline{\rho}\boldsymbol{g} \tag{2.12}$$

where η is the shear viscosity of the two-phase aggregate, $\dot{\boldsymbol{\varepsilon}}_s$ is the deviatoric strain rate tensor, and ζ is the compaction viscosity (which is sometimes referred to as the bulk viscosity, McKenzie, 1984). Equation (2.12) tells us that the deviatoric and isotropic deformation of the matrix is driven by gradients in liquid pressure, and gravity acting on the bulk two-phase aggregate.

The liquid pressure can be eliminated from equation (2.11) by substituting equation (2.12) to give

$$\boldsymbol{q} = -\frac{k_\phi}{\eta_l}\left(\boldsymbol{\nabla}\,\zeta\mathcal{C} + \boldsymbol{\nabla}\cdot 2\eta\dot{\boldsymbol{\varepsilon}}_s + (1-\phi)\Delta\rho\boldsymbol{g}\right), \tag{2.13}$$

where $\Delta\rho$ is the density difference between the solid and liquid. This system can be simplified further using the definition of the deviatoric solid strain rate tensor

$$\dot{\boldsymbol{\varepsilon}} \equiv \frac{1}{2}\left[\boldsymbol{\nabla}\,\boldsymbol{u} + (\boldsymbol{\nabla}\,\boldsymbol{u})^{\mathrm{T}} - \frac{2}{3}\mathcal{C}\boldsymbol{I}\right], \tag{2.14}$$

which allows us to write

$$\boldsymbol{q} = -\frac{k_\phi}{\eta_l}\left(\boldsymbol{\nabla}\,\xi\mathcal{C} + (1-\phi)\Delta\rho\boldsymbol{g}\right), \tag{2.15}$$

where $\xi = \zeta + 4\eta/3$ is the augmented compaction viscosity, and where I have assumed that all off-diagonal terms in the solid deviatoric strain rate tensor are zero. Clearly this is an important assumption as it will preclude lateral flow, but given that the models employed in this thesis will be one-dimensional, I proceed with this simplification. Finally, as neither the compaction viscosity nor the shear viscosity are known for Io's mantle, I will simply assume that $\xi = \zeta$ and explore a range of values for both the compaction and shear viscosities.

Some intuition into equation (2.15) can be gained by defining the liquid overpressure (or compaction pressure) P. Compaction of the matrix is caused by a difference in pressure between the solid and liquid, which is quantified as (Keller et al., 2013)

$$P = (1-\phi)(P_l - P_s) = \zeta\mathcal{C}, \tag{2.16}$$

where P_s is the solid pressure. If liquid pressure exceeds solid pressure, the matrix will be forced to decompact. I formulate conservation of momentum in terms of this liquid overpressure

$$\boldsymbol{q} = -\frac{k_\phi}{\eta_l}\left(\boldsymbol{\nabla} P + (1-\phi)\Delta\rho\boldsymbol{g}\right), \tag{2.17}$$

thus arriving at the form of Darcy's Law — representing conservation of momentum — that I use throughout this thesis.

2.3 Magmatic energy transport

Magmatic segregation is of fundamental importance in transporting tidal heat out of Io's deep interior (section 1.6.2). As described in the previous section, two phase flow involves the buoyant rise of magma through pore-space, and the corresponding sinking of the dense solid matrix. This process transfers energy because even if the solid and liquid are at the same temperature, the melt also carries latent heat, and so more energy is transported by the melt than the solid. In this section I will discuss how energy transport is modelled in a two-phase system, focusing on the enthalpy method (Katz, 2008), which I employ throughout this thesis.

2.3.1 Conservation of energy: the enthalpy method

The enthalpy method allows melting and freezing rates (see equations (2.5) – (2.8)) to be calculated based on an equilibrium phase diagram (Katz, 2008). Within an RVE, there is a total amount of energy that is available to be partitioned between sensible and latent heat. This total amount of energy is given by the bulk enthalpy $H = \overline{\rho h}$. The enthalpy per unit mass for the solid and liquid respectively is

$$h_s = h_0 + C(T - T_0), \tag{2.18}$$

$$h_l = h_0 + C(T - T_0) + L, \tag{2.19}$$

where C is the specific heat capacity (assumed constant and equal between phases), L is the latent heat, T is the temperature, and h_0 is some reference enthalpy defined at a reference temperature T_0. Combining equations (2.18) – (2.19), we have an expression for the bulk enthalpy (Katz, 2008)

$$H = \phi\rho L + \rho h_0 + \rho C(T - T_0). \tag{2.20}$$

We can choose to take $h_0 = 0$ at absolute zero to simplify this equation, though it is important to note that the specific heat capacity is not constant over large temperature ranges, and so defining T_0 close to the temperatures in the system is preferable. In a single component system where the melting temperature T_m is known, if $H > \rho h_0 + \rho C(T_m - T_0)$ then the porosity is uniquely defined because temperature cannot exceed the melting point until all of the solid has melted. Similarly if $H < \rho h_0 + \rho C(T_m - T_0)$ then we know the temperature because porosity cannot be negative. The equilibrium ‘phase diagram’ is clearly trivial in a single component system, but in all applications of the enthalpy method, the temperature, porosity, and compositions of the phases are uniquely defined by the phase diagram, the local composition, and the bulk enthalpy (see Chapter 4). This has three significant benefits. Firstly, there is no need to solve a porosity evolution equation such as (2.7). Secondly, no ad-hoc (or highly-complicated) parametrisations of the melting rate are required. Thirdly, the same system of equations can be easily applied in solid and partially molten domains. With this approach I can model the lithosphere and mantle of Io together without explicitly prescribing the position of the boundary between them.

All that is then left is to provide a conservation of energy equation, by which the bulk enthalpy evolves. The conservation of energy equation is derived in a similar way to conservation of mass, by utilising the finite volume element to give

$$\frac{1}{\rho C}\frac{\partial H}{\partial t} + \boldsymbol{\nabla}\cdot[(\boldsymbol{u}+\boldsymbol{q})T] + \boldsymbol{\nabla}\cdot\left[(\phi\boldsymbol{u}+\boldsymbol{q})\,\frac{L}{C}\right] = \boldsymbol{\nabla}\cdot(\kappa\boldsymbol{\nabla}T) + \frac{\psi}{\rho C}, \tag{2.21}$$

where ψ is the volumetric tidal dissipation rate. A derivation of equation (2.21) can be found in Appendix A of Katz (2008), except that no internal heating is included there, and I neglect adiabatic pressure changes due to Io's small size. Equation (2.21) says that changes in the bulk enthalpy are driven by the advection of sensible and latent heat, diffusion of sensible heat, and internal heating.

2.4 Volcanic plumbing systems

I have indicated at various points in this introduction that a central theme to this thesis is the parallel consideration of mantle two-phase flow and volcanic plumbing systems in the lithosphere. The primary complexity in coupling these domains is the vastly different timescales on which magma flows in each. The details of how I approach this problem will be set out throughout this thesis (in particular in Chapter 3 where it is first introduced), but it is illustrative at this point to set out the general principles in the context of two-phase fluid dynamics.

To couple Io's volcanic systems to the underlying mantle, we must consider how they can be described on the timescales relevant to the evolution of the mantle. My approach is to treat the volcanic systems as a reservoir that interacts with the lithosphere and underlying mantle only by the exchange of mass (and the energy that it carries). By analogy with equations (2.7) – (2.8), conservation of mass per unit volume in the volcanic systems (which I will refer to as a 'plumbing system' interchangeably) can be written as

$$\frac{\partial \phi_p}{\partial t} + \boldsymbol{\nabla} \cdot \boldsymbol{q}_p = E - M, \tag{2.22}$$

where ϕ_p is the average proportion of the RVE that is taken up by the volcanic plumbing systems, $\boldsymbol{q}_p$ is the flux of material in the system, E is the rate of transfer of material into the plumbing system, and M is the rate of transfer of material out of the plumbing system. I will immediately make the fundamental assumption that the proportion of Io that is occupied by the volcanic system is very small $\phi_p \ll 1$. This means we can take

$$\phi_l + \phi_s + \phi_p \simeq \phi_l + \phi_s = 1, \tag{2.23}$$

where ϕ_l is the liquid fraction and ϕ_s is the solid fraction. Equation (2.23) allows us to revert to using ϕ to refer to the liquid fraction, and $(1-\phi)$ the solid fraction. Equation (2.23) allows the further assumption that the proportion ϕ_p can be considered constant. This allows equation (2.22) to be written as

$$\boldsymbol{\nabla}\cdot \boldsymbol{q}_p = E - M, \tag{2.24}$$

The terms E and M must also be present in the conservation of mass equation for the continuum as melt can only enter the volcanic system by leaving the pore-space, and can only leave the volcanic system by transferring into the continuum. Thus equation (2.9) becomes

$$\boldsymbol{\nabla}\cdot \overline{\boldsymbol{v}} = -E + M. \tag{2.25}$$

Terms in E and M are also present in the conservation of energy equation, the formulation of which involves substituting conservation of mass equations (see Appendix A of Katz, 2008). The full conservation of energy equation including these terms is

$$\frac{1}{\rho C}\frac{\partial H}{\partial t} + \boldsymbol{\nabla}\cdot[(\boldsymbol{u}+\boldsymbol{q})T] + \boldsymbol{\nabla}\cdot\left[(\phi\boldsymbol{u}+\boldsymbol{q})\frac{L}{C}\right] = \boldsymbol{\nabla}\cdot(\kappa\boldsymbol{\nabla}T) + \frac{\psi}{\rho C} - E\left(T+\frac{L}{C}\right) + M\left(T_m+\frac{L}{C}\right), \tag{2.26}$$

where T_m is the temperature of emplacing magma. We see that the extraction and emplacement of magma removes heat from or adds heat to the continuum respectively. The energy associated with the transfer is in the form of both sensible and latent heat, as we assume this transfer occurs in the liquid phase. A conservation of energy equation in the plumbing system is not required when there is only one chemical component; the temperature of magma is constant. In Chapter 4 I present the formulation for a two chemical component system.

The conservation of mass approach that I employ for Io's volcanic systems clearly masks a significant amount of detail. Firstly, my approach precludes a consideration of the mechanical processes by which dikes actually propagate. The wildly different timescales on which dikes propagate compared to viscous mantle flow makes an approach that encompasses both complex. By focussing on the long timescales of viscous flow I significantly reduce the complexity of the system, enabling the broad implications of magmatic extraction and emplacement to be investigated, but it also means that I must introduce abstract terms like E and M to describe a range of different physical processes. An understanding of how these physical processes actually operate on Io would illuminate a great deal about the thermal structure and stress state of the lithosphere, but cannot be obtained from my highly parametrised approach. Forms for E and M could be devised that replicate results from more detailed studies into the physics of dike initiation, propagation and emplacement such as Havlin et al. (2013), but a complete understanding will ultimately require a full coupling of the physics of dike propagation to mantle magma flow.

Another significant drawback to my conservation of mass approach is that it cannot be used to rigorously explore compositional evolution in volcanic systems. Chemical differentiation of magmas within Earth's crust is an extremely important process in determining the compositions of erupted products. Jackson et al. (2018) showed that the reactive flow of magmas injected into the lithosphere causes significant compositional evolution, and that this compositional evolution in turn gives rise to the high-melt-fraction magmas that ultimately erupt. My approach does not provide a context in which to explore the physical processes that govern the evolution of magmas in the lithosphere, instead implying a much closer relationship between mantle magmas and erupted products. The lack of evidence for any silica-rich lavas on Io provides some justification for neglecting magma evolution in the lithosphere, but this in of itself is an interesting problem. Why would lavas propagating through a thick lithosphere never evolve to silica-rich compositions? This kind of question cannot be tackled with the conservation of mass approach that I take in this thesis.

My approach for modelling Io's volcanic systems is chosen for the ease with which it can be coupled to the underlying mantle. It allows me to investigate the two domains together, and quantify the broad importance of magma extraction, emplacement, and eruption for both regions. The points of coupling between the volcanic systems and the lithosphere and underlying mantle are clearly the rates E and M. These parameters are discussed extensively throughout this thesis but I will introduce each here. As I have noted in this section, much more complicated forms for E and M than those presented here could be devised — ones that aim to parametrise complex physical processes in more detail. This would be an interesting avenue for future work, but will always fall short of a full consideration of the physics of dike initiation, propagation, emplacement, and eruption.

2.4.1 Extraction of magma to volcanic systems

Within the mantle, I am assuming that magma is ubiquitous and exists in the pore-space of the partially molten rock. Some mechanism must allow this pore-space magma to transfer into the volcanic systems that carry it to the surface. There is extensive literature on the formation and migration of dikes within the lithosphere (e.g., Havlin et al., 2013), but I assume that these processes operate on shorter timescales than I am aiming to investigate here. Rather, I make use of Io's apparent thermal steady state; it is losing heat from its surface at the rate it is being generated in the interior by tidal dissipation (Lainey, 2016). This implies that magma is not accumulating in the interior on long timescales. As such I seek a rate of transfer from the mantle pore space to the volcanic systems that is related to magma production in the interior, and that can respond dynamically if there are changes in the production rate.

I choose to base extraction on the liquid overpressure. If liquid overpressure is high it may facilitate processes like brittle failure, initiating dikes. Further, as I will show in this thesis, the liquid overpressure is highest beneath impermeable barriers such as the lithosphere, which is also where we would expect any such features to form. Throughout this thesis I take extraction to be

$$E = \nu(P - P_c), \tag{2.27}$$

where ν is some constant, and P_c is some critical liquid overpressure that must be exceeded in order for a transfer to occur. Equation (2.27) ensures that extraction of magma to volcanic systems occurs at places where magma accumulates (i.e., beneath the lithosphere) and allows its continued rise by transferring it to the volcanic systems.

The details of how this extraction physically occurs are beyond the scope of this thesis (though I speculate on this in Chapter 3); on the long timescales of interest here it is simply important that such a transfer occurs. In this vein I will take ν to be large such that overpressure in regions of extraction $P \simeq P_c$, and I will explore the effect of varying P_c (see Chapter 3).

2.4.2 The formation of magmatic intrusions

As discussed in section 1.8, it is possible that the formation of magmatic intrusions is a significant source of mass and energy to Io's lithosphere. To explore this possibility I allow for the emplacement of magma out of the volcanic system into the surroundings through the transfer rate M in equations (2.24) – (2.25).

There are a number of different choices that could be made in defining the emplacement rate. In this thesis I will consider three different formulations. The first of these is the most detailed, aiming to investigate both the rate and distribution of emplacement. This formulation assumes that intrusions form because of a temperature difference between magma and the surrounding host-rock

$$M = \begin{cases} \frac{hC(T_m - T)}{L} & T > T_e, \\ 0 & T < T_e, \end{cases} \tag{2.28}$$

where h is a constant to be explored, T_m is the temperature of magma in the volcanic system, and T_e is some temperature below which emplacement is assumed not to occur. This formulation introduces two largely unconstrained parameters in h and T_e; the first determines the absolute rate at which intrusions form, and the second controls where intrusions can form. Discussion of these values is given in Chapter 3.

The other two formulations that I consider are developed to have greater simplicity, and I will use them in particular when the detailed effects of emplacement are not the primary focus (Chapter 5). These more simple formulations are based around the assumption that the emplacement rate may be related to, or independent of, the magnitude of the flux through the volcanic systems $\boldsymbol{q}_p$. The second formulation I investigate takes a simple linear relationship between emplacement rate and the magnitude of $\boldsymbol{q}_p$

$$M = \lambda_q \left| \boldsymbol{q}_p \right| . \tag{2.29}$$

The third and final formulation that I consider assumes simply that emplacement occurs at a constant rate

$$M = \lambda_c. \tag{2.30}$$

The third formulation can be considered a simplification of the first, with emplacement being set by external factors unrelated to the amount of magma in the volcanic system. In Chapter 3, I will show that each formulation produces broadly the same effects. In Chapters 3 and 4 I focus on the temperature dependent formulation. In Chapter 5, I will use the flux-dependent and constant formulations as these can be used to derive analytical expressions.

CHAPTER 3

Coupling magmatism and volcanism in Io

The model, results, and analysis presented in this chapter have been published in Spencer et al. (2020a). This chapter constitutes a minor reformatting of that work to fit within the broader context of this thesis.

3.1 Introduction

Io's extensive volcanism has lead to significant interest in understanding its internal structure and the energy balances that control it. To begin an investigation into Io's planetary volcanism I can make use of some key observations. The rate of tidal dissipation — the process heating Io, see section 2.1 — appears to coincide closely with the rate of surface heat loss (Lainey et al., 2009), implying that Io is close to a state of thermal equilibrium. Further, the surface is crater free with globally distributed, low-relief volcanoes, implying relatively uniform global resurfacing. These observations imply that Io's leading-order structure is spherically symmetric and roughly steady state. An understanding of this leading-order structure must serve as the foundation for investigations into spatial heterogeneity and temporal evolution.

As discussed in section 1.6, Io's radial structure is determined by the heat and mass transport mechanisms operating in its interior. Energy emission from the surface is concentrated at volcanic features, suggesting that volcanism, not conduction, is the primary heat transport mechanism in the lithosphere. The 'heat-pipe' process introduced by O'Reilly and Davies (1981), and summarised in section 1.6.1, exports heat across the lithosphere by advection though volcanic systems. This allows the growth of a thick lithosphere, which limits the efficiency of conductive heat loss, and supports Io's high mountains.

Heat transport in Io's mantle is more widely debated (see section 1.6.2). A thermal equilibrium requires that the rate of energy export matches the rate of tidal dissipation. Moore (2003) demonstrated that an equilibrium between convective heat transport and tidal dissipation would occur at melt fractions above disaggregation (figure 1.5). However, the expected tidal heat production under these conditions is significantly less than the observed surface heat flux. This suggests that convection cannot be the primary mechanism for delivering heat to the lithosphere. Alternatively, magmatic segregation is capable of transporting the observed tidal heat input at low melt fractions (Moore, 2001; Breuer and Moore, 2015). It is has thus become the paradigm view that Io's tidal heat is removed from the mantle by magmatic segregation and is transported across the lithosphere by a volcanic plumbing system. Previous works, however, have not aimed to couple the heat transfer processes in these two domains. In this chapter I explore how these processes combine and affect each-other, and specifically address what controls the total amount of magma produced, the amounts emplaced intrusively as plutons and extrusively as surface volcanism, and the controls these place on lithospheric thickness.

The thickness of Io's lithosphere is determined by the depth to which buried erupta downwell before they are heated to their melting point. Previous work has not considered the dynamics of magma at the boundary between the lithosphere and the underlying mantle or in the lower lithosphere, but the emplacement of plutons introduces heat to the lithosphere, which reduces the lithospheric thickness and modifies its thermal profile. In this chapter I present a coupled model of lithosphere and mantle dynamics that assesses these processes. The model is formulated to make predictions of elastic thickness, surface heat fluxes, and globally averaged eruption rates, predictions that can be readily tested by future missions to the Jupiter system. My results indicate that the heat balance and melt-transport mechanisms in the lithosphere and at the boundary between the lithosphere and underlying mantle ultimately determine the thickness of Io's lithosphere and the melt distribution below it.

Magnetic induction measurements — interpreted in terms of mantle electrical conductivity — have been used to infer the presence of a layer around 50 km thick with more than 20% melt fraction (a "magma ocean") beneath Io's lithosphere (Khurana et al., 2011). I note, however, that the interpretation of the induction measurements as a high-melt-fraction region is debated; Blöcker et al. (2018) argue that interaction with Io's plasma environment is a better explanation of induction measurements than is a magma ocean. Nonetheless, previous studies have proposed that this inferred high-melt-fraction layer could be a region of enhanced tidal dissipation (Hamilton et al., 2013; Bierson and Nimmo, 2016). Tidal dissipation theory predicts that for a homogeneous body, dissipation is highest at the center. A low viscosity layer underlying a rigid lithosphere may allow the concentration of dissipation, but models that invoke it must explain how such a structure arises. In this chapter I use my coupled dynamical model of the lithosphere and underlying mantle to investigate the feasibility of a high-melt-fraction layer occurring without the need for enhanced dissipation.

This chapter is organised as follows. First I outline the physics of the model before presenting results showing the key controls on *i*) lithospheric thickness, *ii*) emplacement rates, and *iii*) a high-melt-fraction layer beneath the lithosphere. I then discuss the implications of these results for interior structure and evolution.

3.2 Model description

The model, shown schematically in figure 3.1, considers the dynamical effects of tidal dissipation on Io's lithosphere and underlying mantle. These are modelled as a continuum that is either solid (the lithosphere) or partially molten (the underlying mantle). I model melting, magmatic segregation, and compaction (the contraction of a solid matrix as melt is expelled) with a system of conservation equations for mass, momentum, and energy appropriate for a compacting two-phase medium (McKenzie, 1984, and also see sections 2.2 – 2.3). Magmatic flow can also occur in a volcanic plumbing system that stretches from the upper mantle to the surface, and that exchanges mass with the partially-molten mantle and lithosphere. In the upper mantle, melt can leave the pore space and enter the plumbing system and then, as melt rises in the plumbing system, it can form intrusions (freeze) in the lithosphere, delivering mass and energy to the surroundings. The volcanic flux that reaches the surface (the eruptive flux) instantly cools and imparts a downward flux of cold surface material. The boundary between the lithosphere and partially-molten mantle is defined as the depth at which the temperature is equal to the solidus temperature (see table 3.1); its location is determined as part of the model. Lithospheric thickness is thus defined as the distance over which the cold, downwelling surface material heats before it begins to re-melt. At points I will refer to the mantle underlying the lithosphere as simply 'the mantle'. On Earth the lithosphere includes part of the mantle, which is defined by a petrological transition from the crust. It is not clear that such a petrological transition exists on Io, and in the absence of a better name for region between the core and lithosphere, I simply use mantle.

The model invokes some simplifying assumptions. Io's volcanoes are distributed across its entire surface (Kirchoff et al., 2011; Williams et al., 2011); this and the lack of craters implies global resurfacing. Though it has been proposed that there is a degree-2 pattern to hotspot locations (Kirchoff et al., 2011; Hamilton et al., 2013; Rathbun et al., 2018), I investigate a spherically symmetric model for consistency with Io's apparent global resurfacing. I assume that deviations from spherical symmetry are secondary effects imprinted on a leading-order radial structure. These deviations from spherical symmetry are expected to be important in discerning the global distribution of tidal dissipation (Veeder et al., 2012; de Kleer and de Pater, 2016; Cantrall et al., 2018; Rathbun et al., 2018). Tidal dissipation models that match Io's surface heat flux utilise either very low viscosities (Steinke et al., 2020) or empirically parameterised rheologies (Bierson and Nimmo, 2016; Renaud and Henning, 2018). To explore the leading-order dynamics without a dependence on poorly constrained parameters, in this chapter I take tidal dissipation to be uniformly distributed. I assess the melt configurations this produces and discuss whether this may lead to significant radial partitioning of tidal heating; a coupled system of dynamics and tidal heating will be explored in Chapter 5. In order to keep this initial model simple, I assume one-component thermodynamics, so the composition of the rock is neglected. I will relax this assumption in Chapter 4, where I incorporate a two-component system. I neglect the pressure-dependence of the melting temperature due to the small size of Io and hence the low pressures in the mantle. Finally I assume that melt is mobile in the partially molten mantle due to the large grain size, and hence large permeability, expected for a refractory, annealed mantle (Lichtenberg et al., 2019).

In the mantle (radii $r_m < r < r_l$), temperature is at the melting point and heat transport occurs solely by magmatic transport of latent heat. Buoyancy causes the upward flow of magma, which is balanced by the downward flow of solid. In the lithosphere ($r_l < r < R$, defined as having a spherically-averaged temperature below the melting point), the temperature drop to the surface drives a conductive heat flux, while the downwelling solid lithosphere transports the cold surface temperature inward (Schenk and Bulmer, 1998). The volcanic plumbing system continues to transport magma and latent heat upward through the lithosphere. I make minimal assumptions about what this plumbing system actually looks like, but require that it interacts with the solid lithosphere by emplacement of material (the for-

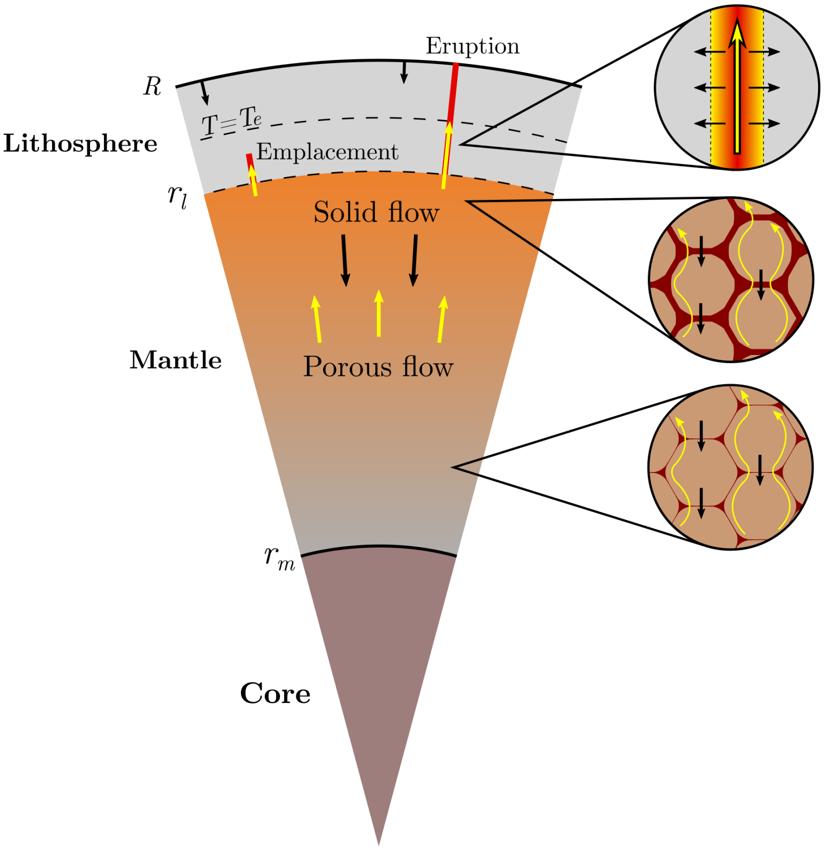

Figure 3.1: Schematic of the model for Io. Magma rises buoyantly through the mantle while the solid moves downward. At the top of the mantle, magma enters the volcanic plumbing system. Some of this magma is emplaced (intruded) into lithosphere; the rest rises to the surface and fuels volcanic eruptions. The core is excluded from the model.

mation of plutonic intrusions). This emplaced material is a lithospheric source of both mass and heat. The actual volume of the plumbing system is assumed to be negligible (consistent with the flow there being much faster than that of the solid and melt elsewhere).

3.2.1 Model equations

In the partially molten mantle, which has melt fraction $\phi(r,t)$, I represent the solid velocity by $\boldsymbol{u}$ and the relative liquid velocity (the Darcy segregation flux) by $\boldsymbol{q} = \phi(\boldsymbol{v} - \boldsymbol{u})$. Darcy's law relates the segregation flux to pressure gradients and buoyancy

$$\boldsymbol{q} = -\frac{K_0\phi^n}{\eta_l}\Big[(1-\phi)\Delta\rho\boldsymbol{g} + \boldsymbol{\nabla}P\Big], \tag{3.1}$$

where $K_0\phi^n$ is the permeability, n is the permeability exponent, $\Delta\rho$ is the density difference between solid and liquid, $\boldsymbol{g} = -g\hat{\boldsymbol{r}}$ is the gravity vector, η_l is the liquid viscosity, and $P = (1-\phi)(P_l - P_s)$ is the compaction pressure (Keller et al., 2013). See section 2.2.3 for a derivation.

Transfer of material between the lithosphere–mantle system and the volcanic plumbing system is considered in the conservation of mass equation. Making a standard Boussinesq approximation (that is, ignoring the density difference except were it appears in the body force term of equation (3.1)), conservation of solid and liquid mass require

$$\frac{\partial}{\partial t}(1-\phi) + \boldsymbol{\nabla}\cdot[(1-\phi)\boldsymbol{u}] = -\Gamma + M, \tag{3.2}$$

$$\frac{\partial\phi}{\partial t} + \boldsymbol{\nabla}\cdot(\phi\boldsymbol{u} + \boldsymbol{q}) = \Gamma - E, \tag{3.3}$$

where Γ is the volume transfer rate of solid into liquid (the melting rate), E is the extraction rate to the plumbing system (a sink of mass from the partially-molten mantle), and M is the emplacement rate from the plumbing system (a source of mass to the lithosphere). Adding equations (3.2) and (3.3) gives conservation of mass in the lithosphere–mantle system

$$\boldsymbol{\nabla}\cdot(\boldsymbol{u} + \boldsymbol{q}) = M - E, \tag{3.4}$$

where I have assumed that the total fraction of Io occupied by the plumbing system is negligible. The flux of material in the plumbing system $\boldsymbol{q}_p$ increases when material is extracted from the mantle and decreases when material is emplaced back into the lithosphere (this can be compared to the standard two-phase continuity equation (2.9)). Conservation of mass in the plumbing system is therefore given by

$$\boldsymbol{\nabla} \cdot \boldsymbol{q}_p = E - M. \tag{3.5}$$

I assume that the magma in the plumbing system is at the melting point T_m. I consider three different parametrisations for emplacement. The first (and primary) formulation parameterises the emplacement rate based on the temperature difference to the host material at temperature T,

$$M = \begin{cases} \frac{hC(T_m - T)}{L} & T > T_e, \\ 0 & T < T_e, \end{cases} \tag{3.6}$$

where C is the specific heat capacity, L is the latent heat, h is an emplacement rate constant (units s^{-1}) and T_e is the elastic-limit temperature. Regions of the lithosphere colder than the elastic-limit temperature are assumed to be brittle; magma propagates through these without permanent emplacement. This assumption is introduced to highlight and investigate the importance of the distribution of magmatic emplacement in controlling the lithospheric temperature profile. The detailed mechanisms of dike propagation and emplacement are subsumed in this parametrisation. I treat h as a free parameter and explore the model's behaviour for a wide range of values.

The other two parametrisations of emplacement that I investigate are more simple than the first. They consider emplacement to be proportional to the magnitude of the flux of material in the plumbing system, or a constant respectively

$$M = \begin{cases} \lambda_q \left|\boldsymbol{q}_p\right| & T > T_e, \\ 0 & T < T_e, \end{cases} \tag{3.7a}$$

$$M = \begin{cases} \lambda_c & T > T_e, \\ 0 & T < T_e, \end{cases} \tag{3.7b}$$

where λ_q and λ_c are constants to be explored; they are similar to h in that they control of the magnitude of emplacement, but have different units and different numerical values, and so are given different symbols. I retain the temperature cut-off T_e such that the effect of the distribution of emplacement can still be explored.

A parametrisation of emplacement based on temperature (equation (3.6)) can be thought of as representing conduction in the vicinity of a propagating dike. The dike loses heat at a rate related to the temperature difference, and it is this energy loss that drives freezing. The other two parametrisations are more simple than the first. It is feasible that as volcanic flux increases, contact area with the host rock increases, leading to an increase in emplacement. This is the rationale before the flux-proportional formulation. The constant emplacement rate formulation is a simplification of each of the other parametrisations, where emplacement is assumed to be at a constant rate when averaged over long timescales. I investigate these different parametrisations to see whether the exact form of emplacement plays an important role in determining internal structure.

Extraction of liquid from the mantle into the plumbing system is expected to take place at the top of the partially-molten mantle. I assume that this transfer is a function of liquid overpressure,

$$E = \begin{cases} \nu(P - P_c) & P > P_c, \\ 0 & P < P_c, \end{cases} \tag{3.8}$$

where ν is an extraction rate constant (units $\mathrm{s}^{-1}\mathrm{Pa}^{-1}$) and P_c is a critical overpressure that liquid must attain in order to be extracted into the plumbing system. Liquid overpressure (compaction pressure) is related to the compaction rate $\boldsymbol{\nabla} \cdot \boldsymbol{u}$ by the relationship (McKenzie, 1984)

$$P = \zeta \boldsymbol{\nabla} \cdot \boldsymbol{u}, \tag{3.9}$$

where $\zeta = \eta/\phi$ is the compaction viscosity, related to the shear viscosity η. This form of the compaction viscosity is commonly assumed, but other forms have been proposed with a weaker singularity as $\phi \to 0$ (Rudge, 2018).

I model heat transport in the lithosphere and mantle of Io together, using an enthalpy method (Katz, 2008) so that no boundary conditions need be imposed an the lithosphere–mantle boundary (see section 2.3). Conservation of energy requires

$$\frac{1}{\rho C}\frac{\partial H}{\partial t} + \boldsymbol{\nabla}\cdot[(\boldsymbol{u}+\boldsymbol{q})T] + \boldsymbol{\nabla}\cdot\left[(\phi\boldsymbol{u}+\boldsymbol{q})\frac{L}{C}\right] = \boldsymbol{\nabla}\cdot(\kappa\boldsymbol{\nabla}T) + \frac{\psi}{\rho C} - E\left(T + \frac{L}{C}\right) + M\left(T_m + \frac{L}{C}\right), \tag{3.10}$$

where bulk enthalpy is defined as $H = \rho CT + \rho L\phi$, and κ is the thermal diffusivity. I note here that I have made the assumption that the specific heat capacity is constant between absolute zero and T_m (see the discussion following equation (2.20)). Changes in bulk enthalpy are caused by advection of sensible heat, advection of latent heat, diffusion, tidal heating, extraction of melt, and emplacement of melt, which are represented respectively by each term in equation (3.10). The integral of the tidal heating rate ψ over silicate Io gives the total tidal heating input Ψ, which I take to be 1×10^{14} W (Lainey et al., 2009).

The required boundary conditions for the system are

$$\begin{aligned} \boldsymbol{q} = 0, \quad \boldsymbol{q}_p = 0, \quad \frac{\partial H}{\partial r} = 0, \quad \frac{\partial P}{\partial r} &= -(1-\phi)\Delta\rho\boldsymbol{g} \quad \text{at } r = r_m, \\ H = T_s, \quad \boldsymbol{u} &= -\boldsymbol{q}_p \quad \text{at } r = R. \end{aligned} \tag{3.11}$$

At the base of the domain there is no solid or liquid flow — I assume that there is no transfer of material across the core-mantle boundary, justified by the large and stable density difference expected between an Fe-rich core and a silicate mantle. The volcanic plumbing flux is by definition zero at the base of the domain. I assume that there is no energy flow

Table 3.1: Dimensional parameters

Quantity	Symbol	Definition	Preferred Value	Units
Radial position	r			m
Radius	R		1820	km
Core radius[1]	r_m		700	km
Lithosphere radius	r_l			m
Boundary layer coordinate	Z			m
Solid velocity	u			m/s
Segregation flux	q	$q = \phi(v-u)$		m/s
Volcanic plumbing flux	q_p			m/s
Porosity	ϕ			
Permeability constant[2]	K_0	$K = K_0\phi^n$	10^{-7}	m^2
Permeability exponent[2]	n	see above	3	
Density	ρ		3000	$\mathrm{kg/m^3}$
Density difference	$\Delta\rho$		500	$\mathrm{kg/m^3}$
Gravitational acceleration	g		1.5	$\mathrm{m/s^2}$
Shear viscosity	η		1×10^{20}	Pas
Liquid viscosity	η_l		1	Pas
Volume transfer rate	Γ			s^{-1}
Emplacement rate*	M	$M = hC(T_m - T)/L$		s^{-1}
Emplacement constant	h	see above	7	Myr^{-1}
Alt emplacement constant	λ_q	$M = \lambda_q q_p$		m^{-1}
Alt emplacement constant	λ_c	$M = \lambda_c$		s^{-1}
Extraction rate	E	$E = \nu(P - P_c)$		s^{-1}
Extraction constant	ν	see above	1.4×10^{-5}	$\mathrm{Myr^{-1}Pa^{-1}}$
Compaction pressure	P	$P = \zeta \boldsymbol{\nabla} \cdot \boldsymbol{u}$		MPa
Critical overpressure	P_c		5	MPa
Compaction viscosity	ζ	$\zeta = \eta/\phi$		Pas
Temperature	T			K
Elastic limit temperature	T_e		1000	K
Melting temperature	T_m		1500	K
Surface temperature	T_s		150	K
Thermal diffusivity	κ		10^{-6}	$\mathrm{m^2/s}$
Latent heat	L		4×10^5	J/Kg
Specific heat capacity	C		1200	J/Kg/K
Total tidal heating[3]	Ψ		1×10^{14}	W
Tidal heating rate**	ψ		4.2×10^{-6}	$\mathrm{W/m^{-3}}$

[1] Bierson and Nimmo (2016), [2] Katz (2008), [3] Lainey et al. (2009)

* Alternative forms for the emplacement rate are considered in (3.7a) – (3.7b)

** Ψ divided by the volume of silicate Io

across the core-mantle boundary, and so enforce zero gradient on enthalpy. This condition on enthalpy means that porosity may not be precisely zero at the core-mantle boundary. This is the source of the condition on compaction pressure, which comes from equation (3.1) and the condition that the Darcy flux must equal zero at the base of the domain even if porosity is non-zero. At the surface, enthalpy is set to the surface temperature T_s. This condition means that porosity, Darcy segregation flux, and the compaction pressure are also zero at the surface. The solid velocity at the surface is the negative of the surface plumbing system flux. This ensures conservation of mass and can be seen through the sum of equations (3.4) and (3.5).

3.2.2 Solution methods

The full model to be solved comprises the enthalpy equation (3.10) for H, the combination of equations (3.1) and (3.9) in a compaction equation for P and $\boldsymbol{q}$, total mass conservation (3.4) for $\boldsymbol{u}$, and conservation of mass in the plumbing system (3.5) for $\boldsymbol{q}_p$. The enthalpy solution gives ϕ and T through the definition of bulk enthalpy $H = \rho C T + \rho L \phi$, by assuming that temperature is buffered to the melting point when enthalpy exceeds that of the melting temperature; melt fraction is zero wherever temperature falls below the melting point. Parameter values are given in table 3.1. The system is scaled (see Appendix 3.A) and solved using the Portable, Extensible Toolkit for Scientific Computation (PETSc) (Balay et al., 2020, 2019, 1997). Robust convergence is obtained by splitting the system of governing equations into three non-linear problems for enthalpy, pressure, and plumbing-system flux. These are solved iteratively at each timestep until the ℓ_2-norm of their residual vectors are all below a small tolerance (10^{-7}). I run the model to steady state and report the final, steady solutions. To facilitate exploration of the parameter space, I employ an asymptotic approximation of these solutions. This is developed in Appendix 3.B.

3.3 Results

A representative solution of the model is plotted in figure 3.2. This representative solution uses the temperature dependent parametrisation of the emplacement rate (equation (3.6)). Panel (a) shows that melt upwells throughout the mantle and the solid correspondingly downwells. This process, driven by magmatic buoyancy, results in relatively low melt fractions ($\sim 3\%$) except in a thin boundary layer beneath the lithosphere that I discuss below. Magma that reaches the surface solidifies and cools to the surface temperature (with the heat released to space). The continual eruption and burial of the surface causes the lithosphere to downwell, balancing the upward flux of magma in the plumbing system. The downwelling lithosphere advects the cold surface temperature into the interior, resulting in a relatively cold upper lithosphere, capable of supporting Io's mountains. As the lithospheric material continues to downwell through the lower lithosphere, it is heated by magmatic emplacement (the formation of plutonic intrusions) and eventually reaches the solidus, where it starts to melt. The balance between downward advection of the cold surface temperature, and intrusive heating, results in a steady lithospheric thickness being maintained. A steep temperature gradient arises in the lithosphere (fig. 3.2b) between the upper lithosphere, where heat transport is dominated by the downward advection of cold lithosphere, and the lower lithosphere, where emplacement causes significant heating. Throughout most of the underlying mantle, liquid pressure is low, causing the solid matrix to compact (fig. 3.2d). Approaching the lithosphere boundary, liquid pressure increases and causes the decompaction of the downwelling lithospheric material.

I now explore the behaviour of the model. I first investigate the effect of the parameters associated with the volcanic plumbing system, utilising the temperature dependent form of emplacement, before exploring alternative parametrisations of emplacement. I then explore material and rheological parameters.

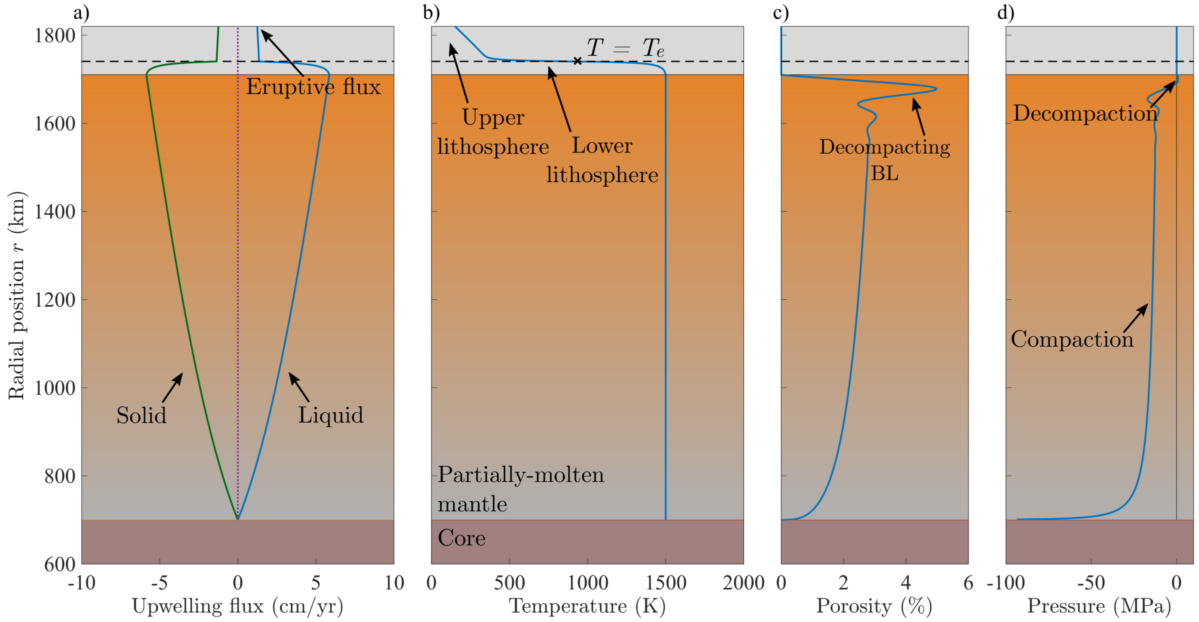

Figure 3.2: Example solution to the model with $h = 7$ Myr^{-1}, $T_e = 960$ K. a) Upwelling magma is replaced by downwelling solid. b) The lower lithosphere ($T > T_e$) is heated by magmatic intrusions (emplacement), but the upper lithosphere ($T < T_e$) is cold due to the downwelling cold surface material. c) Melt fractions are low throughout the mantle but increase in a thin boundary layer on the order of 50 km thick. d) Compaction occurs throughout most of mantle as the liquid is at low pressure, but beneath the lithosphere $P \simeq P_c = 0.8$ MPa, and downwelling solid is decompacted by liquid pressure. The elastic thickness (defined at a homologous temperature of 0.6 T_m) is 80 km and the eruption rate is 1.25 cm/yr, with 99.5% of heat transport through the surface being volcanic. Parameter values can be found in table 3.1.

3.3.1 Dependence on volcanic plumbing system parameters

The main parameters that control the behaviour of the volcanic plumbing system are the emplacement rate constant h, and the elastic limit temperature T_e. The behaviour of the system for three values of emplacement rate constant h and elastic-limit temperature T_e is shown in figures 3.3 – 3.4, where I am using the temperature dependent form for emplacement (equation (3.6)). The solid lines are the full, numerical solutions to the model and the dashed lines are from the asymptotic approximation (see Appendix 3.B).

Figure 3.3 demonstrates that the rate of magmatic emplacement exerts a strong control on Io's lithospheric thickness. When the emplacement rate is zero (fig. 3.3, $h = 0$), magma does not re-heat the sinking lithosphere and therefore the cold surface material downwells far into the mantle before it is heated to its melting point (by basal conduction and tidal heating only), producing a > 600 km thick lithosphere. Conversely, when emplacement is rapid, the lithosphere is very quickly heated to its melting point and therefore is thin. Figure 3.3e shows how the volcanic plumbing flux changes through the lithosphere. When there is no emplacement, the drop in volcanic plumbing flux is purely due to radial spreading.

Figure 3.4 shows the effect of increasing the elastic-limit temperature T_e. When T_e is low, emplacement can take place throughout a large portion of the lithosphere. This causes most of the lithosphere to be hot (fig 3.4, $T_e = 825$ K) and thus the elastic thickness is small. Increasing T_e leads to the growth of a large, cold upper lithosphere where no emplacement is taking place. This provides a large elastic thickness capable of supporting Io's mountains. Figure 3.4e shows that the total amount of material being emplaced at steady-state does not significantly change as T_e is increased, and the thickness of the emplacement region ($T > T_e$) is roughly constant as T_e increases. As I will discuss in section 3.4.1, the total amount of erupted and emplaced material is controlled by a global energy balance.

To comprehensively map the parameter space of T_e and h I utilise the asymptotic approxima-

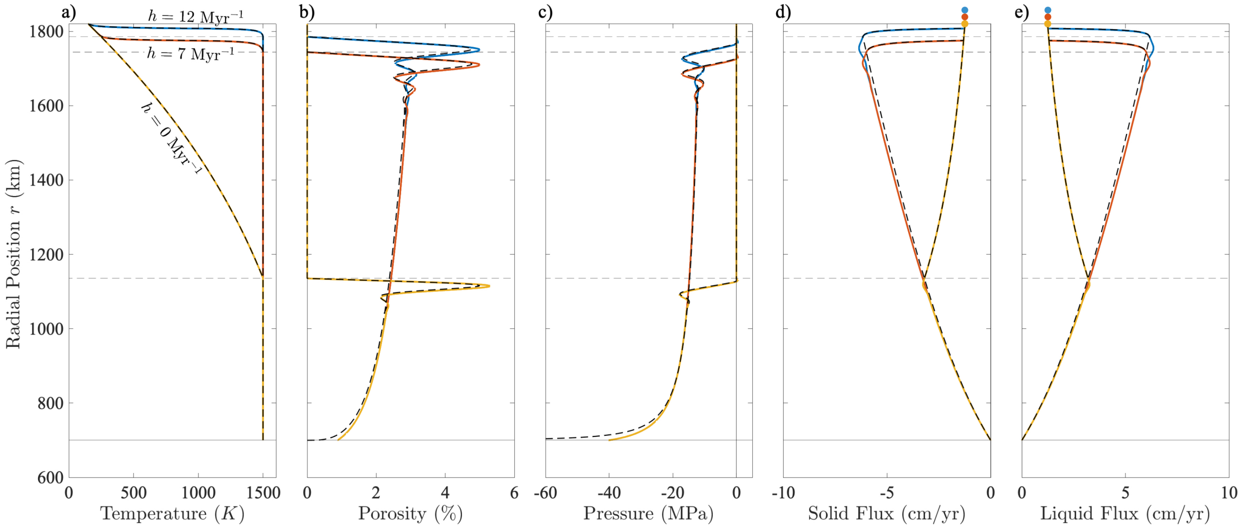

Figure 3.3: The effect of emplacement rate h on a) temperature profile, b) porosity distribution, c) compaction pressure, d) solid and e) liquid fluxes. Solid lines are full solutions to the model, and heavy dashed lines are the approximate solutions. Thin dashed lines mark the lithosphere–mantle boundaries. Dots on panels d and e show the surface erupted fluxes. When there is no magmatic emplacement ($h = 0$), the lithosphere grows to be over 600 km thick due to the rapid downwelling of the cold surface temperature. As emplacement rate is increased, the heating that this provides to the lithosphere can increasingly balance the cold downwelling surface temperature, resulting in smaller lithospheric thicknesses. $T_e = 960$ K in these solutions, and I use the temperature dependent form for emplacement. Liquid flux is the sum of the segregation flux q and plumbing-system flux q_p. Parameters values can be found in table 3.1.

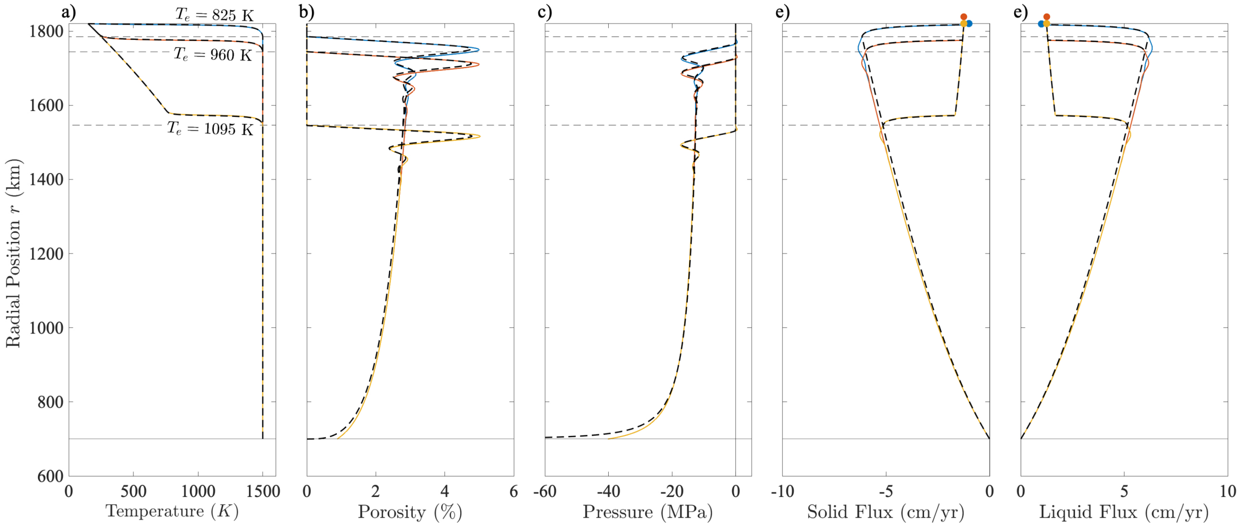

Figure 3.4: The effect of elastic limit temperature T_e on a) temperature profile, b) porosity distribution, c) compaction pressure, d) solid and e) liquid fluxes. Solid lines are full solutions to the model, and heavy dashed lines are the approximate solutions. As the elastic limit temperature T_e is increased, lithospheric thickness increases and a larger proportion of the upper lithosphere is cold, resulting in larger elastic thicknesses. $h = 7$ Myr^{-1} in these solutions, and again I use the temperature dependent form for emplacement.

tion of the steady solution. Figures 3.3 – 3.4 show that there is good agreement between the full solutions and the asymptotic approximation. Figure 3.5 shows how (a) elastic thickness (defined at a homologous temperature of 0.6 T_m), (b) eruption rate, and (c) volcanic heat flux vary as a function of the emplacement rate constant h and elastic-limit temperature T_e. Figure 3.5 confirms the trends seen in figures 3.3 and 3.4, and places them in the context of observable features. The blue region in figure 3.5 indicates the parameter space that gives reasonable elastic thicknesses (10 – 100 km) at reasonable brittle–ductile transition temperatures (homologous temperature 0.5 – 0.7 T_m). Figure 3.5a shows that the elastic thickness varies rapidly with relatively small changes in T_e and h around the main solution (the central star, plotted in fig. 3.2). Elastic thickness is thus the most useful observation for constraining the characteristics of Io's volcanic plumbing system. Figure 3.5b shows that eruption rate reaches a maximum of $\sim$ 1.25 cm/yr over much of the parameter space, a value that is discussed further below. The conductive heat flux in this part of the parameter space is negligible (fig. 3.5c) as virtually all of the input tidal heating is lost in eruptions. Figure 3.5b shows that if emplacement rate is very high and takes place through the majority of the lithosphere, eruption rate goes to zero. All heat is lost by conduction through a thin lid in this case.

3.3.2 Alternative forms for emplacement

I now investigate the effects of changing the parametrisation of emplacement used in the model. Figure 3.6 shows how the three different emplacement formulations compare: temperature dependent emplacement rate (equation (3.6)), volcanic flux dependent emplacement rate (equation (3.7a)), and constant emplacement rate (equation (3.7b)). The top row of figure 3.6 show how the emplacement formulations control the lithospheric temperature profile and volcanic flux when the elastic limit temperature $T_e = 0$. The bottom row of figure 3.6 shows the same, but when $T_e = 0.6\ T_m$. The relevant emplacement rate constants (h, λ_q,

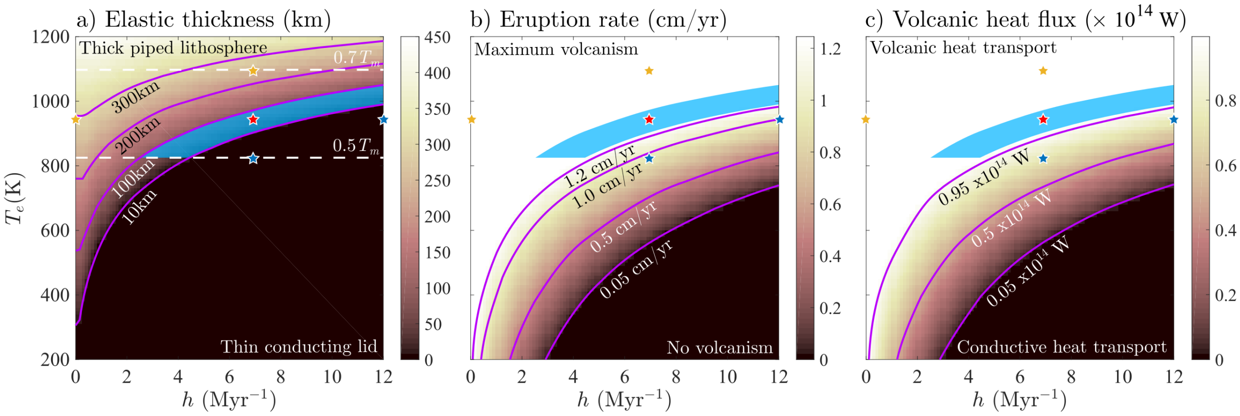

Figure 3.5: Model predictions of a) elastic thickness, b) eruption rate, and c) volcanic heat flux in the parameter space of emplacement constant h and elastic limit temperature T_e. The dashed lines on panel a) mark homologous temperatures 0.5 T_m and 0.7 T_m, an estimated range for the transition from brittle to ductile behaviour. The blue region covers the parameter space for potential elastic thicknesses (10 – 100 km). The central red star marks the solution displayed in figure 3.2, and other stars mark the solutions in figures 3.3 and 3.4.

λ_c) were chosen to give a uniform lithosphere thickness of 80 km, allowing the formulations to be compared.

If the elastic limit temperature $T_e = 0$ (or T_e is low, as seen in figures 3.4 – 3.5), a temperature dependant formulation of the emplacement rate predicts a hot upper lithosphere that would be incapable of supporting Io's high mountains. If, however, emplacement rate is proportional to the plumbing system flux or is a constant, the upper lithosphere is expected to retain some strength even if emplacement is allowed to take place up to the surface (figure 3.6a, shown by the intermediate temperatures in the upper lithosphere for these emplacement formulations). When the elastic limit temperature is high $T_e = 0.6$, however, these formulations of emplacement predict very sharp temperature gradients and drops in plumbing system flux within a small portion of the lower lithosphere (figure 3.6c–d).

The primary features of the different emplacement parametrisations are broadly the same. A high emplacement rate results in a thin lithosphere, and if emplacement is concentrated in the lower lithosphere, the upper lithosphere is strongest and most able to support Io's high mountains. Given these broad similarities and the lack of a means to constrain h, λ_c, or λ_q

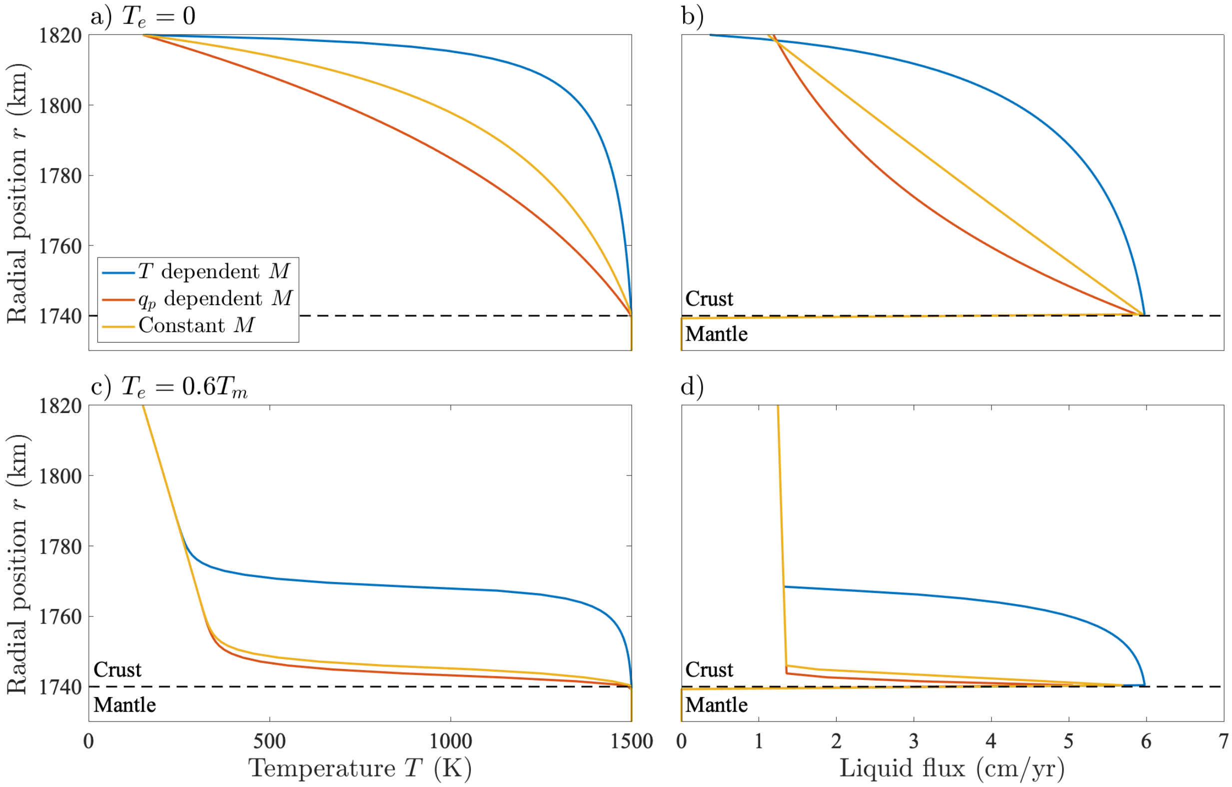

Figure 3.6: The effect of using different parametrisations for emplacement rate M on the lithospheric temperature profile (panels a and c) and volcanic flux (panels b and d) for two values of the elastic limit temperature T_e. If there is no elastic cut-off temperature for emplacement ($T_e = 0$), a temperature dependent formulation predicts a much weaker upper lithosphere than flux dependent or constant emplacement formulations. If a reasonable temperature for the transition from brittle to ductile behaviour is used ($T_e = 0.6T_m$), flux dependent or constant emplacement formulations predict very sharp temperature gradients and changes in magma flux near the base of the lithosphere. The temperature dependent emplacement rate is defined in equation (3.6), the volcanic flux dependent rate is defined in equation (3.7a), and the constant rate is defined in (3.7b). Parameter values h, λ_q and λ_c — which control the emplacement rate in each formulation — are chosen to give a lithospheric thickness of ~ 80 km at the relevant value of T_e.

based on physical processes, I will continue my analyses using the temperature dependent formulation.

3.3.3 Dependence on material and rheological parameters

I now examine the effects of varying material and rheological parameters in the model. Figure 3.7 shows solutions of porosity and pressure for a range of critical compaction pressures P_c, and figure 3.8 shows solutions of porosity for a range of matrix shear viscosities η and liquid visosities η_l. I consider the critical overpressure P_c to be a material parameter as it parameterises the strength of the downwelling lithosphere.

Pressure differences between the solid and liquid in the partially molten rock causes the solid matrix to deform. When the solid pressure is higher, the matrix compacts, expelling liquid, and when the liquid pressure is higher, the solid decompacts and melt accumulates. Away from boundary layers, the melt fraction is almost entirely controlled by the buoyant segregation of magma. Figures 3.7 and 3.8a show that P_c and η do not affect the melt fraction outside of boundary layers, while figure 3.8b shows that increasing the liquid viscosity η_l increases melt fractions throughout the mantle. This is because the buoyancy-driven melt fraction is controlled by the permeability and liquid viscosity in Darcy's law (3.1).

As solid lithosphere downwells, warms, and begins to melt, the high pressure of rising magma forces the solid matrix to decompact to accommodate infiltration of buoyant magma. This decompaction occurs over a region known as a decompacting boundary layer, in which the compaction pressure gradient term in Darcy's law (3.1) becomes important. Figure 3.7 shows that if a large compaction pressure (liquid overpressure) is required for magma to move out of the mantle pore-space into the plumbing system, large porosities build up beneath the lithosphere. This is because the large liquid overpressure drives rapid decompaction of the downwelling solid material. High shear viscosities also lead to the development of a larger boundary layer with a higher peak porosity (fig. 3.8a). An increased shear viscosity (and so through $\zeta = \eta/\phi$, an increased bulk viscosity) causes greater resistance of the downwelling matrix to compaction, which means a larger length scale over which the compaction pressure gradient counteracts buoyancy, and in which the porosity must therefore increase to enable upward melt motion. The thickness of the boundary layer is on the order of the compaction length, which is an emergent length-scale governing the interaction of liquid and solid in a two-phase medium (McKenzie, 1984).

The interaction between compaction pressure driving melt flow and compaction sets up an oscillation of the porosity and pressure (Spiegelman, 1993) that decays to match the buoyancy-dominated mantle region below. The wavelength of these oscillations is set by the compaction length. This can be seen in figure 3.8 where a lower shear viscosity (and hence a smaller compaction length, table 3.A.1) results in a shorter wavelength of oscillations. Figure 3.8 shows that high shear viscosities and low magma viscosities (both of which represent high bulk viscosities) damp porosity oscillations effectively so that porosity rapidly relaxes to the buoyancy-driven profile.

In figures 3.7 and 3.8 the location of the lithosphere–mantle boundary and the flux of melt out of the mantle are not affected by the parameter changes (where porosity increases, melt velocity decreases and so the flux is unchanged). As such, the material parameters control the form of the decompacting boundary layer and the underlying porosity, but do not affect the lithosphere or volcanic plumbing system. In particular, and perhaps surprisingly, the value of P_c, which encodes information about the strength of the lithosphere in this model, does not significantly affect the lithospheric thickness.

3.4 Discussion

My results demonstrate the importance of magmatic intrusions (emplacement) in controlling Io's lithospheric thickness and temperature profile. A significant proportion of magmas generated in the mantle must contribute to heating the cold downwelling lithosphere — otherwise it would be extremely thick. Further, the intrusions must be concentrated in the lower lithosphere if the upper lithosphere is to retain significant elastic strength, which it requires to support Io's high mountains (McKinnon et al., 2001). The results also suggest that a high-melt-fraction layer can develop beneath Io's lithosphere due to decompaction, without requiring any radial partitioning of tidal heat. I now discuss these results further and consider their implications.

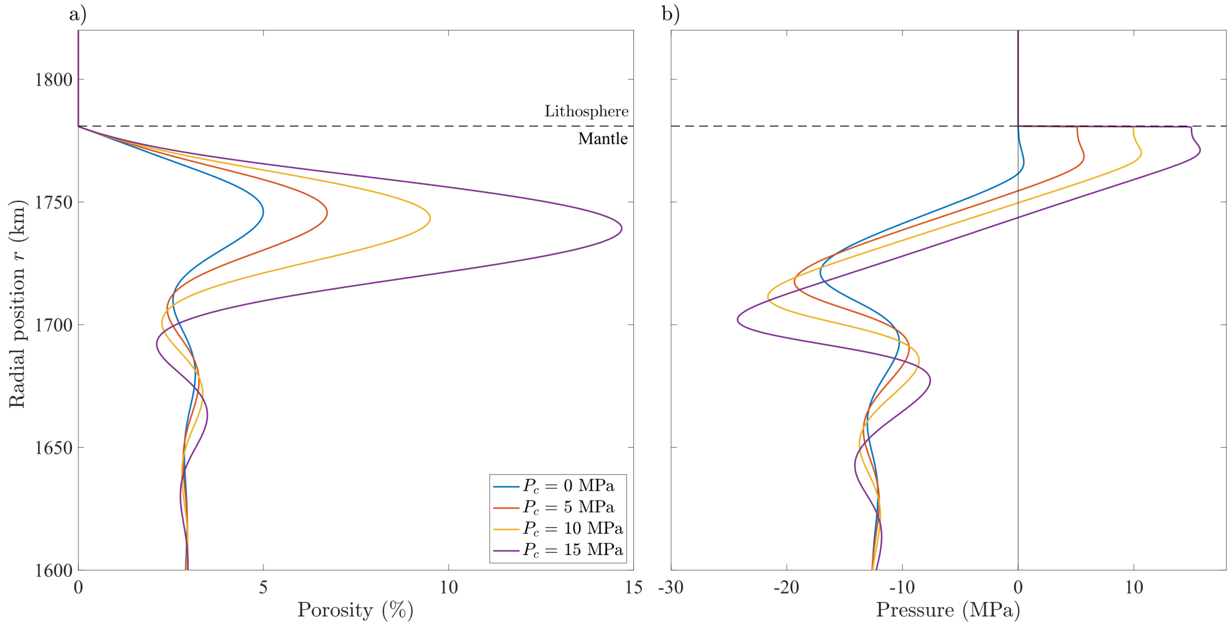

Figure 3.7: a) Porosity and b) compaction pressure in the decompacting boundary layer beneath the lithosphere for different values of critical compaction pressure P_c. High values of P_c cause the material downwelling from the lithosphere to decompact rapidly, leading to the accumulation of large amounts of melt. Note the different radial scale from other figures.

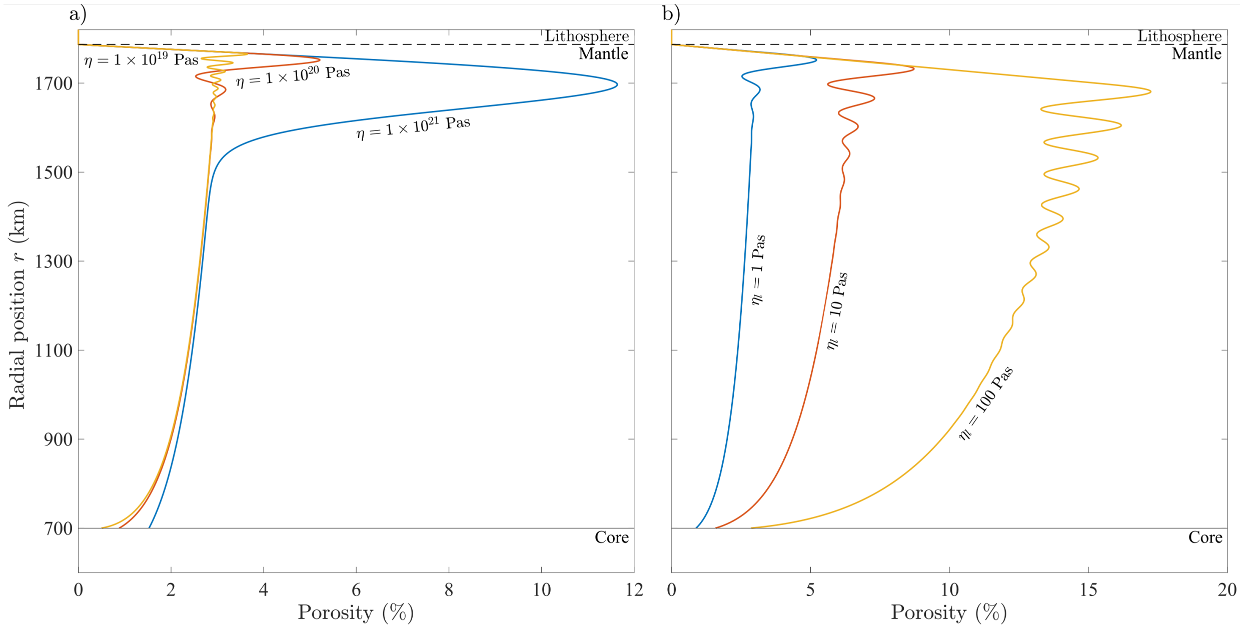

Figure 3.8: Porosity distribution for varying a) shear viscosity and b) melt viscosity. High shear viscosities cause thick decompacting boundary layers with high peak porosities. High melt viscosities cause high-melt-fractions throughout the mantle as melt can less easily segregate. High shear viscosity and low melt fractions increase the bulk viscosity, damping porosity oscillations.

3.4.1 Magmatic intrusions

The foremost result of this chapter is captured in figure 3.5, which indicates that magmatic intrusions are the primary control on Io's lithospheric thickness. Models of heat piping that neglect heating from intrusions will result in steady-state lithospheric thicknesses of over 600 km. Models with a downwelling lithosphere that fix the lithospheric thickness cannot be assumed to be in thermal steady state and may violate energy conservation. The primary control on the temperature profile in Io's lithosphere is the distribution of magmatic emplacement. Unless intrusions are confined to the lower lithosphere, the upper lithosphere becomes hot and weak, so would be unable to support significant topography. With a sufficiently large elastic-limit temperature, colder regions (in the upper lithosphere) have no emplacement and so remain strong. Kirchoff et al. (2020) note that the release of confining stress by lithospheric faults leads to extension in Io's upper lithosphere, which manifests as rifts, pull-apart basins, and simple graben structures. This transition to an extensional regime may further explain the low level of emplacement that must be taking place in the upper lithosphere, with magmas instead rising all the way to the surface. A more detailed description of heat piping might attempt to account for the mechanics and energetics of emplacement in the context of the lithospheric stress profile.

The relevant parametrisation for emplacement is not known, but figure 3.6 shows that three reasonable parametrisations all produce the same broad behaviour; high emplacement rates lead to a thin lithosphere, and predominantly lower-lithosphere emplacement produces a strong upper lithosphere. To rigorously identify the most relevant emplacement parametrisation would likely require a close knowledge of the temperature distribution in Io's lithosphere. This is out of reach of current or planned observations. I favour the temperature dependent form of emplacement because it does not predict very sharp temperature gradients or changes in volcanic flux in the lower lithosphere (figure 3.6). In other applications where simplicity is the priority, a constant emplacement rate or one proportional to the plumbing flux may well be preferable.

Unless the lithosphere is unrealistically thin, my model shows that conductive heat loss at the surface is negligible (fig. 3.5c), consistent with the conclusions of O'Reilly and Davies (1981). As shown in more detail in Appendix 3.C, the heat loss due to eruption is $q_s(\rho L+\rho C(T_m-T_s))$ per unit surface area, where q_s is the globally averaged eruption rate, ρL is the latent heat of erupted magma, and $\rho C(T_m - T_s)$ is the sensible heat lost as erupted magma cools to the surface temperature T_s. At steady state, with negligible conduction through the elastic lithosphere, this surface heat flux must balance the total dissipation rate Ψ, implying a volcanic resurfacing rate

$$4\pi R^2 q_s = \frac{\Psi}{\rho L + \rho C(T_m - T_s)}. \tag{3.12}$$

For Io, equation (3.12) predicts a resurfacing rate of 1.25 cm/yr (Breuer and Moore, 2015); this is the maximum rate seen in figure 3.5b. Equation (3.12) also provides a means of estimating eruption rates for other tidally heated lava-worlds, utilising their tidal heating rate, size, and surface temperature, all of which are obtainable from observations (Bolmont et al., 2013). In particular I note the potential application of equation (3.12) — and the model in general — to the TRAPPIST-1 planets, which are undergoing comparable levels of tidal heating with moderate surface temperatures (150–400 K) (Barr et al., 2018).

The predicted eruption rate can be compared to an estimate of the total melt production rate. Assuming that all tidal heating directly causes melting, the total melt production rate is $\Psi/\rho L$. The predicted eruption rate is therefore less than the melt production rate by a factor of $C(T_m - T_s)/(L + C(T_m - T_s))$. For Io, this indicates that around 80% of magma must be emplaced into the crust. This analysis demonstrates that the eruption rate and the total amount of emplaced material are controlled by the tidal heating rate and the relative temperatures of the magma and the surface. This explains why these quantities remain almost unchanged in figures 3.3 and 3.4, despite significant differences in the thickness of the lithosphere and the precise location at which emplacement occurs. Equation (3.12) also shows that if the total heating rate Ψ is increased, it results in a proportional increase in both the eruption rate and the intrusive emplacement rate.

3.4.2 Magma-rich layer beneath the lithosphere

Figures 3.7 and 3.8 demonstrate that if a high-melt-fraction layer exists within Io, it does not necessarily imply the presence of a magma ocean with melt fractions above disaggregation (Khurana et al., 2011; Tyler et al., 2015), nor was it necessarily formed by concentrated tidal heating (Moore, 2001; Bierson and Nimmo, 2016). Instead, my model suggests that a high-melt-fraction layer could form if a large liquid overpressure is required in order to inject dikes into the lithosphere, or if the compaction length is large.

McKinnon et al. (2001) and Kirchoff and McKinnon (2009) note that high compressive stresses must arise in Io's lithosphere due to the downwelling of a spherical shell. If these compressive stresses are present at the lithosphere–mantle boundary, they will have to be overcome by magma pressure to form dikes; this would indicate a high value for P_c, promoting the formation of a high-melt-fraction region beneath the lithosphere. However, I have demonstrated that Io's lower lithosphere must be hot due to extensive magmatic intrusion, and so it is likely that the stresses associated with downwelling lithosphere would be accommodated by faulting in the upper lithosphere and viscous creep in the lower lithosphere. The relevant value for P_c in the model is thus unclear; more investigation is needed into the strength and deformation mechanisms of Io's lithosphere.

Nevertheless, I have demonstrated that a high-melt-fraction layer can in principle arise from a state of uniform tidal heating. Further work is needed to ascertain whether such a layer is likely to exist. In particular, it must determine whether the required high shear viscosities are compatible with the observed tidal heating (Bierson and Nimmo, 2016; Renaud and Henning, 2018). If such a layer does not exist, my model suggests that melt fractions are relatively uniform within Io (fig. 3.8), providing little drive for radial partitioning of tidal heating. The most promising means for investigating Io's dissipation structure (aside from improved gravity and induction measurements) remains the search for its signature in three-dimensional patterns of surface features (e.g., Rathbun et al., 2018; Cantrall et al., 2018). This will be discussed in detail in Chapter 5.

At this point I emphasise that the presence and form of the decompacting boundary layer are independent of the model predictions for lithospheric thickness. In the context of my model, a decompacting boundary layer is a feature beneath the lithosphere that does not affect the mass or heat fluxes out of the mantle, nor how energy is deposited in the lithosphere; it is these factors that control Io's lithospheric thickness.

3.4.3 Model limitations

A primary simplification made in formulating this model was my assumption of spherical symmetry. As described in Chapters 1 and 2, tidal heating does not just vary with radius but also with latitude and longitude. Steinke et al. (2020) show that if dissipation is significantly concentrated in a layer beneath the lithosphere (termed crust in that work), lateral variations in mantle temperature can exceed 100 K, perhaps impacting the usefulness of a one-dimensional approach. More distributed heating leads to much lower lateral mantle temperature variations (~ 1 K, Steinke et al., 2020), but may still cause significant lateral variations in melting rate. The presence or absence of a dissipative layer is thus key to understanding Io's three-dimensional tidal heating distribution.

Convection of the partially molten mantle is also a potentially important three-dimensional effect. If buoyant segregation is inefficient at transporting heat, convection of the two phase medium could occur and imprint deviations from the one-dimensional model presented here. Further, compositional effects may lead to thermochemical convection (see Chapter 4 for a discussion). However, I stress that convection cannot dominate Io's mantle heat transport due to its low efficiency at melt fractions relevant for Io (Breuer and Moore, 2015). Also neglected here is that compaction effects can cause the lateral migration and focusing of melt (Sparks and Parmentier, 1991; Turner et al., 2017), which could lead to channelisation of melt and may exert a control on Io's volcano distribution. My model represents a long-term average resurfacing rate that is spatially uniform. Volcanic eruptions are discrete events in both space and time, so at any given instant the eruption and resurfacing rate will not be spatially uniform. My model does not resolve the details of the eruption process, which are likely to include shorter time-scale variability in both space and time around the average rate. As such some caution is required in comparing detailed observations of the current surface heat flux and eruption rate with that predicted by the model.

Another key simplification in this model is the assumption that Io is composed of a single chemical component. Continued melting in the interior is likely to have caused significant chemical stratification (Keszthelyi and McEwen, 1997). Melting of a polymineralic rock occurs over a range of temperatures, with more fusible minerals melting first. The upward migration and eruption of fusible melts plausibly depletes the deep mantle of fusible material and enriches the near-surface. Interesting is the lack of observed olivine in surface erupta (Keszthelyi et al., 2004), indicating either that deep refractory melts do not form, that they predominantly freeze in the interior, or that they evolve significantly in the lithosphere. Erupted fusible material would also melt at shallow depths upon burial, affecting the lithospheric thickness. How magmatism and volcanism control chemical evolution is the subject of Chapter 4.

3.5 Conclusions

Io is a body that is complicated in its detail but observations suggest it has a simple structure at leading order. In this chapter I have demonstrated that a coupled model of magmatic segregation, compaction, and heat-piping can explain this leading-order structure and the associated observations: globally averaged elastic thickness, eruption rate, and surface heat flux, as well as a possible high-melt-fraction layer beneath the lithosphere. I have shown that magmatic intrusions into Io's lithosphere are a fundamental control on its lithospheric thickness. Without the heating associated with the formation of magmatic intrusions, the lithosphere would grow to be > 600 km thick. However, these intrusions must be confined to the lower lithosphere if the upper lithosphere is to retain sufficient strength to support Io's high mountains. I have also shown that an inferred high-melt-fraction region can be understood as a decompacting boundary layer if a process such as lateral compression makes it difficult for magma to migrate from the partially-molten mantle into the lithosphere. An extension of this model to include more elaborate chemical thermodynamics and non-uniform tidal dissipation will given further insights into how this system operates, and begin to give insight into the deviations from the spherically symmetric view I have presented.

Appendix

3.A Model scaling and non-dimensional parameters

Here I non-dimensionalise the governing equations. Dimensional parameter definitions are given in table 3.1, and the scales and definitions of the non-dimensional parameters are given in table 3.A.1. I write for example $u = u_0\hat{u}$, where u_0 is the velocity scale and $\hat{u}$ is the dimensionless velocity, insert similar expressions for all the variables into the equations, and finally drop the hats on the dimensionless quantities to arrive at a dimensionless model. For the temperature I write $T = T_s + T_0\hat{T}$ with $T_0 = T_m - T_s$ so that the non-dimensional temperature varies between 0 and 1. I also assume spherical symmetry, and write all quantities as a function of r, noting that $\boldsymbol{\nabla} \cdot \boldsymbol{u} = r^{-2}\ \partial(r^2 u)/\partial r$ where u is the radial component of the solid velocity.

The non-dimensional equations for conservation of solid and liquid mass are

$$\frac{\partial}{\partial t}(1-\phi_0\phi) + \frac{1}{r^2}\frac{\partial}{\partial r}\left(r^2(1-\phi_0\phi)u\right) = -\Gamma + M, \tag{3.13}$$

$$\phi_0\frac{\partial \phi}{\partial t} + \frac{1}{r^2}\frac{\partial}{\partial r}\left(r^2(\phi_0\phi u + q)\right) = \Gamma - E, \tag{3.14}$$

where the three formulations for the emplacement rate are $M = \hat{h}(1-T)\mathcal{I}_M$, $M = \hat{\lambda}_q q_p \mathcal{I}_M$,

Table 3.A.1: Reference scales and non-dimensional parameters

Quantity	Symbol	Definition	Preferred Value	Units
Tidal heating scale	ψ_0		4.2×10^{-6}	W/m^3
Liquid velocity scale	q_0	$q_0 = \psi_0 R/\rho L$	6.4×10^{-9}	m/s
Solid velocity scale	u_0	$u_0 = q_0$	6.4×10^{-9}	m/s
Porosity scale	ϕ_0	$q_0 = K_0\phi_0^n \Delta\rho g/\eta_l$	0.044	
Temperature scale	T_0	$T_0 = T_m - T_s$	1550	K
Bulk viscosity scale	ζ_0	$\zeta_0 = \eta/\phi_0$	2.3×10^{21}	Pas
Pressure scale	P_0	$P_0 = \zeta_0 q_0/R$	8.0×10^{6}	Pa
Péclet Number	Pe	$\mathrm{Pe} = q_0 R/\kappa$	1160	
Stefan Number	St	$\mathrm{St} = L/CT_0$	0.25	
Emplacement constant	$\hat{h}$	$\hat{h} = h\rho C T_0/\psi_0$	200	
Extraction constant	$\hat{\nu}$	$\hat{\nu} = \nu\zeta_0$	1000	
Scaled elastic limit temperature	$\hat{T}_e$	$\hat{T}_e = \frac{T_e - T_s}{T_m - T_s}$	0.6	
Compaction parameter	δ	$\delta = \zeta_0 K_0 \phi_0^n/\eta_l R^2$	5.8×10^{-3}	

The tidal heating scale ψ_0 is imposed, which gives the velocity scale q_0 which in turn gives the porosity scale ϕ_0.

and $M = \hat{\lambda}_c \mathcal{I}_M$. $\mathcal{I}_M$ is an indicator function that equals 1 for $T > T_e$ and $q_p > 0$, and equals zero otherwise. This ensures that emplacement only occurs above the elastic limit temperature, and provided there is melt present in the plumbing system to be emplaced. $E = \hat{\nu}(P - P_c)\mathcal{I}_E$ is the extraction rate, where the indicator function $\mathcal{I}_E$ equals 1 for $P > P_c$, and equals zero otherwise, ensuring that extraction only occurs in regions above the critical overpressure.

Total conservation of mass for the lithosphere–mantle and plumbing system are

$$\frac{1}{r^2}\frac{\partial}{\partial r}(r^2(u + q)) = M - E, \tag{3.15}$$

$$\frac{1}{r^2}\frac{\partial(r^2 q_p)}{\partial r} = E - M. \tag{3.16}$$

Darcy's law and the compaction relation become

$$q = \phi^n \left(1 - \phi_0\phi - \delta\frac{\partial P}{\partial r}\right), \tag{3.17a}$$

$$\phi P = \frac{1}{r^2}\frac{\partial(r^2 u)}{\partial r}, \tag{3.17b}$$

where δ is a dimensionless parameter defined in table 3.A.1. This measures the typical size of the compaction pressure gradients relative to the buoyancy; it is expected to be relatively small. It can be related to the compaction length (McKenzie, 1984) $l = \sqrt{\zeta_0 K_0 \phi_0^n/\eta_l}$, by $\delta = l^2/R^2$ (so the square root of δ is the ratio of the compaction length to the radius of the planet).

Conservation of energy becomes

$$\frac{\partial H}{\partial t}+\frac{1}{r^2}\frac{\partial}{\partial r}(r^2(u+q)T)+\frac{\mathrm{St}}{r^2}\frac{\partial}{\partial r}(r^2(\phi_0\phi u+q)) = \frac{1}{\mathrm{Pe}\, r^2}\frac{\partial}{\partial r}\left(r^2\frac{\partial T}{\partial r}\right)+\mathrm{St}\psi+M(1+\mathrm{St})-E(T+\mathrm{St}), \tag{3.18}$$

where Pe is the Peclet number, St is the Stefan number (table 3.A.1), and where bulk enthalpy has been scaled by $T_0\rho C$.

3.B Asymptotic approximation

To facilitate a rapid exploration of parameter space, I construct an approximation to the steady states of the model. This approximation makes use of the fact that the porosity scale ϕ_0 and the compaction parameter δ are both much less than unity. Neglecting them in the equations provides a good approximation over most of the lithosphere and the mantle, apart from in the boundary layer just below the boundary between the lithosphere and partially molten mantle (which is discussed in section 3.B.2). Importantly I note that Pe^{-1} is also expected to be a small parameter, but I retain conduction in the equations because it is important in controlling the temperature distribution within the lithosphere.

3.B.1 Lithosphere and mantle

I consider the lithosphere and the underlying mantle separately and solve for the position of the boundary $r = r_l$ between them. I assume that all extraction from the mantle occurs within the decompacting boundary layer, just below the base of the lithosphere (as is verified by the full numerical solutions). The extraction term E is therefore non-zero only in a narrow region of thickness $O(\delta)$ and hence is neglected from the continuum equations. At the base of the lithosphere $r = r_l$, the entire flux $q(r_l)$ (hereafter referred to as q_l) is transferred into the plumbing system. As $q_p = 0$ in the mantle, emplacement M only appears in the lithosphere equations. Taking this into account, the combination of mass continuity equations (3.13) and (3.14) indicate that $u = -q$ throughout the mantle. Since we also have $T = 1$ in the mantle, conservation of energy (equation (3.18)) becomes simply

$$\frac{1}{r^2}\frac{\partial(r^2 q)}{\partial r} = \psi, \tag{3.19}$$

so melting (or equivalently, the transport of latent heat by melt) balances tidal heating. Equation (3.19) can be integrated directly to give

$$q(r) = -u(r) = \frac{\psi}{3}\left(r - \frac{r_m^3}{r^2}\right). \tag{3.20}$$

Darcy's law (3.17) becomes $q = \phi^n$ so ϕ is deduced directly from q, and the compaction relation (3.17) further indicates that $P = -\psi/\phi$. In particular, these expressions give the values for the flux q_l, porosity, and compaction pressure at the top of the mantle $r = r_l$, which are used below to feed into the decompacting boundary layer,

$$q_l = \frac{\psi}{3}\left(r_l - \frac{r_m^3}{r_l^2}\right), \tag{3.21a}$$

$$\phi(r_l) = q_l^{1/n}, \tag{3.21b}$$

$$P(r_l) = \frac{\psi}{q_l^{1/n}}. \tag{3.21c}$$

The flux q_l transfers to the plumbing system at the top of the mantle for its continued transport through the lithosphere, to which I now turn.

In the lithosphere, $q = 0$ and the combination of mass equations (3.15) and (3.16) now requires $u = -q_p$, the plumbing-system flux. Conservation of mass in the plumbing system (3.16) becomes

$$\frac{1}{r^2}\frac{\partial(r^2 q_p)}{\partial r} = -M. \tag{3.22}$$

Conservation of energy in the lithosphere (4.18) becomes

$$\frac{1}{r^2}\frac{\partial}{\partial r}(r^2 uT) = \frac{1}{\mathrm{Pe}\, r^2}\frac{\partial}{\partial r}\left(r^2\frac{\partial T}{\partial r}\right) + \mathrm{St}\psi + M(\mathrm{St}+1), \tag{3.23}$$

so advection of the solid balances conduction, tidal heating, and heating from intrusions (emplacement). These two equations (3.22) – (3.23) are solved together to determine the temperature profile T, the plumbing system flux q_p (and hence the solid velocity u), and the position of the lithosphere-mantle boundary r_l. The required boundary conditions are

$$\begin{aligned} q_p = q_l, \quad T = 1, \quad \frac{\partial T}{\partial r} = 0, \quad \text{at } r = r_l, \\ T = 0, \quad \text{at } r = 1. \end{aligned} \tag{3.24}$$

Although this solution to the lithospheric system involves a numerical integration, it is considerably more straightforward and faster than the solution to the full model.

From this approach I find a good approximation to the thickness of the lithosphere, the temperature profile within the lithosphere, the plumbing flux q_p and emplacement rate (and hence the eruptive flux at the surface), as well as the porous melt flux and porosity in the majority of the mantle. A detail in the full solutions that is not yet captured by this asymptotic approximation is the high-porosity region — the decompacting boundary layer — just below the base of the lithosphere. In the context of my model, apart from transferring melt from the porous mantle to the plumbing system, the details of this layer are unimportant in determining the large scale structure of the solutions (thickness and temperature distribution of the lithosphere). However, in order to understand the dynamics further, I now analyse this region.

3.B.2 Decompacting boundary layer

The behaviour in the boundary layer is obtained by rescaling the equations locally to find a local approximation of the solution close to the lithosphere–mantle boundary. A composite approximation valid over the whole domain can then be found by combining the two approximations (the 'outer' mantle and lithosphere solution given above, and the 'inner' boundary layer solution).

As rising magma approaches the lithosphere–mantle boundary at $r = r_l$, it is no longer reasonable to neglect the compaction pressure gradient term in equation (3.17). Approaching the lithosphere, rising magma is impeded by the low permeability of downwelling solid, which causes magma to accumulate. The accumulation of magma in this layer generates pressure that decompacts the low-porosity-solid that is downwelling from the lithosphere (cf. Hewitt and Fowler, 2008). To understand what happens in this boundary layer, we must reintroduce the term proportional to δ in equation (3.17), and rescale lengths to consider the dynamics close to the lithosphere–mantle boundary.

First I note that including extraction, the conservation of mass equations for the solid, liquid, and plumbing system in the mantle are

$$\frac{1}{r^2}\frac{\partial}{\partial r}\left(r^2(1-\phi_0\phi)u\right) = -\psi, \tag{3.25a}$$

$$\frac{1}{r^2}\frac{\partial}{\partial r}\left(r^2(\phi_0\phi u + q)\right) = \psi - E, \tag{3.25b}$$

$$\frac{1}{r^2}\frac{\partial(r^2 q_p)}{\partial r} = E. \tag{3.25c}$$

I also note that the compaction pressure relation (3.17) can be combined with conservation of solid mass in the mantle (3.25a), giving

$$\phi_0 u\frac{\partial\phi}{\partial r} - (1-\phi_0\phi)\phi P = \psi. \tag{3.26}$$

I then write $r = r_l - \delta Z$, where Z is a boundary layer coordinate describing the rescaled distance beneath the lithosphere–mantle boundary. Rewriting equations (3.25a) – (3.25c), (3.17), and (3.26) in terms of this coordinate, we find

$$\frac{\partial u}{\partial Z} = O(\phi_0, \delta), \tag{3.27a}$$

$$\frac{\partial q}{\partial Z} = E + O(\phi_0, \delta), \tag{3.27b}$$

$$\frac{\partial q_p}{\partial Z} = -E + O(\phi_0, \delta), \tag{3.27c}$$

$$q = \phi^n \left(1 + \frac{\partial P}{\partial Z}\right) + O(\phi_0), \tag{3.27d}$$

$$-\mu u \frac{\partial \phi}{\partial Z} = \psi + \phi P + O(\phi_0, \delta), \tag{3.27e}$$

where $O(\phi_0, \delta)$ represents terms of order ϕ_0 or δ, which may be neglected (note that having rescaled into the boundary layer, the neglected terms are not the same as those neglected earlier, reflecting the different dominant physics in the boundary layer). I write $\phi_0/\delta = \mu$, and treat this as an $O(1)$ parameter.

The first mass conservation equation (3.27a) indicates that u is approximately constant throughout this layer, and its value is given by matching the value in the mantle below, $u = -q_l$, where q_l is the liquid flux defined in equation (3.21a). Moreover, adding together the second two mass conservation equations (3.27b) – (3.27c) shows that $q + q_p$ is constant, and must be equal to q_l to match with the mantle. The final two equations (3.27d) – (3.27e) (which represent Darcy's law and the compaction relation) can therefore be written as

$$q_l \mu \frac{\partial \phi}{\partial Z} = \psi + \phi P, \tag{3.28a}$$

$$\frac{\partial P}{\partial Z} = \frac{q}{\phi^n} - 1. \tag{3.28b}$$

Extraction occurs over the region $0 < Z < Z_E$ (Z_E is determined shortly). In this region we have $E = \hat{\nu}\delta(P - P_c)$, and I take the limit of very large extraction rate constant ν (so $\hat{\nu}\delta$ is large), such that $P \simeq P_c$ throughout this region. Equation (3.28a) can then be integrated to give

$$\phi(Z) = \frac{\psi}{P_c}\left(e^{\frac{P_c Z}{q_l \mu}} - 1\right), \qquad 0 < Z < Z_E, \tag{3.29}$$

and as P is approximately constant, equation (3.28b) gives $q = \phi^n$. The porosity and flux q therefore increase with Z through this extraction region and since $q_p = q_l - q$, the plumbing flux correspondingly decreases with Z until it reaches 0. This defines the position Z_E at which extraction started. Substituting $q_l = q = \phi^n$ into equation (3.29) gives

$$Z_E = \frac{q_l \mu}{P_c} \ln \left(\frac{P_c q_l^{1/n}}{\psi} + 1 \right). \tag{3.30}$$

Turning to the region below extraction where $E = 0$, mass conservation equations (3.25b) – (3.25c) indicate that $q_p = 0$ and $q = q_l$ are now approximately constant. In this region equations (3.28a) and (3.28b) comprise a two-dimensional phase-plane problem for $\phi(Z)$ and $P(Z)$. A solution is sought with $P = P_c$ and $\phi = q_l^{1/n}$ at Z_E (for continuity with the extraction region), and that matches the correct far-field behaviour as $Z \to \infty$. The correct behaviour is that ϕ and P tend towards the values $q_l^{1/n}$ and $-\psi/q_l^{1/n}$, given earlier in equation (3.21b) – (3.21c), to match with the rest of the mantle. Since this corresponds to a fixed point of the system that is a stable spiral or node, such a solution can be found. The solution involves decaying oscillations of both ϕ and P towards the far-field values, which are evident in figures 3.3 and 3.4, and even more so in figures 3.7 and 3.8.

It it worth pointing out that the $1/\phi$ dependence of bulk viscosity is an important control on the porosity oscillation within this boundary layer. Other forms of bulk viscosity with a weaker singularity have also been suggested; for example with $\zeta \sim -\ln \phi$ as $\phi \to 0$ (Rudge, 2018). The weaker dependence on porosity leads to greater oscillations, but the general form of the boundary layer is maintained.

To compare the asymptotic approximation with the full numerical solution, I construct a combination of the 'outer' solution for the majority of the mantle (where q is given by equation (3.20), $\phi = q^{1/n}$, and $P = \psi/\phi$), together with the 'inner' solutions for the decompacting boundary layer. Denoting the former solution as $\phi_m(r)$ and the latter solution $\phi_{bl}(Z)$, this composite solution is defined by

$$\phi(r) = \phi_m(r) + \phi_{bl}\left(\frac{r_l - r}{\delta}\right) - \phi_l, \tag{3.31}$$

with equivalent expressions for P and q, where the subtraction of the 'overlapping' value ϕ_l is necessary to avoid double counting.

3.C Analysis of heat flux and emplacement

Useful information can be obtained by integrating the energy equation (3.23) over the lithosphere (from $r = r_l$ to $r = 1$). Substituting equation (3.22) into equation (3.23), recalling that $u = -q_p$ and integrating, gives

$$\left((\mathrm{St}+1)q_p - \frac{1}{\mathrm{Pe}}\frac{\partial T}{\partial r} \right)\Bigg|_{r=1} = \mathrm{St} r_l^2 q_l + \mathrm{St}\int_{r_l}^{1} \psi \, r^2 \mathrm{d}r \tag{3.32}$$

where q_l is the melt flux at the top of the mantle, which was defined in equation (3.21a). Equation (3.32) can thus be written as

$$\left((\mathrm{St}+1)q_p - \frac{1}{\mathrm{Pe}}\frac{\partial T}{\partial r} \right)\Bigg|_{r=1} = \mathrm{St}\int_{r_m}^{1} r^2 \psi \mathrm{d}r. \tag{3.33}$$

where I recall that r_m is the radius of the core. The left hand side here represents the heat loss due to eruption and conduction at the surface, and the right hand side is the total tidal input; this expression thus represents a global energy balance.

After re-dimensionalising the variables, this can be written as

$$4\pi R^2 \left(q_p \left(\rho L + \rho C T_m - \rho C T_s\right) - k\frac{\partial T}{\partial r} \right)\Bigg|_{r=R} = \Psi, \tag{3.34}$$

where k is the conductivity.

As shown in figure 3.5, for the parameter regime applicable to Io, the surface conductive heat flux is negligible. In this case we see that the resurfacing rate q_s (that is, the value of q_p at the surface) is given by

$$q_s = \frac{\Psi}{4\pi R^2(\rho L + \rho C(T_m - T_s))}. \tag{3.35}$$

This expression can be contrasted with the liquid flux into the lithosphere q_l in equation

(3.21a). Since r_l is typically close to R, that expression can be written dimensionally as

$$q_l \approx \frac{\Psi}{4\pi R^2 \rho L}. \tag{3.36}$$

As such, q_s is approximately a fraction $L/[L + C(T_m - T_s)]$ of q_l, and the proportion of q_l that must be emplaced is

$$\frac{C(T_m - T_s)}{L + C(T_m - T_s)}. \tag{3.37}$$

For Io, equation (3.35) gives a resurfacing rate of of 1.25 cm/yr. Compared to the flux into the base of the lithosphere (equation (3.36)) of 6.3 cm/yr, equation (3.37) predicts that 80% of magma produced inside Io is emplaced into the lithosphere.

CHAPTER 4

Compositional evolution by magmatism and volcanism

The model, results, and analysis presented in this chapter have been published in Spencer et al. (2020b). This chapter constitutes a minor reformatting of that work to fit within the broader context of this thesis.

4.1 Introduction

In Chapter 3 I presented a model coupling magma formation and migration in Io's mantle to the volcanic systems in its lithosphere. Melting of an impure material invariably produces melts and residua with different compositions, and if the two phases separate, compositional evolution is expected. Despite Io's long history of study, it is not well known to what extent melting and volcanism control its interior structure and evolution and, in particular, if these processes create compositional layering within the mantle. The framework provided in Chapter 3 provides a new means of addressing these questions. Direct constraints on Io's interior structure would be provided by measurements of the composition and temperature of erupted lavas. To keep pace with recent improvements in observational techniques (e.g., Davies et al., 2016, 2017; de Kleer et al., 2019a,c), interior evolution models that are predictive of eruption temperatures and compositions are increasingly required.

Keszthelyi and McEwen (1997) presented an initial attempt to estimate the geochemical and petrological structure of Io's interior that would arise from the extensive volcanism. They predicted that the lithosphere would be dominated by felsic lavas rich in incompatible elements and that the mantle would be dominantly a forsterite-rich dunite. When the initial *Galileo* observations suggested widespread eruption of ultramafic lavas and constrained the temperature of the Pillan eruption to 1870 ± 25 K (McEwen et al., 1998), this model was abandoned. It was replaced by a model that called upon a region with $\sim$ 50% partial melting at the base of the lithosphere. This configuration hypothetically allowed efficient recycling of the erupted lavas back into the mantle (Keszthelyi et al., 1999, 2004). This magma-ocean model was supported by *Galileo* magnetometer results (Khurana et al., 2011) and is consistent with the suggestion of magnesian orthopyroxenes in Ionian lavas (Geissler et al., 1999). The magma-ocean model predicts a well-mixed and geochemically homogeneous mantle (Keszthelyi et al., 2004); erupted lavas would be largely uniform in temperature and composition, most likely similar to terrestrial komatiites (Williams et al., 2000).

However, there were significant challenges to the magma-ocean model as proposed in Keszthelyi et al. (2004). For example, once partial melting exceeds $\sim$ 20%, the shear modulus drops to the point that tidal dissipation cannot match the surface heat flow (Moore, 2003; Bierson and Nimmo, 2016; Renaud and Henning, 2018), limiting the possible thickness of such a high-melt-fraction layer (however, dissipation in a magma ocean may be significant e.g., Tyler et al., 2015; Hay et al., 2020). Furthermore, applying a different thermal model to the Pillan eruption, its temperature was revised down to $\sim$ 1600 K (Keszthelyi et al., 2007). Indeed, even the initial McEwen et al. (1998) results showed most eruptions being consistent with $\sim$ 1300 K (i.e., basaltic) temperatures. Spectroscopic constraints on the mineralogy of Io's lavas were always known to be weak because the *Galileo* camera did not observe far enough into the infrared to reliably detect other key minerals such as olivine (Geissler et al., 1999). These issues led to a revised magma-ocean model with the maximum degree of mantle partial melting only reaching $\sim 25\%$ and decreasing rapidly with depth (Keszthelyi et al., 2007). Auroral hotspot oscillations have been used as evidence against a magma ocean (Roth et al., 2017), and reanalysis of the magnetometer results suggests that plasma interactions with the atmosphere provide an alternative explanation to a magma ocean (Blöcker et al., 2018; de Kleer et al., 2019b). In Chapter 3 I showed that high melt fractions can arise within a decompacting boundary layer at the top of a low-melt-fraction mantle. Indeed, the distinction between a magma-ocean model and a low-melt-fraction model has significantly reduced since Keszthelyi and McEwen (1997) and McEwen et al. (1998); at this point, the hypothesis that Io is a largely solid body that has developed significant stratification needs to be investigated.

In this chapter I present a fluid dynamical model of lithosphere and mantle dynamics that builds on the framework presented in Chapter 3 by including compositional evolution. The compositional model is in the form of a two-component phase diagram between hypothetical refractory and fusible components. I use this simplified theory to investigate the effect of magmatic segregation and volcanic eruptions on leading-order chemical structure. My results show that magmatic segregation causes a rapid stratification of the mantle, with fusible material in the upper mantle and lithosphere, and refractory material at depth. Magma forms in both the upper and lower mantle and, importantly, magma must be able to leave the lower mantle in order to facilitate heat loss. The model exhibits two distinct modes of behaviour, depending on the fate of magma produced in the lower mantle. If lower mantle melts stall within the upper mantle, high temperature eruptions should not occur. However, if these refractory melts migrate to the surface, they can provide an explanation for the highest temperature eruptions observed on Io.

This chapter is organised as follows. First I outline the physics of the model before presenting results showing the two distinct modes of behaviour. I demonstrate the time evolution of both modes, and investigate the effect of bulk composition on the system. I then discuss these results in the context of present and potential future observations.

4.2 Model description

The model, shown schematically in figure 4.1, considers the evolution and dynamics of a tidally heated body composed of a mixture of two chemical components. It is an extension of the model described in Chapter 3 using the same equations, and also solved in one dimension. Here I extend it to consider conservation of chemical species and the effect of composition on melting behaviour, using a phase diagram described below. I consider the lithosphere and mantle to be a continuum that can either be entirely solid or partially molten, depending on the local energy content, and solve a system of conservation equations for mass, momentum, energy, and chemical species.

Alongside the continuum, I model a magmatic plumbing system that provides a means of upward magma transport distinct from magmatic segregation. Keszthelyi and McEwen (1997) proposed that deep, refractory magmas may sometimes ascend to the surface from great depth, but a mechanism to allow this has not been explored. I assume that anywhere magma reaches high overpressure, it enters into a magmatic plumbing system and migrates upward; this system can be present in both the lithosphere and the underlying mantle. The plumbing system presented in this chapter is thus a generalisation of that described in Chapter 3, with the potential to be present throughout the domain, as opposed to just in the lithosphere. The plumbing system could be interpreted as a system of fractures formed by buoyant, high pressure melt. However, in the formulation of my model I am purposefully agnostic to its exact physical form; I consider possible interpretations in section 4.4. When magma enters the plumbing system, it transports the local melt composition and temperature upward into the upper mantle and lithosphere. The flux of plumbing-system melt that reaches the surface is the erupted flux; its composition sets the composition of the newly resurfaced lithosphere. As in Chapter 3, the lithosphere is defined as the portion of the domain that is below the solidus (where the porosity is zero), and so the thickness of the lithosphere is the distance over which cold, surface material downwells before it is heated sufficiently to begin re-melting.

I revisit the thermochemical melting models that have been used to predict the segregation of Io's mantle into an upper fusible layer and a deep layer of almost-pure olivine (Keszthelyi and McEwen, 1997). My approach is to simplify the compositional model to two representative end-members, aiding their incorporation into a dynamical framework. I consider Io to be composed of a mixture of these two components, with a melting behaviour that is described by the two-component phase diagram shown in figure 4.2. The presence of fusible material (component A) significantly reduces the melting point of the refractory component (component B), and so upon heating, fusible melts are produced until component A is almost entirely removed from the system. These types of compositional model have proven fruitful in studies of mantle melting at mid-ocean ridges (Katz, 2010; Katz and Weatherley, 2012).

As in Chapter 3, I assume spherical symmetry motivated by the global distribution of Io's volcanoes (Kirchoff et al., 2011; Williams et al., 2011). The one-dimensional approach of this work precludes my ability to investigate processes such as thermochemical convection that may be a consequence of stratification, a point I discuss in section 4.4.5, below. I focus my analysis on the chemical evolution of the system, and therefore take tidal dissipation to be uniform, avoiding dependence on poorly constrained rheological parameters (Bierson and Nimmo, 2016; Renaud and Henning, 2018). In actuality, the tidal heating rate depends on radius, latitude, and longitude, and so while I would not expect significant changes in radial structure to arise from its inclusion, it is likely to be an important component of models that aim to predict surface variability (see Chapter 5). I neglect the pressure-dependence of the

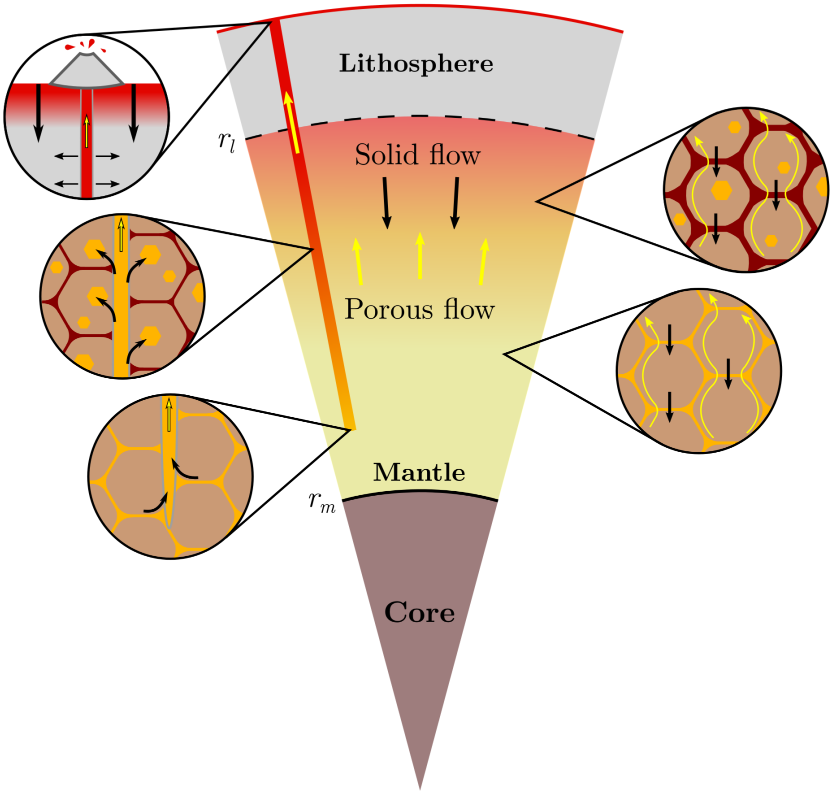

Figure 4.1: Schematic of the model. Magma rises buoyantly in the mantle while the solid moves downwards. If a critical overpressure is exceeded, magma is extracted to a magmatic plumbing system. It freezes (is emplaced) from the plumbing system back into the continuum at a rate defined in equation (4.10). Some magma reaches the surface, fueling volcanic eruptions and burying the lithosphere. The composition of erupted magma determines the composition of the lithosphere. The core is excluded from the model.

melting temperature due to the small size of Io and hence the low pressures in the mantle. I also neglect solid-state phase change and any compositional dependence of latent heat or phase density. For more detailed petrological modelling, it may be important to include these effects.

My model considers the time-dependent evolution of the interior structure and composition, and explores the evolution to a steady state. I develop a reduced model to elucidate key features of the dynamics predicted by the full model. The reduced model is formulated at steady state and its structure is motivated by solutions obtained to the full model; it is detailed in Appendix 4.C.

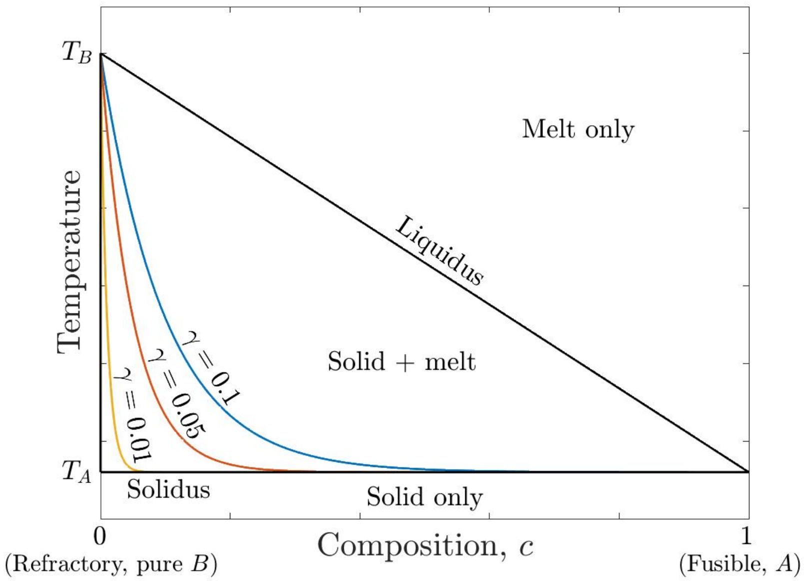

Figure 4.2: The phase diagram employed in the model. The black lines show the solidus and liquidus between a refractory component B and a fusible component A. Coloured lines show the smoothed solidus using equation (4.1) for different values of γ, which allow the presence of a small amount of fusible material in solid solution with component B. As $\gamma \to 0$, the smoothed solidus approaches the solidus of pure solid B. The full model uses a smoothed solidus with $\gamma = 0.01$, and the reduced model uses the $\gamma = 0$ solidus.

4.2.1 Model equations

I consider a generic refractory component B and a fusible component A, and the phase diagram shown in figure 4.2. The concentration of the fusible component A in phase i (solid s or liquid l) is denoted c_i, and that of the refractory component is $1 - c_i$. The solidus temperature T_s is given by

$$T_s = T_B + (T_A - T_B)\frac{1 - e^{-c_s/\gamma}}{1 - e^{-1/\gamma}}, \tag{4.1}$$

and the liquidus temperature T_l is given by

$$T_l = T_B - (T_B - T_A)c_l, \tag{4.2}$$

where T_B is the melting point of the refractory component, T_A is the melting point of the fusible component, and $\gamma > 0$ is a parameter that controls the amount of fusible material that is incorporated in a solid solution with component B. I allow this small degree of solid solution simply because it provides a smoothed solidus curve, which facilitates my numerical method (the effect of smoothing the solidus is small, and is discussed in section 4.C). As $\gamma \to 0$, the smoothed solidus approaches that of pure refractory component B. It is important to note that the chosen form for the solidus is arbitrary and does not have a thermodynamic basis.

The model presented in Chapter 3 is described by conservation equations for mass, momentum, and energy in a compacting two-phase medium and conservation of mass and energy equations in the magmatic plumbing system. These are

$$\boldsymbol{\nabla}\cdot(\boldsymbol{u}+\boldsymbol{q}) = -E + M, \tag{4.3}$$

$$\boldsymbol{q} = -\frac{K_0\phi^n}{\eta_l}\left[(1-\phi)\Delta\rho\boldsymbol{g} + \boldsymbol{\nabla} P\right], \tag{4.4a}$$

$$P = \zeta\left(\boldsymbol{\nabla}\cdot\boldsymbol{u} - M\right), \tag{4.4b}$$

$$\frac{1}{\rho C}\frac{\partial H}{\partial t} + \boldsymbol{\nabla}\cdot[(\boldsymbol{u}+\boldsymbol{q})T] + \boldsymbol{\nabla}\cdot\left[(\phi\boldsymbol{u}+\boldsymbol{q})\frac{L}{C}\right] = \boldsymbol{\nabla}\cdot(\kappa\boldsymbol{\nabla} T) + \frac{\psi}{\rho C} - E\left(T+\frac{L}{C}\right) + M\left(T_p+\frac{L}{C}\right), \tag{4.5}$$

$$\boldsymbol{\nabla}\cdot\boldsymbol{q}_p = E - M, \tag{4.6}$$

$$\boldsymbol{\nabla}\cdot(\boldsymbol{q}_p T_p) = ET - MT_p, \tag{4.7}$$

where $\boldsymbol{u}$ is the solid velocity, $\boldsymbol{q} = \phi(\boldsymbol{v}-\boldsymbol{u})$ is the Darcy segregation flux, E is the extraction rate to the plumbing system, and M is the emplacement rate from the plumbing system. Porosity is denoted by ϕ, and $K_0\phi^n$ is the permeability, in which n is the permeability exponent. In addition, $\Delta\rho$ is the density difference between solid and liquid, $\boldsymbol{g} = -g\hat{\boldsymbol{r}}$ is the gravity vector, η_l is the liquid viscosity, $P = (1-\phi)(P_l - P_s)$ is the compaction pressure, and $\zeta = \eta/\phi$ is the compaction viscosity, related to shear viscosity η. Bulk enthalpy is defined as $H = \rho CT + \rho L\phi$, T is temperature, L is the latent heat, C is the specific heat capacity, ρ is the density, ψ is the volumetric tidal heating rate, κ is the thermal diffusivity, T_p is temperature in the plumbing system, and $\boldsymbol{q}_p$ is the plumbing system flux.

Conservation of mass (4.3) tells us that material leaves the lithosphere–mantle system by extraction to the plumbing system and enters the lithosphere–mantle system by emplacement from the plumbing system back into the continuum. Conservation of momentum is formulated by the combination of Darcy's law (4.4a), which tells us that fluid flow is driven by buoyancy and compaction pressure gradients, with the compaction relation (4.4b), which relates the liquid overpressure to the compaction rate $\boldsymbol{\nabla}\cdot\boldsymbol{u}$ (McKenzie, 1984). Equation (4.4b) includes magmatic emplacement because I assume that emplacement does not cause fluid pressurisation. Conservation of energy (4.5) tells us that changes in bulk enthalpy occur by the advection of sensible and latent heat, diffusion of sensible heat, tidal heating, the energy removed by extraction, and the energy delivered by emplacement. Conservation of mass (4.6) in the plumbing system tells us that the plumbing system flux increases when material is extracted from the mantle and decreases when material is emplaced back into the continuum. Equation (4.7) represents conservation of energy in the plumbing system. There are no time derivatives in equations (4.6) – (4.7) because the plumbing system is assumed to occupy negligible volume (see section 2.4).

To the equations above, I add an equation that tracks the composition of the system

$$\frac{\partial \overline{c}}{\partial t} + \boldsymbol{\nabla}\cdot[(\phi\boldsymbol{u} + \boldsymbol{q})c_l] + \boldsymbol{\nabla}\cdot[(1-\phi)\boldsymbol{u}c_s] = -Ec_l + Mc_p, \tag{4.8}$$

where $\overline{c} = \phi c_l + (1-\phi)c_s$ is the phase averaged composition and c_p is the composition of material in the plumbing system. This equation tells us that changes in phase averaged composition occur through advection of the liquid composition, advection of the solid composition, extraction of the liquid to the plumbing system, and emplacement of the plumbing system material. I neglect compositional diffusion due to the large advective velocities compared to chemical diffusivity. The composition of plumbing system material is given by a conservation of chemical mass equation

$$\boldsymbol{\nabla}\cdot(\boldsymbol{q}_p c_p) = E c_l - M c_p, \tag{4.9}$$

where the plumbing system composition can only change by the addition of melts from the lithosphere–mantle system of a different composition.

In Chapter 3 I proposed three feasible parametrisations for the rate of magmatic emplacement M. I showed that these three different formulations all produce broadly similar effects, especially considering the uncertainties in the parameters involved in each. Here I explore only a temperature-dependent formulation because, as shown in Chapter 3, this formulation has the smoothest temperature derivatives at places where emplacement initiates, which facilitates better numerical convergence. The magmatic empalcement rate is taken to be

$$M = \begin{cases} \frac{h_M C(T_p - T)}{L} & T \geq T_A, \\ \frac{h_L C(T_p - T)}{L} & T_A > T \geq T_e, \\ 0 & T < T_e, \end{cases} \tag{4.10}$$

where T_e is an elastic limit temperature below which no emplacement occurs (see Chapter 3). The emplacement rate constant h was discussed at length in Chapter 3, but here I propose that it may have different values in the mantle h_M and the lithosphere h_L (the lithosphere is where $T < T_A$). The mechanisms by which magma propagates through a partially-molten medium are likely to be very different to those in a solid, and so would be expected to have a different efficiency of magma transport. In this work, h_L is directly analogous to h in Chapter 3 and the behaviour with different values of h_M will be explored.

Extraction of liquid from the mantle into the plumbing system is treated in the same way as in Chapter 3; the transfer is taken to be a function of liquid overpressure,

$$E = \begin{cases} \nu(P - P_c) & P \geq P_c, \\ 0 & P < P_c, \end{cases} \tag{4.11}$$

where ν is an extraction rate constant (units $\mathrm{s}^{-1}\mathrm{Pa}^{-1}$), and P_c is a critical overpressure that the liquid must exceed in order to be extracted into the plumbing system. I recall that P is the overpressure relative to the solid pressure P_s, not the absolute liquid pressure P_l. I take P_c to be a constant, but a more realistic model might relate this parameter to depth and the local system state, to capture the different pressures required to initiate and sustain dikes.

The full model to be solved comprises equations (4.3) – (4.11), which govern the time evolution of temperature, porosity, and composition, as well as the magma and solid velocities. The phase averaged composition $\overline{c}$ and the bulk enthalpy H uniquely define the temperature, porosity, and liquid and solid compositions through the solidus and liquidus equations (4.1) – (4.2), the definition of bulk enthalpy, and the definition of phase averaged composition.

The required boundary conditions for the system are

$$\begin{aligned} \boldsymbol{q} = \boldsymbol{q}_p = 0, \quad \frac{\partial H}{\partial r} = \frac{\partial \overline{c}}{\partial r} = 0, \quad c_p = c_l, \quad T_p = T, \quad \frac{\partial P}{\partial r} = -(1-\phi)\Delta\rho \boldsymbol{g} \quad \text{at } r = r_m, \\ H = T_s, \quad \boldsymbol{u} = -\boldsymbol{q}_p, \quad \overline{c} = c_p \quad \text{at } r = R. \end{aligned} \tag{4.12}$$

As in Chapter 3, at the base of the domain there is no solid or liquid flow, as well as no flux in the volcanic plumbing system. I again assume no gradient in enthalpy at the base of the domain, which in turn leads to the condition on compaction pressure, which ensures that the Darcy flux is zero at the base of the domain even if porosity is not (see the text after equation (3.11)). To this I add conditions on the bulk composition, and on the composition and temperature of the plumbing system. I assume no gradient in the bulk composition at the base of the domain, and I set the composition and temperature of the plumbing system equal to the surrounding liquid composition and temperature respectively. The surface boundary conditions are the same as in Chapter 3 except for the addition of a condition on composition. This condition states that the composition at the surface is set by the erupted composition, which together with the zero basal fluxes, conserves the bulk composition. Initial conditions are required for enthalpy and composition. I take a body of uniform composition (the value of which sets the bulk composition), uniformly on its solidus. Other initial conditions, for example starting uniformly cold, do not affect the broad behaviour of the system after an initial transient phase (see section 4.3.2).

Parameter values and definitions are given in table 4.1. The system is scaled (see Appendix 4.A) and spherical symmetry is assumed so that all variables are a function of only radial position r and time. The system is solved using the Portable, Extensible Toolkit for Scientific computation (PETSc) (Balay et al., 1997, 2019, 2020; Katz et al., 2007). Details of the implementation are given in Appendix 4.B. The code is benchmarked against the single component model presented in Chapter 3.

4.3 Results

The steady-state behaviour of the model across parameter space can be broadly divided into two distinct modes. This division is on the basis of the transport of refractory melts that form in the lower mantle, which is controlled by the value of the mantle emplacement constant h_M. The results in this section are framed to exhibit the contrasting behaviour of these two modes; the implications of each mode will be discussed further below. In mode 1, rising refractory magma in the magmatic plumbing system interacts and exchanges substantial energy with the lower-temperature partially-molten upper mantle. This drives

Table 4.1: Dimensional parameters

Quantity	Symbol	Preferred Value	Units
Radial position	r		m
Radius	R	1820	km
Core radius[1]	r_m	700	km
Lithosphere radius	r_l		m
Boundary layer coordinate	Z		m
Solid velocity	u		m/s
Segregation flux	q		m/s
Volcanic plumbing flux	q_p		m/s
Porosity	ϕ		
Permeability constant[2]	$K = K_0\phi^n$	10^{-7}	m^2
Permeability exponent[2]	n	3	
Density	ρ	3000	$\mathrm{kg/m^3}$
Density difference	$\Delta\rho$	500	$\mathrm{kg/m^3}$
Gravitational acceleration	g	1.5	$\mathrm{m/s^2}$
Shear viscosity	η	1×10^{20}	Pa s
Liquid viscosity	η_l	1	Pa s
Volume transfer rate	Γ		s^{-1}
Emplacement rate	M		s^{-1}
Lithospheric emplacement constant*	h_L	5.7	Myr^{-1}
Mantle emplacement constant	h_M		Myr^{-1}
Extraction rate	E		s^{-1}
Extraction constant	ν	1.4×10^{-5}	$\mathrm{Myr}^{-1}\mathrm{Pa}^{-1}$
Compaction pressure	P		MPa
Critical overpressure	P_c	0	MPa
Compaction viscosity	ζ		Pa s
Bulk enthalpy	H		$\mathrm{J/m^{-3}}$
Temperature	T		K
Plumbing system temperature	T_p		K
Solidus temperature	T_s		K
Liquidus temperature	T_l		K
Solidus constant	γ	0.01	
Elastic limit temperature	T_e	1000	K
Refractory melting temperature	T_B	1500	K
Fusible melting temperature	T_A	1230	K
Surface temperature	T_{surf}	150	K
Thermal diffusivity	κ	10^{-6}	$\mathrm{m^2/s}$
Latent heat	L	4×10^5	J/kg
Specific heat capacity	C	1200	J/kg/K
Phase-averaged composition	$\bar{c}$		
Solid composition	c_s		
Liquid composition	c_l		
Plumbing system composition	c_p		
Tidal heating rate**	ψ	4.2×10^{-6}	$\mathrm{W/m^{-3}}$

* *h* in Chapter 3

** Such that the integrated heating matches the observed input[3] of $\sim 1 \times 10^{14}$ W

[1]Bierson and Nimmo (2016), [2]Katz (2008), [3]Lainey et al. (2009)

all plumbing-system magmas to freeze within the upper mantle and, as a result, refractory melts to not reach the lithosphere. In mode 2, refractory plumbing-system magmas rise through the upper mantle with little to no interaction. These melts reach the base of the lithosphere, combine with more fusible melts, and are erupted to the surface. Figures 4.1 and 4.2 show steady-state solutions for the full model for each of the two modes. Figure 4.3 shows the evolution of the model from an initial uniform state, again for each of the two modes. Finally, in figure 4.4 I summarise the behaviour of the model as a function of the bulk composition of the body, demonstrating the transition between the two modes. These figures are discussed further below.

In this chapter I do not explore the parameter space of the lithospheric emplacement constant h_L, the elastic limit temperature T_e, nor the critical extraction pressure P_c. The effect of variation in these parameters was considered in Chapter 3 and their effects here are the same. The lithospheric emplacement constant h_L and the elastic limit temperature T_e control the thickness and temperature distribution in the lithosphere, and the critical extraction pressure P_c affects the melt fraction in decompacting boundary layers that occur where magma is extracted to the plumbing system. In the results presented here, I choose values of h_L and T_e that give reasonable lithospheric thicknesses and temperature distributions. I take $P_c = 0$ and explore whether compositional effects also exert a control on melt fractions.

4.3.1 Two modes of magmatism

Figure 4.1 shows temperature, porosity, fluxes, and compositions at steady state for two representative values of h_M. Refractory magmas that form in the lower mantle are transferred to the magmatic plumbing system at the top of the lower mantle, enabling their continued rise. As they rise through the upper mantle, they are emplaced at a rate proportional to h_M, and it is the size of this parameter that distinguishes the two modes. Mode 1 arises when h_M is sufficiently large that all the melt from the lower mantle is emplaced into the midand upper mantle. Mode 2 arises when some of the melt extracted from the lower mantle reaches the lithosphere, which occurs if h_M is sufficiently small. Solid lines in figure 4.1 are steady-state solutions to the full model; dashed lines are solutions to the reduced model.

The two modes share various features that can be identified from figure 4.1. I discuss these similarities before considering their differences. Some features are similar to those in the one-component case of Chapter 3, which I cover only briefly here. The radial porosity profiles in figure 4.1b,f show that the uniform tidal heating causes melt to form throughout the mantle. Figure 4.1c,g shows that these melts rise buoyantly while the solid correspondingly sinks. Where melt reaches high pressure it is extracted into the plumbing system, through which it continues to rise. The lithospheric plumbing system carries melt to the surface where it erupts. The globally-averaged eruption rate is the surface plumbing-system flux in figure 4.1c,g. Over long timescales and given the negligible surface conduction, this global eruption rate must extract heat at the same rate that it is input to the interior by tidal heating. The upward flux of melt through the lithospheric magmatic plumbing system is balanced by downwelling of the solid lithosphere. This recycles erupted material back into the mantle.

At steady state in both modes, the mantle has segregated into three layers: a refractory lower mantle with $T = T_B$, a low-melt-fraction mid-mantle with $T_A < T < T_B$, and a fusible upper mantle with $T \approx T_A$. As lithospheric solid downwells through the upper mantle, tidal heating causes the formation of fusible melts, which buffers the temperature close to T_A. With continued melting and the buoyant segregation of fusible melts, material downwelling out of the upper mantle is almost exhausted in fusible material and so its solidus temperature has increased according to the phase diagram. In this mid-mantle region, tidal heating primarily acts to raise the temperature of the solid. As a result, melting rate and porosity are low in the mid-mantle, as seen in both modes in figure 4.1b,f. Further, the Darcy flux in the mid-mantle is approximately zero (figure 4.1c,g), so heat transport across

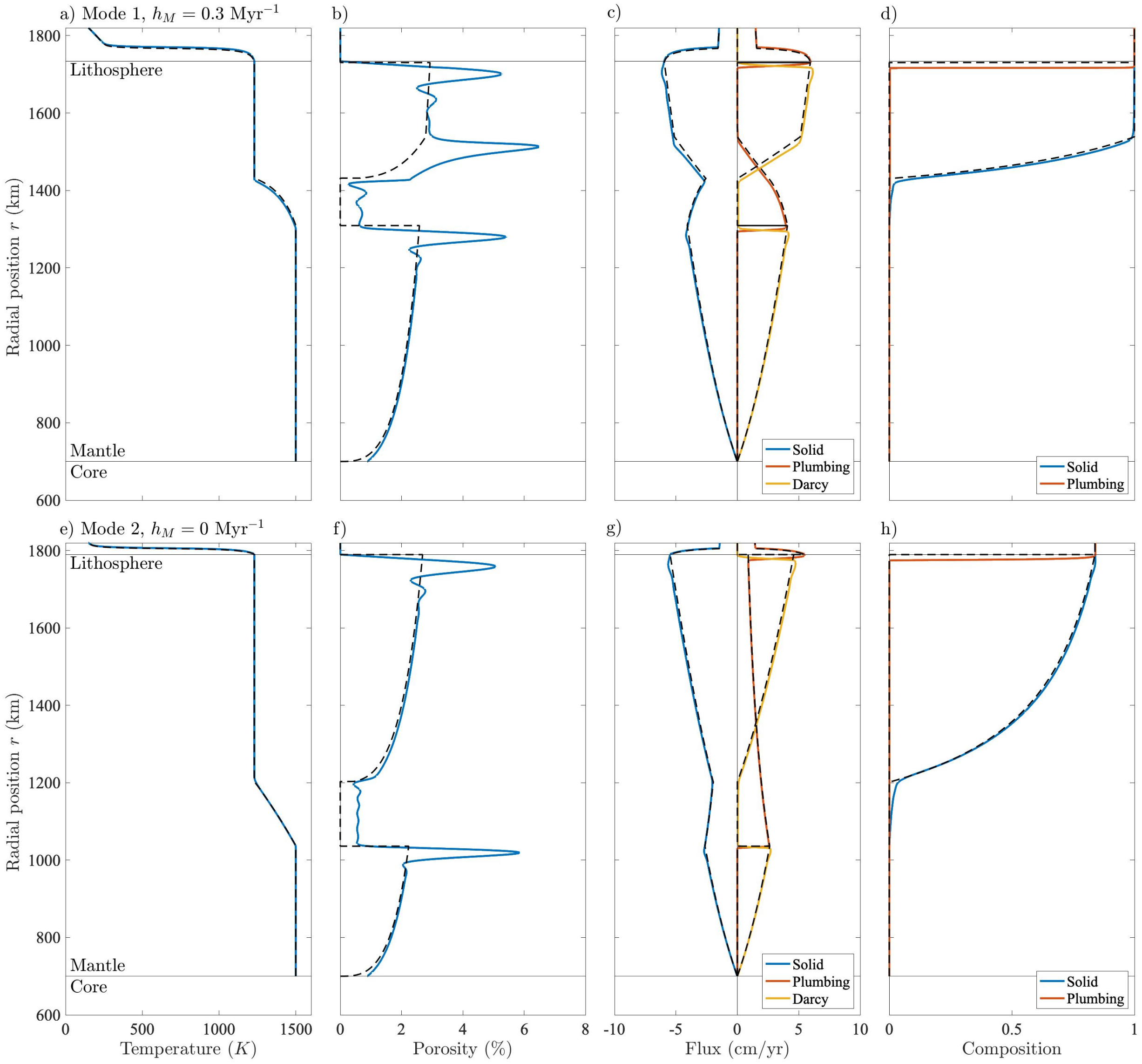

Figure 4.1: Steady-state solutions to the full model for two end-member behaviours showing temperature; porosity; solid, plumbing, and Darcy fluxes; solid and plumbing system compositions. Panels a–d show mode 1 where $h_M = 0.3$ Myr^{-1}; deep refractory plumbing material is emplaced into the upper mantle. Panels e–h show mode 2 where $h_M = 0$; deep refractory material is not emplaced in the mantle. Bulk composition is 0.5. In both modes the lower mantle is segregated to a purely refractory composition at temperature T_B, but in mode 2 the ability of refractory material to migrate to the lithosphere means that the upper mantle is a mixture of refractory and fusible components. In mode 1 the emplacement of refractory melts into the upper mantle drives increased melting, resulting in a porosity peak in the lower part of the upper mantle. The dashed lines show solutions to the reduced model. Parameter values are given in table 4.1.

this region occurs only by conduction, advection in the plumbing system, and downward solid advection, a result that I discuss below. Continued heating as the solid downwells

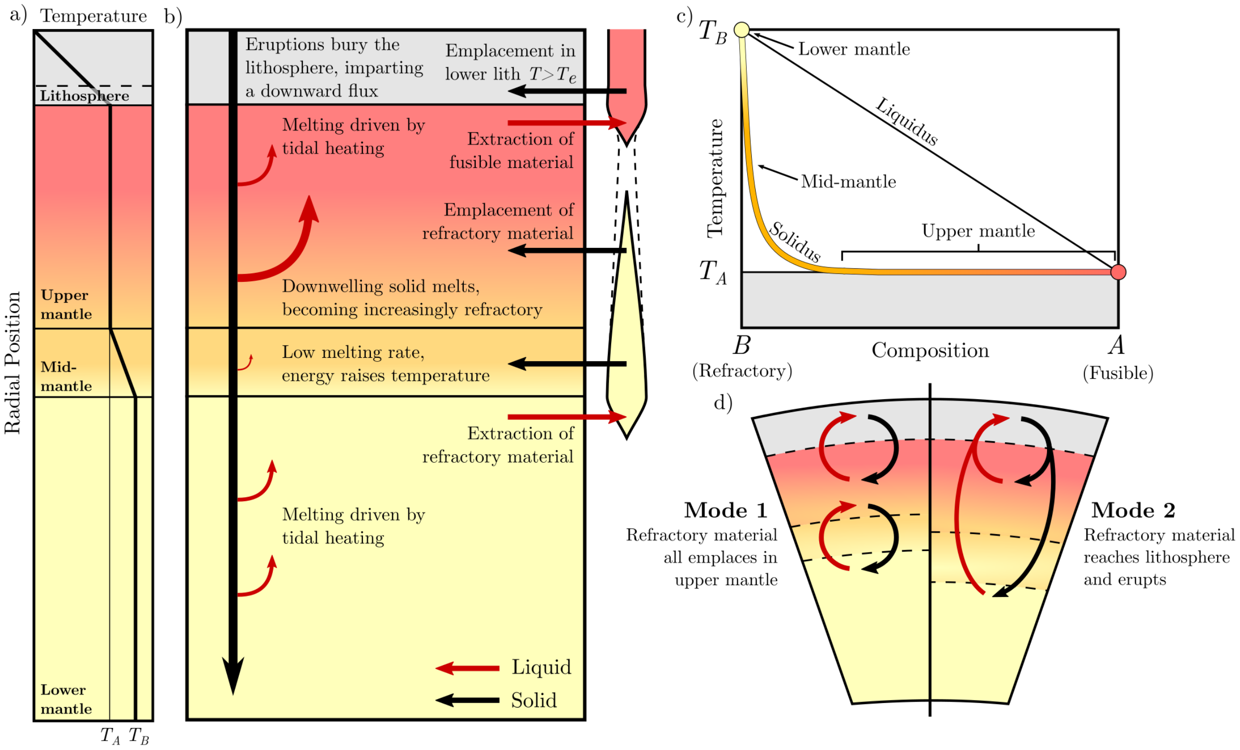

Figure 4.2: Schematic describing the steady-state solutions. Colour indicates composition (panel c). a) The upper and lower mantle are at the melting point of the fusible and refractory components respectively. b) Melting in the lower mantle is driven by tidal heating. Melting rate in the mid-mantle is low because energy goes toward raising the temperature of downwelling material. If emplacement of refractory melts in the upper mantle occurs, this drives large amount of melting and exhausts the plumbing system material. Fusible melt is extracted from the top of the upper mantle and combines with any plumbing-system material, some of which is emplaced in the lower lithosphere; the remainder rises to fuel volcanic eruptions. d) In mode 1, all refractory material is emplaced in the upper mantle. In mode 2, refractory material rises to the lithosphere and so cycles through the surface.

through the mid-mantle melts out the remaining small amount of fusible material, and the solid is raised to the refractory melting point T_B. Melting rate and thus porosity increase in the lower mantle because, as in the upper mantle, all imparted tidal heating directly causes melting.

Magma rising through a two-phase medium cannot pass into impermeable regions. Such regions act as barriers to flow, causing an increase in magma pressure, which forces the solid to decompact and produces higher melt fractions (figure 4.1b,f). The lithosphere represents such an impermeable barrier to melts rising through the upper mantle, and similarly, the mid-mantle region acts as an essentially impermeable barrier to melts rising from the lower mantle. The high liquid pressure below these layers causes melts to be extracted into the magmatic plumbing system. Magma extracted from the lower mantle is composed entirely of the refractory component and is at temperature T_B. Flow through the plumbing system enables these refractory melts to migrate from the lower mantle into the colder overlying mantle and lithosphere. The differences between the two modes are then a consequence of what happens to this melt. The mid- and upper mantle are below the melting point of the refractory component, and it may be expected that these lower temperatures causes refractory plumbing system material to be emplaced during ascent.

In mode 1 (figure 4.1a–d), this emplacement is significant — it acts to exhaust the plumbing system of refractory material before it reaches the lithosphere. As refractory melts are emplaced they release their latent heat to the upper mantle, providing additional heat to melt surrounding fusible material. This is reflected in the rapid increase of Darcy flux in the lower part of the upper mantle in figure 4.1c. The emplacement of refractory melts into the upper mantle eventually exhausts the material in the plumbing system, as shown by the plumbing system flux in 4.1c. Where the plumbing system material runs out, the melting rate in the upper mantle decreases to just that produced by tidal heating, which causes the change in gradient of the Darcy flux in the upper mantle in figure 4.1c. The change in melting rate caused by the cessation of emplacement means that downwelling solid must suddenly decompact, creating a high-porosity decompacting layer in the upper mantle, which can be seen in figure 4.1b.

Mode 2 (figure 4.1e–h) is the case where at least some of the melt that is extracted from the lower mantle makes it all the way to the surface. The end-member shown in figure 4.1 is when $h_M = 0$, in which case there is no emplacement in the upper mantle at all. The plumbing-system flux still decreases in figure 4.1g, but only due to radial spreading in a spherical coordinate system, and so the total volume of melt extracted from the lower mantle reaches the top of the upper mantle. Fusible magmas extracted at the top of the upper mantle combine with refractory plumbing system melts rising from below, producing lithospheric plumbing-system material with a volumetrically averaged temperature and composition. This lithospheric plumbing-system material describes either an average of non-interacting melts of different temperatures and compositions, or a mixture with an intermediate composition; I assume that the effect is the same on the long timescales considered here. The lithospheric plumbing system melts are emplaced into the lithosphere at a rate determined by h_L and the temperature of the melt, and with a distribution determined by T_e. Material that erupts onto the surface in mode 2 is at a higher temperature than in mode 1, and so serves as a more efficient heat-loss mechanism. This increased heat-loss efficiency results in a lower eruption rate and a thinner lithosphere (see below).

Figure 4.2 shows a schematic of temperature, mass transport, and the phase diagram. Colours in figure 4.2 denote composition according to the phase diagram in panel c. Mode 1 is characterised by a strong segregation of fusible and refractory material; refractory material does not erupt, instead it is cycled between the lower mantle and the deep parts of the upper mantle, whilst fusible material is cycled between the upper mantle and the lithosphere. In mode 2, refractory material is cycled from the lower mantle to the surface, and fusible material is cycled from the upper mantle to the surface. In both modes, the lower mantle is composed purely of refractory material, and the mid-mantle spans compositions corresponding to the steep section of the solidus in figure 4.2c. In mode 1 there is a transition from almost pure refractory to pure fusible material above the region of the upper mantle where emplacement takes place (figure 4.1d). In mode 2, the segregation of the mantle is much less complete, as shown by figure 4.1h. The lack of mantle emplacement means that refractory melts rise all the way to the surface. The intermediate-composition erupted material is buried down through the lithosphere and upper mantle, and its composition gradually changes due to the melting of the fusible material by tidal heating.

4.3.2 Time-evolution to steady state

Figure 4.3 shows how both modes of the model evolve to steady state, presenting results for eruption rate, temperature, porosity, and composition. I assume an initially homogeneous body with a bulk composition of 50% fusible material that is initially on its solidus throughout. Other initial conditions, for example starting uniformly cold, or with a cold lithosphere, result in the same broad behaviour, but starting on the solidus removes the spin-up time required to heat the mantle. Thus, despite not knowing the precise 'initial condition', various distinctive behaviours can be found that may have important implications for the evolution of Io and other volcanic bodies. The left column of figure 4.3 shows the evolution of mode 1, and the right column shows the evolution of mode 2. Note that steady state is reached much more rapidly in mode 1 and so the time axis of mode 2 is significantly expanded. The final steady states are those shown previously in figure 4.1.

The early ($t \leq 5$ Myr) evolution of the model is the same for both modes. Fusible (pure-A) melts are produced throughout the mantle and rise upward. They are erupted onto the surface and so a cold fusible lithosphere begins to grow. The upper mantle is being continually resupplied with fusible material as it is buried through the lithosphere and remelted at its base. There is no such resupply of fusible material to the deep mantle, which becomes increasingly refractory. After $\sim$ 5 Myr, about 20% of Io's volume has been erupted and reburied; the lower mantle is almost completely depleted in fusible material. As a result, melting rate there drops and the solid starts to climb the solidus toward $T = T_B$ (figure 4.2). Panels a and d in figure 4.3 show that the decreased melting rate in the lower mantle reduces the eruption rate to almost zero. This reduction in eruption rate causes the lithosphere to thin, increasing conductive heat loss from the surface. Once the lower mantle has been heated to T_B, the 3-layer mantle structure described above in the steady-state solution emerges. From this point in the evolution onward, the mid-mantle is acting as an impermeable barrier to refractory melts formed in the lower mantle. The presence of this barrier

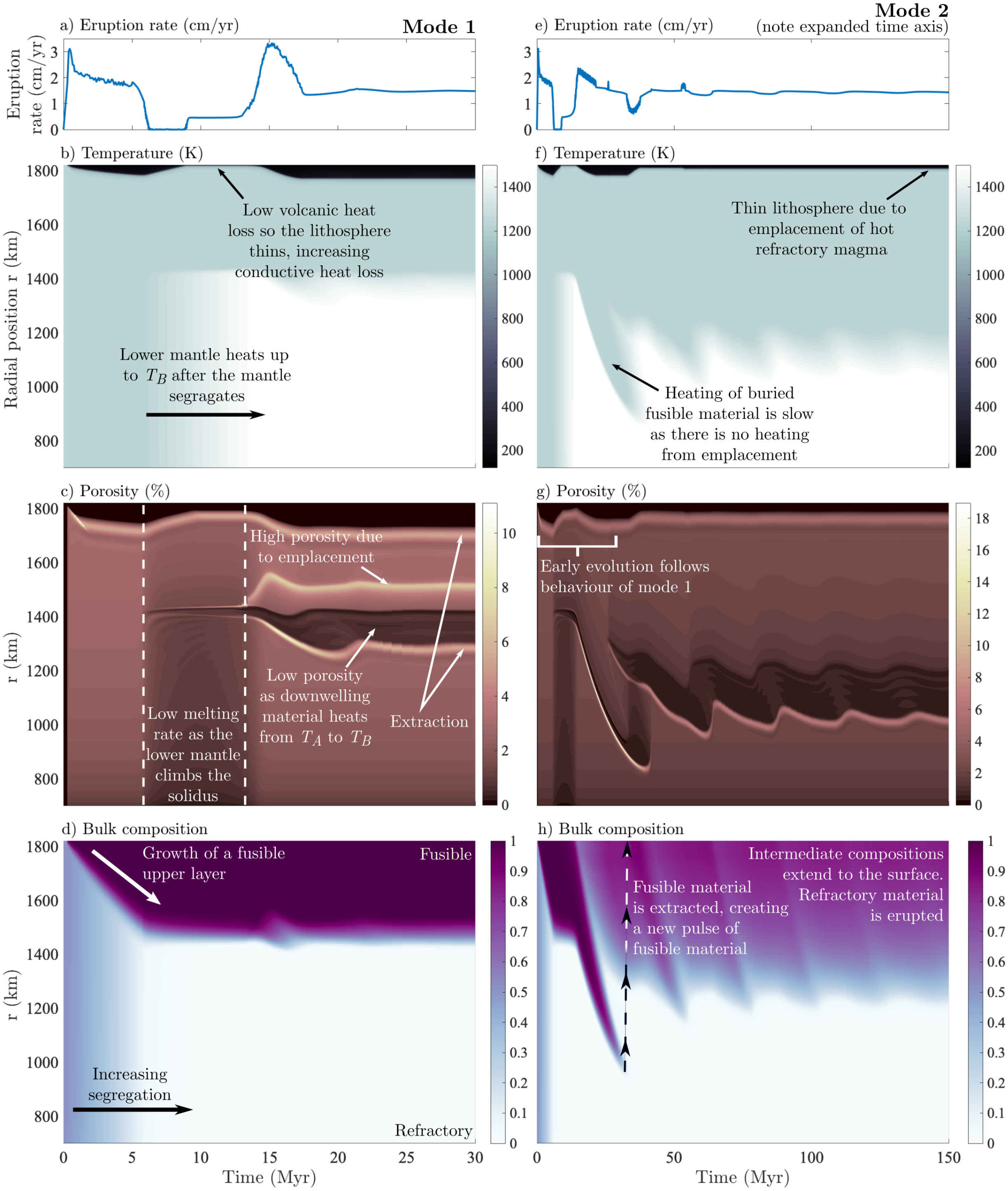

Figure 4.3: The evolution of the full model to steady state, showing eruption rate, temperature, porosity, and phase-averaged (bulk) composition. Panels a–d show mode 1 of the model where $h_M = 0.3$ Myr^{-1}, and panels e–h show mode 2 where $h_M = 0$. In both cases, the initial condition is an unstratified mantle of composition $\bar{c} = 0.5$, uniformly on the solidus. In mode 1, the emplacement of deep melts into the upper mantle rapidly drives the system to segregate, and equilibrium is reached in ∼30 Myr. No refractory material reaches the surface. Mode 2 takes much longer to reach steady state. In mode 2, refractory melt reaches the surface and intermediate compositions exist throughout the upper mantle.

causes melt to accumulate at the top of the lower mantle, as shown by the bright region at ~ 1300 km in figure 4.3c. The accumulation of melt at the top of the lower mantle increases liquid overpressure, which initiates the extraction of refractory melt to the magmatic plumbing system. It is at this point, after around 15 Myr, that the evolution of the two modes diverge.

In mode 1, the emplacement of the refractory melts into the upper mantle creates a band of intermediate composition there, but the top of the upper mantle and the lithosphere remain purely composed of the fusible material. Steady state is reached after ~ 30 Myr, coinciding with the attainment of thermal equilibrium, where heat loss from eruptions equals that input by tidal heating. In mode 2, the deep refractory melts make it to the surface, and the lithosphere — initially composed of purely fusible material — becomes of intermediate composition. As there is little to no emplacement in the upper mantle the downwelling lithosphere maintains its composition, which results in cyclic behaviour where the composition of new lithosphere depends on the downwelling composition of the lithosphere a few Myr previously. For example, the initial, purely fusible lithosphere creates a pulse of fusible melt at ~ 40 Myr, which produces a new pulse of erupta, more fusible than that in the intervening period. This cycle continues with a decreasing amplitude of differences between erupta compositions until eventually a steady state is reached after ~ 200 Myr. Thermal equilibrium is reached after ~ 100 Myr, which can be seen by the constant eruption rate after ~ 100 Myr in figure 4.3e.

4.3.3 Bulk composition and mantle emplacement rate

Figure 4.4 shows how lithospheric thickness, mantle structure, eruption rate, and erupted composition vary as a function of bulk composition for three values of h_M. The primary control on whether the model is in mode 1 or mode 2 is the mantle emplacement constant h_M, but figure 4.4 shows that bulk composition also exerts a significant control. The results in figure 4.4 are produced using the reduced, steady-state model. The agreement of the reduced model and the full model is demonstrated in figure 4.1.

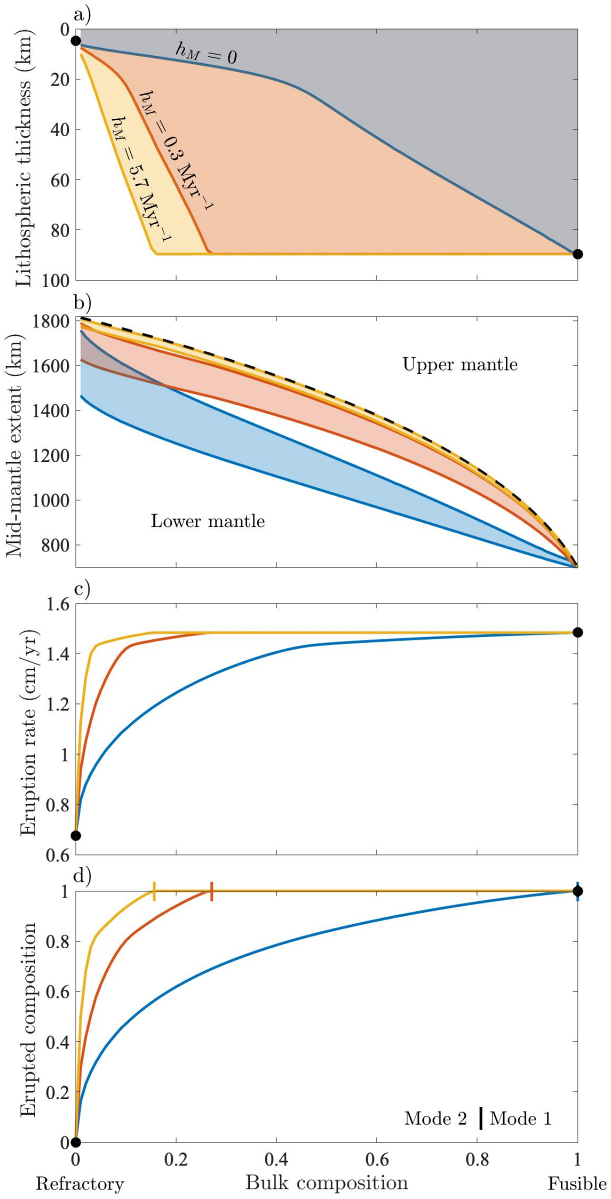

Figure 4.4: Reduced model solutions of a) lithospheric thickness, b) location of the mid-mantle, c) eruption rate, and d) erupted composition for varying bulk composition, for three values of h_M. Refractory material can reach the lithosphere (mode 2) when h_M is low, and/or when the bulk composition is refractory (panel d). Higher temperature erupta provide a more efficient heat loss mechanism, so at steady state the eruption rate must decrease (panel c), and this results in a thinner lithosphere (panel a). When refractory material is all frozen in the mantle (at higher values of h_M or more fusible bulk compositions), the system is in mode 1. High values of h_M create a smaller lower mantle and a large upper mantle for a given bulk composition (panel b). The dotted line on panel b shows the boundary between the upper and lower mantle if fully segregated.

Refractory bulk compositions produce bodies with large refractory lower mantles and thin fusible upper mantles, as shown by figure 4.4b. If $h_M = 0$, all of this refractory material reaches the lithosphere upon melting and the model is always in mode 2. When $h_M > 0$, some of the refractory material is emplaced and if there is too little of it (i.e., if the bulk composition is fusible enough) then it is all emplaced before reaching the surface and the erupted composition is purely fusible (mode 1). For a given value of h_M there is a critical bulk composition that divides mode 2 from mode 1 (figure 4.4d). Equivalently, for a given bulk composition there is a critical h_M which divides mode 2 (low h_M) from mode 1 (high h_M).

A prominent feature of figure 4.4 is that the lithospheric thickness and eruption rate both decrease at more refractory bulk compositions. When hot, refractory melt reaches the surface, the eruption rate and lithospheric thickness drop. The drop in lithospheric thickness is due to increased emplacement, which I discuss below.

4.4 Discussion

My results demonstrate that magmatic segregation and volcanic eruptions lead to a rapid stratification of the mantle. Fusible material is cycled in the upper mantle and lithosphere, and its depletion at depth generates a refractory lower mantle that rises to its melting point. The fate of high-temperature refractory magmas formed in the lower mantle controls the degree of chemical stratification and the composition and temperature of erupted products. If high-temperature refractory melts freeze in the upper mantle (mode 1), no refractory lavas will be observed at the surface and the mantle will be fully stratified. Alternatively, if refractory melts can migrate to the surface (mode 2), refractory eruptions will be observed and the mantle will not be fully stratified.

I first discuss the stratification caused by magmatic segregation and the mantle structure it produces. Next I discuss the key results from each mode, analysing their successes and shortcomings in explaining present observations, and their predictions for future observations. I then consider how lower mantle extraction and the migration of deep refractory melts could be interpreted physically, before finally discussing the limitations and future directions of this work.

4.4.1 Stratification by magmatic segregation

The formation of a pure-refractory lower mantle at steady state is a necessary consequence of magmatic segregation in my model. Magmas that form in the lower mantle rise toward the upper mantle, leaving behind an increasingly refractory residuum, a feature shown in the time evolution plots in figure 4.3. The composition of the lower mantle only reaches steady state when all fusible material has been removed. Compositional stratification in my model can be best understood by noting that solids are continually moving downward (see solid flux in figure 4.1c,g), and are continually heated as they downwell. Continued heating of intermediate compositions produces fusible melts that segregate buoyantly upward, leading to increasingly refractory compositions with depth.

The structure of the mid- and upper mantle depends on both the phase diagram and the fate of refractory magmas produced in the lower mantle. For my simple two-component phase diagram, the upper mantle is at the fusible melting temperature T_A, and the mid-mantle must span the temperature range between T_A and the temperature T_B of the pure-refractory region below. The reduced model shows that the thickness of the mid-mantle ($T_A < T < T_B$) is determined by the rate at which downwelling solid is heated from T_A to T_B, which is slowest (and thus the mid-mantle is thickest) when no emplacement takes place there. If emplacement of the lower refractory magma there is very efficient (see the largest value of h_M and the dotted line in figure 4.4b) the mid-mantle is thin and there is almost complete segregation between a pure refractory lower mantle and a pure fusible upper mantle. On the other hand, if refractory melts migrate far into the upper mantle, stratification is less complete. The upward migration reduces the thickness of the pure refractory lower mantle, and increases the thickness of intermediate-composition upper mantle.

With a more detailed phase diagram, I would expect a general structure similar to that proposed here but with greater complexity. In particular, the chemistry of the lithosphere and uppermost mantle would likely be much more complex, with layering controlled by melting temperature, and potentially influenced by near-surface sulphur cycling. Sulphur may be acting as a volatile that reduces melting temperatures (Battaglia et al., 2014). The formation of a lowermost olivine layer is expected to be a feature of any relevant silicate phase diagram, and so my prediction of the formation of high temperature refractory melts is expected to hold. Any temperature range in the mantle over which there is not significant melting would be present as a low-melt-fraction layer that acts as a barrier to melts rising from below, potentially leading to magma overpressure and, in the context of my model, transfer to a plumbing system.

4.4.2 Implications of the two magmatic modes

In this section I discuss the specific results and implications of each mode, analysing the degree to which each mode can explain current observations, and the predictions they make of future observations.

In mode 1, high-temperature refractory magmas formed in the lower mantle migrate into the upper mantle and freeze, delivering their latent heat to the fusible surroundings. The additional melting this emplacement causes can manifest as a high-melt-fraction decompacting layer, as seen in figure 4.1b. Magnetic induction models have been used to infer the presence of a ≥ 50 km region of $\geq 20\%$ melt fraction beneath Io's lithosphere (Khurana et al., 2011). This has been previously interpreted as a region of concentrated tidal heating (Tobie et al., 2005; Bierson and Nimmo, 2016), or as I presented in Chapter 3, a decompacting boundary layer. Mode 1 of my model shows another manifestation of this decompaction hypothesis; a high melt fraction layer can arise due to freezing of deep refractory melts into the upper mantle. This is a result of the viscous resistance of the mantle to decompaction, and does not occur if the viscosity of the mantle is small, as shown by the solutions to the reduced model in figure 4.1, in which this viscous resistance is effectively ignored. A decompacting layer, whether caused by freezing or the strength of the lithosphere, provides a means of generating high melt fractions in the upper mantle without requiring concentrated tidal heating in this layer.

Mode 1 predicts that no eruptions of refractory material take place. This could be considered consistent with the lack of observed olivine on the surface of Io, although this apparent absence may simply reflect an observational limitation (Geissler et al., 1999). The key deviation of mode 1 from observations is that it does not predict any high temperature eruptions. For mode 1 to produce high temperature eruptions would require invoking processes like viscous heating on ascent (Keszthelyi et al., 2007).

In mode 2, refractory melts formed in the lower mantle rise to the base of the lithosphere and are ultimately erupted. This predicts the presence of refractory phases on the surface. If Io behaves according to mode 2 of my model, the abundance of refractory phases at the surface could be used to constrain the intrusive behaviour and bulk composition through model outputs like those in figure 4.4. The relative lack of upper mantle emplacement in mode 2 means that melting throughout the upper mantle is caused predominantly by tidal heating (Moore, 2001). A key strength of mode 2 in relation to observations lies in its prediction of high eruption temperatures. This provides a means of reconciling heat flow arguments that require heat transport by magmatic segregation (Moore, 2003; Breuer and Moore, 2015), with observations of high temperature eruptions (McEwen et al., 1998; de Kleer et al., 2014). Mode 2 supports the hypothesis of Keszthelyi and McEwen (1997) that eruptions of deep, refractory melts formed within a stratified Io could produce very high temperature lavas.

Here I expand on that suggestion, demonstrating the dynamical conditions necessary for such eruptions. The rise of deep refractory melts to the surface is a means of recycling deep material to the lithosphere, and so the upper mantle is never fully depleted in refractory material.

The eruption rate predicted by mode 2 is lower than that in mode 1. At steady state and given the negligible surface conduction, the heat lost through eruptions must equal that input by tidal heating. Increasing the temperature of erupted material means therefore that a lower eruption flux is needed (figure 4.4c). Despite this decreased eruption rate, in my model there is very little change in total melting. The combination of the decreased eruption rate and the approximately constant total melt production means that more emplacement of intrusions takes place in bodies operating in mode 2. This effect was explained in Chapter 3, where I showed that the emplaced fraction is given by $C(T_{\text{erupt}}-T_{\text{surf}})/(L+C(T_{\text{erupt}}-T_{\text{surf}}))$, where C is the specific heat capacity, L is the latent heat, T_{erupt} is the eruption temperature, and T_{surf} is the surface temperature. The increased emplacement yields a thinner lithosphere than mode 1 for the same value of the lithospheric emplacement constant h_L. However, I note that the appropriate value of h_L is not known, so larger lithospheric thicknesses could also be produced in mode 2, with emplacement spread over a larger region.

A conclusive detection of olivine on Io's surface would provide significant support for mode 2, though I note that processes such as fractional crystallisation may evolve magmas in the lithosphere, meaning that a lack of surface olivine cannot conclusively rule out mode 2. Further, additional observations to constrain the globally averaged volcanic eruption rate and eruption temperature would also test whether refractory melts are migrating out of the deep mantle. On the basis of its ability to explain high eruption temperatures originating from a mantle governed by magmatic segregation, I propose that mode 2 is the more likely state for Io.

4.4.3 Mechanism of ascent for deep refractory magmas

A fundamental assumption of my model is that deep refractory melts are able to migrate out of the lower mantle without equilibration as they rise. From a modelling perspective, I assume that this occurs due to the accumulation of magmatic overpressure in the lower mantle, which enables melt to leave the lower mantle through some arbitrary 'magmatic plumbing system'. In the model, this plumbing system is treated in the same way as the plumbing system in the lithosphere, which I envision as a network of dikes. However, its physical manifestation in the mantle may well be different. In this section I first discuss the assumption that refractory magmas can leave the lower mantle, and then discuss possible physical interpretations of the plumbing system.

If Io is indeed in a thermal steady state (Lainey et al., 2009), heat supplied to the lower mantle must be able to leave to the upper mantle. The heat being transported is primarily in the form of latent heat (Moore, 2001), which can only be lost by the freezing of lower mantle melts. If lower mantle melt was not extracted to a plumbing system, it would have to freeze at the top of the lower mantle where the temperature drops, passing its latent heat to fusible material at the base of the upper mantle, which would melt and continue heat transport upward. I consider such a perfect exchange of mass and energy unlikely due to the extreme liquid overpressures it would generate. These large liquid overpressures would be expected to cause melt to penetrate the overlying upper mantle, which is at its solidus and so is unlikely to have significant strength. The mantle magmatic plumbing system is intended to capture the range of possible fates of this lower mantle melt. The ultimate freezing and heat transfer could take place at the very base of the upper mantle (large h_M); in a distributed region of the upper mantle (intermediate h_M); or in the lithosphere and on the surface (small or zero h_M).

Assuming then that magma does leave the lower mantle, its rise could be accomplished in a number of ways. The lower mantle is hotter and, at the top, has a higher porosity than the overlying mid- and upper mantle. Together these create a lower bulk density that gives the potential for a Rayleigh-Taylor overturn. In my model, the entire mantle is on its solidus, so I would not expect significant resistance to such an overturn on long timescales. In this interpretation, h_M parameterises the equilibration of rising refractory plumes with their surroundings. If the plumes are large and rise rapidly, the degree of equilibration may be very low, representing mode 2 of my model. Such an overturn represents a mode of convective heat transport. Another possibility is that lower mantle melts rise through a system of dikes. High magma pressure in the decompacting boundary layer may localise and nucleate fractures that are driven by magmatic buoyancy. It is possible that such conduits become semi-permanent features, although this would require large amounts of lateral melt transport in the decompacting boundary layer. Interpretations of my deep magmatic plumbing system as a system of dikes would presumably imply a higher value of h_M than large convective plumes. Related to the concept of lower mantle melts rising through dikes is the formation of reactive channels. If rising refractory melts are corrosive to more fusible compositions, they can localise into high-flux channels (Kelemen et al., 1995; Rees Jones and Katz, 2018). Rising lower mantle melts are undersaturated in SiO_2 and so may dissolve pyroxene and precipitate olivine. This could create high permeability, pure-olivine conduits that allow for the rapid upward rise of refractory melts.

I emphasise that my model makes no explicit assumption about the nature of this plumbing system, other than that it provides some mechanism for upward transport with an efficiency determined by the parameter h_M. Further work might pursue a more detailed mechanistic interpretation, but that is beyond the scope of this thesis.

4.4.4 Model limitations and future work

This work represents an initial step toward a full coupling of geodynamics and thermochemistry in volcanic bodies like Io. I have used a simplified phase diagram that, whilst providing useful insight into the general processes of stratification, could be significantly extended. Revisiting previous thermochemical modeling (Keszthelyi and McEwen, 1997; Keszthelyi et al., 2007) in light of the dynamics presented here could give a more realistic picture of the compositional structure of Io. I have also ignored the pressure dependence of melting temperature, the different latent heats of refractory and fusible material, and solid-state phase changes. While I justified these simplifications, a more complete model would aim to incorporate their effects. Further, I did not consider the possibility that the two chemical components and their melts may have different densities. This, and the one-dimensionality of the model precludes my ability to investigate thermochemical convection, which may be an important part of this system, as discussed below.

In this work I have also neglected the radial distribution of tidal heating. In Chapter 3 it was demonstrated that the lithospheric balances of eruption, emplacement and lithospheric thickness depend only on the integrated heating from below, not its distribution. In the present case, the thicknesses and melt fractions of the different layers in the model would change with variable tidal heating with radius, but the general principles of stratification and melt migration will hold. Future work may aim to couple dynamic models like that presented here with evolving tidal dissipation models. In Chapter 5 I investigate the effects of spatially variable tidal dissipation on the single component model of Chapter 3, but do not expand this to the two-component model presented here.

Another significant simplification in my model is the assumption of spherical symmetry. Tidal heating is a function of not just radius but also latitude and longitude (Segatz et al., 1988; Ross et al., 1990), and may lead to lateral temperature differences on the order of ~ 100 K (Steinke et al., 2020). Such considerations will be key to deciphering the links between interior dissipation and heat transport, and the surface expression of volcanism. If, as speculated above, convective overturn is a mechanism of upward migration of buoyant refractory melts, then future work should include this inherently symmetry-breaking process.

The model here is developed to describe leading-order dynamics and compositional evolution; more detailed three-dimensional models are probably needed to facilitate close comparisons to specific surface observations or to make predictions of the surface distribution of eruption products. Such models would be best constrained by more detailed observations of eruptive heat fluxes, temperatures, and petrology.

4.4.5 The possibility of solid-state convection

A potentially significant limitation to my model is its neglect of compositional and thermal density variations. At the pressures relevant for Io's mantle, Fe is expected to preferentially partition into the melt. Such an interpretation of my compositional model might suggest an unstable density stratification with hot, Fe-depleted, refractory material in the lower mantle, and cooler, Fe-enriched, fusible material in the upper mantle (Ballmer et al., 2017). Indeed Keszthelyi and McEwen (1997) proposed that an Fe-rich mid-mantle would form due to the production of fractionated Fe-rich melts. Unstable density stratifications are expected to result in convective instabilities. In this section I therefore discuss the possibility of convective instabilities arising from the chemical structures predicted in this work.

Consider a highly simplified system of two static layers of thickness b separated by a horizontal boundary, where the upper layer (layer 1) has density ρ_1 and the lower layer (layer 2) has density $\rho_2 < \rho_1$. Both layers have the same viscosity η. Such a configuration is susceptible to a Rayleigh-Taylor instability. Turcotte and Schubert (2014) show that the fastest-growing wavelength of instability is given by $\lambda = 2.568b$, with a growth rate $\tau_\alpha = 13.04\eta/(\rho_1 - \rho_2)gb$. Taking b to be half the thickness of Io's mantle, we get a wavelength of $\sim$ 1300 km; with a viscosity of $\eta = 10^{20}$ Pa s and a density difference of 100 kg/m^3, the growth rate of the instability is $\sim$ 200 kyr. This can be compared to the $\sim$ 20 Myr timescale for advection across half the depth of the mantle. This simple calculation indicates that the structure presented in this work may be susceptible to very long-wavelength convective instabilities.

Long-wavelength convective overturn would induce the rise of refractory material, potentially affecting the spatial distributions of eruption products.

The applicability of such a calculation to the full system of downwelling solid and buoyantly segregating magma is not immediately clear, especially given the close links between melting, composition, temperature, and density. If convective overturns are able to re-mix the mantle, the drive for compositional convection will be removed. This may lead to episodic behaviour where the mantle becomes increasingly stratified until a convective overturn occurs and resets the compositional structure. Alternatively, convective overturns may sequester Fe at the base of the mantle, removing it from the system considered here. A full analysis of the propensity for thermochemical convection as a consequence of magmatic segregation and volcanism is an interesting avenue of future research. It would require a two-dimensional (at least) model, and potentially a more elaborate petrological parametrisation to assess the partitioning of Fe. It is interesting to note, however, that convection in this system will not necessarily alter heat transport in the way that it does in other systems, since conduction already plays an essentially insignificant role in the one-dimensional structure my model has predicted. Heat transport occurs almost entirely through advection of latent heat by the buoyantly ascending melt, which we might expect to be relatively unaffected by convective motion of the solid. On the other hand, the effect of convection on composition would likely be more significant.

4.5 Conclusions

In this chapter I have demonstrated that magmatic segregation and volcanic eruptions can rapidly lead to significant compositional stratification of Io's mantle. This stratification produces a refractory lower mantle and a fusible upper mantle and lithosphere. Melting of the refractory lower mantle produces high-temperature melts that must leave the lower mantle in order to facilitate heat loss. The fate of these refractory melts controls the degree of stratification of the mantle and the composition and temperature of erupted lavas. If high-temperature, refractory melts reach the surface, they can provide an explanation of the highest temperature observed eruption, but if they stall in the upper mantle, high temperature eruptions are not predicted. I hypothesise that Io's highest temperature eruptions originate from a deep lower mantle, and that their eruption limits the stratification of the upper mantle. Future observations of the petrology and temperature of eruptions will directly test this hypothesis.

Appendix

4.A Model scaling and non-dimensional parameters

Here I non-dimensionalise the governing equations of the full model. Much of this process is the same as in Appendix 3.A. Dimensional parameters and definitions are given in table 4.1. Scales and definitions of the non-dimensional parameters are given in table 4.A.1. I write, for example, $u = u_0\hat{u}$ where u_0 is the solid velocity scale and $\hat{u}$ is the dimensionless velocity, insert similar expressions for all the variables into the equations, and finally drop the hats on the dimensionless quantities to arrive at a dimensionless model. As in Chapter 3, for temperature I write $T = T_{\text{surf}} + T_0\hat{T}$, but here I take $T_0 = T_B - T_{\text{surf}}$, so that a non-dimensional temperature of 1 denotes the melting point of refractory material. I assume spherical symmetry and write all quantities as a function of r.

The non-dimensional equation for conservation of mass in the lithosphere–mantle and plumbing system are

$$\frac{1}{r^2}\frac{\partial}{\partial r}(r^2(u+q)) = -E + M, \tag{4.13}$$

$$\frac{1}{r^2}\frac{\partial(r^2 q_p)}{\partial r} = E - M. \tag{4.14}$$

Conservation of the phase-average composition $\overline{c}$ is

$$\frac{\partial \overline{c}}{\partial t} + \frac{1}{r^2}\frac{\partial}{\partial r}\left[r^2(\phi_0\phi u + q)c_l\right] + \frac{1}{r^2}\frac{\partial}{\partial r}\left[r^2(1-\phi_0\phi)uc_s\right] = -Ec_l + Mc_p. \tag{4.15}$$

Conservation of chemical composition in the plumbing system is

$$\frac{1}{r^2}\frac{\partial}{\partial r}(r^2 q_p c_p) = Ec_l - Mc_p. \tag{4.16}$$

Darcy's law and the compaction equation become

$$q = \phi^n\left(1-\phi_0\phi-\delta\frac{\partial P}{\partial r}\right), \tag{4.17a}$$

$$\frac{P}{\zeta} + \frac{1}{r^2}\frac{\partial}{\partial r}\left[r^2\phi^n\left(1-\phi_0\phi-\delta\frac{\partial P}{\partial r}\right)\right] = -E, \tag{4.17b}$$

where δ is a dimensionless compaction parameter defined in Chapter 3 and table 4.A.1. Conservation of energy becomes

$$\frac{\partial H}{\partial t} + \frac{1}{r^2}\frac{\partial}{\partial r}(r^2(u+q)T) + \frac{\mathrm{St}}{r^2}\frac{\partial}{\partial r}(r^2(\phi_0\phi u+q)) = \frac{1}{\mathrm{Pe}\,r^2}\frac{\partial}{\partial r}\left(r^2\frac{\partial T}{\partial r}\right) + \mathrm{St}\,\psi + M(T_p+\mathrm{St}) - E(T+\mathrm{St}), \tag{4.18}$$

where Pe is the Peclet number, St is the Stefan number (table 4.A.1), and where bulk enthalpy has been scaled by $T_0\rho C$. Conservation of energy in the plumbing system is

$$\frac{1}{r^2}\frac{\partial}{\partial r}(r^2 q_p T_p) = ET - MT_p. \tag{4.19}$$

Table 4.A.1: Reference scales and non-dimensional parameters

Quantity	Symbol	Definition	Preferred Value	Units
Tidal heating scale	ψ_0		4.2×10^{-6}	$\mathrm{W/m^3}$
Liquid velocity scale	q_0	$\psi_0 R/\rho L$	6.4×10^{-9}	m/s
Solid velocity scale	u_0	q_0	6.4×10^{-9}	m/s
Porosity scale	ϕ_0	$K_0 \phi_0^n \Delta\rho g/\eta_l$	0.044	
Temperature scale	T_0	$T_m - T_s$	1550	K
Bulk viscosity scale	ζ_0	η/ϕ_0	2.3×10^{21}	Pa s
Pressure scale	P_0	$\zeta_0 q_0/R$	8.0×10^{6}	Pa
Péclet Number	Pe	$q_0 R/\kappa$	1160	
Stefan Number	St	L/CT_0	0.25	
Emplacement constant	$\hat{h}$	$h\rho C T_0/\psi_0$	200	
Extraction constant	$\hat{\nu}$	$\nu\zeta_0$	1000	
Scaled elastic limit temperature	$\hat{T}_e$	$\frac{T_e - T_s}{T_m - T_s}$	0.6	
Compaction parameter	δ	$\zeta_0 K_0 \phi_0^n/\eta_l R^2$	5.8×10^{-3}	

The tidal heating scale ψ_0 is imposed, which gives the velocity scale q_0 which in turn gives the porosity scale ϕ_0.

4.B Numerical implementation

Equations (4.13) – (4.19) are solved for phase averaged composition $\overline{c}$, plumbing system composition c_p, compaction pressure P, enthalpy H, plumbing system flux q_p, and plumbing system temperature T_p respectively, using the finite volume method. Other variables are obtained from these six primary variables. In particular enthalpy and phase-averaged composition uniquely define temperature, porosity, solid composition, and liquid composition through the solidus and liquidus equations (4.1) – (4.2), the scaled definition of bulk enthalpy $H = T + \mathrm{St}\,\phi_0\phi$, and the definition of phase averaged composition $\overline{c} = \phi_0\phi c_l + (1-\phi_0\phi)c_s$. This local (cell-wise) problem is solved with a Newton method.

For the numerical solution, I introduce a small amount of artificial diffusion of phase-averaged composition into the system as it helps to avoid discontinuous gradients in composition. The modified composition equation including this artificial diffusion is

$$\frac{\partial \overline{c}}{\partial t} + \frac{1}{r^2}\frac{\partial}{\partial r}\left[r^2(\phi_0\phi u + q)c_l\right] + \frac{1}{r^2}\frac{\partial}{\partial r}\left[r^2(1-\phi_0\phi)uc_s\right] = \frac{D_c}{r^2}\frac{\partial}{\partial r}\left(r^2\frac{\partial \overline{c}}{\partial r}\right) - Ec_l + Mc_p, \quad (4.20)$$

where D_c is a constant that controls the size of the artificial diffusion. A value of $D_c \sim 5\times10^{-4}$ is generally required for robust convergence, and can be decreased with grid refinement. The effect of this diffusion can be seen in figure 4.1d,h where the solid composition of the full model deviates slightly from that of the reduced model. Figure 4.1 shows that the introduction of this diffusion does not affect the model results.

The monolithic system (equations (4.13) – (4.19)) is highly non-linear and tightly coupled (Katz et al., 2007). Robust convergence is obtained by splitting the system into three non-linear sub-system solvers shown schematically in figure 4.B.1. The first sub-system solves equation (4.15) for phase averaged composition $\overline{c}$, and equation (4.18) for enthalpy H. Time integration is performed using the theta method. When $\theta = 0$ the system is fully explicit, and is fully implicit when $\theta = 1$. Initially $\theta = 0.5$ is used, but if convergence fails an explicit timestep is taken. Sub-system 1 employs Newton's method (with globalization). As part of the residual evaluation for this sub-system, a local non-linear solve for porosity, temperature, and solid and liquid compositions (described above) is required.

Once a solution is found for sub-system 1, the result is passed to solver 2, which solves equation (4.17b) for compaction pressure P using Newton's method (with globalization). This separates the non-linearity of permeability in equation (4.17b) from the composition–enthalpy system in sub-system 1, which also computes porosity. Solver 2 also calculates the Darcy flux q and solid velocity u.

Upon convergence, the solutions to the previous two sub-systems are passed to solver 3, which contains the plumbing system equations (4.14), (4.16), and (4.19). Placing the plumbing system equations in a separate non-linear solver separates them from the pressure dependence of extraction, and the temperature/plumbing system flux dependence of emplacement. Even so convergence can be poor when new regions of extraction emerge, which causes rapid changes to the solutions between timesteps. As per the previous two sub-systems solvers, solver 3 also employs Newton's method (with globalization). If Newton fails to converge, I use a pseudo transient continuation method with implict (backward Euler) time integration. The pseudo transient problem is evolved to steady-state to yield the solutions to equations (4.14), (4.16), and (4.19).

An adaptive time step is used. At the beginning of each time step k, a trial value for the step size $\Delta t_k = 1.005\ \Delta t_{k-1}$ is selected. The time step is aborted if any of the solvers for the three sub-systems fail to converge, and the step size is reduced by 50%. In the event of multiple sub-system solve failures, when $\Delta t_k < 1 \times 10^{-12}$, an explicit timestep is taken using Δt_{k-1}, and the process of step size reduction is repeated. The simulation is terminated if an explicit step with $\Delta t_k < 1 \times 10^{-12}$ fails to converge.

After the convergence of all three non-linear sub-systems, a unified residual to the monolithic

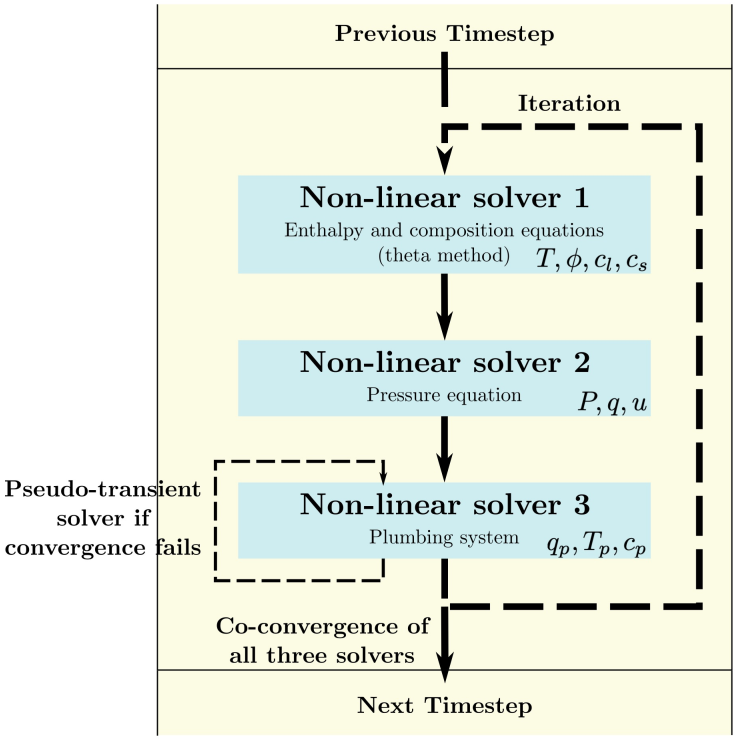

Figure 4.B.1: Schematic of the solver used for the full model. The system is split into three non-linear solvers for enthalpy and composition, pressure, and the plumbing system. The solutions to each solver are iterated until all solvers agree to within some small tolerance. A pseudo-transient solver is used for the pipe equations when convergence is poor.

non-linear problem (4.13) – (4.19) is computed. Successive solution of the three sub-systems are continued until the ℓ_2-norm of the residual of each discrete PDE is $< 1 \times 10^{-7}$. Once satisfied, the time step is accepted and the state of the time-dependent PDE is advanced in time from t_k to $t_{k+1} = t_k + \Delta t_k$.

The discretisation and system of non-linear equations is solved using the Portable, Extensible, Toolkit for Scientific computation (PETSc) (Balay et al., 1997, 2019, 2020).

4.C Reduced model

Illuminating simplifications can be made to the full model by assuming small porosity and zero compaction length — this involves neglecting terms in ϕ_0 and δ within the scaled equations. Conservation of composition in the lithosphere–mantle system becomes

$$\frac{\partial \overline{c}}{\partial t} + \frac{1}{r^2}\frac{\partial}{\partial r}\left(r^2 q c_l\right) + \frac{1}{r^2}\frac{\partial}{\partial r}\left(r^2 u c_s\right) = -E c_l + M c_p. \tag{4.21}$$

I assume that extraction E is zero outside of boundary layers at the base of any solid regions, where it acts to transfer any liquid flux q to the plumbing flux q_p. E can therefore be thought of as a delta function on the boundaries between partial melt and solid (as boundary layers go to zero thickness in the zero-compaction-length approximation).

Darcy's law and the compaction relation become

$$q = \phi^n, \tag{4.22a}$$

$$\phi P = -\frac{1}{r^2}\frac{\partial(r^2 q)}{\partial r}. \tag{4.22b}$$

The reduced energy equation (4.18) splits naturally into two cases: 'solid', in which case $q = 0$ and we have

$$u\frac{\partial T}{\partial r} = \frac{1}{\mathrm{Pe}\, r^2}\frac{\partial}{\partial r}\left(r^2\frac{\partial T}{\partial r}\right) + \mathrm{St}\,\psi + M(T_p - T + \mathrm{St}); \tag{4.23}$$

and 'partially molten', in which case given the phase diagram of pure component B (figure 4.2) we have constant T (either at T_A or T_B) and

$$\mathrm{St}\,\frac{1}{r^2}\frac{\partial(r^2 q)}{\partial r} = \mathrm{St}\,\psi + M(T_p - T + \mathrm{St}), \tag{4.24}$$

where I recall that all extraction occurs on boundaries and so E is absent. In partially-molten regions the compaction pressure is thus given by

$$P = \frac{\mathrm{St}\,\psi + M(T_p - T + \mathrm{St})}{\mathrm{St}\,\phi}. \tag{4.25}$$

Informed by solutions to the full model, I seek solutions that have a partially molten, pure-refractory lower-mantle with $T = T_B$ and $\bar{c} = 0$, occupying $r_m < r < r_b$; a mid-mantle solid region $r_b < r < r_a$ where $T_A < T < T_B$; an upper-mantle partially molten region $r_a < r < r_l$ where $T = T_A$; and a solid lithosphere $r_l < r < R$ where $T_s < T < T_A$. Note that the mid-mantle region in the full model has non-zero porosity, but since the porosity and Darcy flux there are small, it is treated as a pure solid region in this reduced model.

Throughout, I note that solid velocity $u = -q - q_p$ is known from q and q_p. In the deep refractory mantle, the enthalpy equation (4.24) can be integrated to give

$$q = \frac{\psi}{3}\left(r - \frac{r_m^3}{r^2}\right), \qquad r_m < r \le r_b. \tag{4.26}$$

In particular, this gives the value q_b at the position r_b (which is to be determined). This flux is transferred to the plumbing system, which then has temperature $T_p = T_B$ and composition $c_p = 0$. In the region $r_b < r < r_a$, we have to solve

$$u\frac{\partial T}{\partial r} = \frac{1}{\mathrm{Pe}\,r^2}\frac{\partial}{\partial r}\left(r^2\frac{\partial T}{\partial r}\right) + \mathrm{St}\,\psi + M(T_p - T + \mathrm{St}), \tag{4.27}$$

$$\frac{1}{r^2}\frac{\partial(r^2 q_p)}{\partial r} = -M, \tag{4.28a}$$

$$M = \hat{h}_M(T_B - T)\mathcal{I}_M, \tag{4.28b}$$

where $\mathcal{I}_M$ is an indicator function that is zero when $q_p = 0$ and 1 otherwise. This problem is very similar to that solved for the lithosphere in Chapter 3. It is solved with boundary conditions

$$\begin{aligned} T = T_B, \quad \frac{\partial T}{\partial r} = 0, \quad q_p = q_b \quad &\text{at } r = r_b \\ T = T_A \quad &\text{at } r = r_a. \end{aligned} \tag{4.29}$$

If the position of r_a is known (or guessed — see below), this problem determines the position of r_b, as well as the temperature profile and the plumbing flux $q_{p,a}$ at r_a. This problem can be solved with a shooting method as in Chapter 3.

In the partially molten upper mantle ($r_a < r < r_l$) where $c_s \leq 1$, from the phase diagram we have $c_l = 1$, $c_p = 0$, and $T = T_A$. Equation (4.21) therefore tells us that the solid composition is simply given by

$$c_s = -\frac{q}{u}. \tag{4.30}$$

The emplacement rate $M = \hat{h}_M(T_B - T_A)$ is constant and so the plumbing flux is

$$q_p = \left(q_{p,a}\frac{r_a^2}{r^2} - \hat{h}_B(T_B - T_A)\frac{r^3 - r_a^2}{3r^2} \right) \mathcal{I}_{qp} \tag{4.31}$$

where the indicator function $\mathcal{I}_{qp}$ indicates that this quantity cannot go below zero. The reduced enthalpy equation (4.24) then gives

$$q = \frac{\psi}{3}\left(r - \frac{r_a^3}{r^2} \right) + \left(1 + \frac{T_B - T_A}{\mathrm{St}} \right)\left[q_{p,a}\frac{r_a^2}{r^2} - q_p \right] + q_a\frac{r_a^2}{r^2}. \tag{4.32}$$

The second term here is the melting due to the heat released when material is emplaced from the plumbing system. The final term comes from balancing energy at the interface $r = r_a$; since there is a temperature gradient below, the Stefan condition (jump condition for the enthalpy equation) gives a sudden melt flux

$$q_a = -\frac{1}{\mathrm{St}\,\mathrm{Pe}}\frac{\partial T}{\partial r}\bigg|_{-}, \tag{4.33}$$

where the temperature gradient here is known from the solution of (4.27) – (4.29). From these solutions we know the plumbing flux $q_{p,c}$ and liquid flux q_l arriving at the lithosphere–mantle boundary r_l (which is to be determined). Since the flux q_l is then transferred to the plumbing system, the plumbing system in the lithosphere subsequently has constant temperature and composition given by

$$c_p = \frac{q_l}{q_{p,l} + q_l}, \tag{4.34a}$$

$$T_p = \frac{q_{p,l} T_B + q_l T_A}{q_{p,l} + q_l}. \tag{4.34b}$$

Note that if all refractory material has been emplaced beneath the lithosphere, then $q_{p,c} = 0$ and this simply says that the lithospheric plumbing system has $c_p = 1$, and $T_p = T_A$. Within the region $r_l < r < R$, we have to solve the system

$$u\frac{\partial T}{\partial r} = \frac{1}{\mathrm{Pe}\, r^2}\frac{\partial}{\partial r}\left(r^2 \frac{\partial T}{\partial r}\right) + \mathrm{St}\,\psi + M(T_p - T + \mathrm{St}), \tag{4.35}$$

$$\frac{1}{r^2}\frac{\partial (r^2 q_p)}{\partial r} = -M, \tag{4.36a}$$

$$M = \hat{h}_C (T_p - T)\mathcal{I}_M. \tag{4.36b}$$

This system has the boundary conditions

$$\begin{aligned} T = T_A, \quad \frac{\partial T}{\partial r} = 0, \quad q_p = q_l + q_{p,l}, \quad &\text{at } r = r_l, \\ T = T_s \quad &\text{at } r = R. \end{aligned} \tag{4.37}$$

This system is solved the same way as the mid-mantle solid region: a shooting method is used to find the position r_l, as well as the lithospheric temperature distribution and the plumbing flux. Seeking a particular bulk composition for silicate Io, a guess can be made of r_a, and a Newton method used on the resultant bulk composition to find the position of r_a that gives the desired bulk composition.

Figure 4.1 shows solutions to the reduced model as dashed lines, showing good agreement with the full model. There are slight differences in the position of the mid-mantle that arise in the full model due to the smoothed solidus (equation (4.1)).

CHAPTER 5

Spatially variable tidal dissipation, magmatism and volcanism

The model, results, and analysis presented in this chapter have been published in Spencer et al. (2021). This chapter constitutes a minor reformatting of that work to fit within the broader context of this thesis.

5.1 Introduction

In Chapter 3 I investigated Io's 'top-down tectonics', where the eruption and burial of lava, combined with the low surface temperature leads to the growth of a thick and cold lithosphere in spite of the high surface heat flux. This high heat flux is primarily exported from the interior by magmatic segregation in the mantle (Moore, 2001), and through volcanic 'heat-pipes' in the lithosphere (O'Reilly and Davies, 1981). Heat is supplied to the interior by tidal dissipation — a process of great importance in the Solar System (de Kleer et al., 2019b) — and the distribution of input tidal heating is expected to control the surface heat flux distribution (Ross et al., 1990; Tackley, 2001; Kirchoff et al., 2011; Beuthe, 2013; Rathbun et al., 2018; Steinke et al., 2020). However, the implications of tidal heating for interior structure, magma dynamics, tectonics, and topography are not well known.

The spatial distribution of tidal heating is a longstanding and still largely unresolved problem in planetary science (Segatz et al., 1988; Roberts and Nimmo, 2008; Beuthe, 2013; Bierson and Nimmo, 2016; Renaud and Henning, 2018). The end-members generally considered for Io are that of lower-mantle heating or asthenosphere heating (Segatz et al., 1988; Ross et al., 1990; Tackley et al., 2001; Hamilton et al., 2013), though magma-ocean dissipation has also been proposed (Tyler et al., 2015; Hay et al., 2020). Lower-mantle dissipation predicts high polar heat fluxes, whereas asthenospheric dissipation predicts high equatorial heat fluxes. A number of works have sought to identify tidal dissipation patterns from surface heat fluxes (Veeder et al., 2012), volcanic activity (Rathbun et al., 2018), and volcano distributions (Ross et al., 1990; Kirchoff et al., 2011; Hamilton et al., 2013). The primary hindrance to these works is the poor polar coverage of observations, so whilst a number of these works favour an asthenosphere heating model (e.g., Ross et al., 1990; Kirchoff et al., 2011), the general consensus is that more polar observations are needed to fully address this question (Rathbun et al., 2018; de Kleer et al., 2019b). Further, long-timescale, averaged heat fluxes are difficult to estimate, and it is unclear to what extent short-timescale observations of volcanic activity reflect the global dissipation structure. Tectonic features, which vary on much longer timescales, may provide a more robust link between surface observations and the distribution of tidal heating.

An important tectonic feature that is expected to relate to the surface heat flux, and thus the tidal heating distribution, is the long-wavelength lithospheric thickness (Ross et al., 1990; Steinke et al., 2020). In Chapter 3 I proposed that the eruption and burial of lava results in the growth of a cold lithosphere, with a steady-state thickness that is controlled by the balance of downward advection and heat delivered by magmatic intrusions. Conduction plays a minor role in this model because the rate of burial is so large. In such a system, the lithospheric thickness is primarily controlled by the rate of melt production and the rate of intrusive heating. An alternative model was put forward by Steinke et al. (2020), who proposed a stagnant lid convection model where a portion of mantle heat transport occurs by convection, and this convectively-transported heat is transported though the lithosphere by conduction. This predicts that the lithosphere is thinnest where heat flux is highest. It should be noted that Steinke et al. (2020) referred to the surface layer as the crust; I have used lithosphere instead because the crust is usually considered to be a petrologically distinct layer, a distinction that becomes important in the isostatic calculations below. If the thickness of the lithosphere can be related to topography and heat flow, then long-wavelength variations in lithospheric thickness could be used to infer the tidal heating distribution. Constraints on the lithospheric thickness could also be combined with future spacecraft measurements of Io's libration amplitude to investigate its interior structure (Van Hoolst et al., 2020).

The model I presented in Chapter 3 and that in Steinke et al. (2020) propose different controls on the lithospheric thickness and so may be expected to predict different relationships between the tidal heating distribution and thickness. Steinke et al. (2020) used radially integrated tidal heating profiles to predict the effect of spatially variable tidal heating on lithospheric thickness, finding that the thickness anti-correlates with surface heat flux. In this chapter I extend my model from Chapter 3 to consider the effect of variable tidal heating on the eruption and intrusion model for lithospheric thickness such that comparisons can be made between my models and Steinke et al. (2020).

I generalise the simplified, steady-state model presented in Chapter 3 (and derived in Appendix 3.B) to allow variable tidal heating. Io is divided into a set of laterally contiguous, one-dimensional columns that are coupled to a viscoelastic tidal heating model. The tidal heating model calculates a three-dimensional heating rate from a spherically symmetric rheological structure. This leads to a recognised limitation of these type of tidal heating models; the three-dimensional heating rate that they produce generates a non-spherically symmetric structure that cannot be used to recalculate the heating distribution without averaging over spherical shells (Roberts and Nimmo, 2008; Bierson and Nimmo, 2016). Thus, models coupling such tidal heating calculations to dynamics cannot be fully self-consistent. I use this coupled, pseudo-three-dimensional model to investigate the links between tidal heating, lithospheric thicknesses, and long-timescale eruption rates/heat fluxes. My results show that the relationship between lithospheric thickness and heat flux depends on how magmatic intrusions form within the lithosphere. If the rate of formation of permanent magmatic intrusions is independent of the (non-zero) magma flux through volcanic conduits, as may be expected if the volcanic system exploits pre-existing fractures, I predict the lithosphere to be thickest where radially integrated heating rate (and thus eruption rate and heat flux) is highest. If, however, magmatic intrusions form at a rate proportional to the magma flux in volcanic conduits, as may be expected if volcanic conduits form due to basal magma pressure that generates new pathways for magma to propagate into the lithosphere, the lithospheric thickness should be weakly anti-correlated with radially integrated heating rate.

Having predicted the lithospheric thickness and its global variation, I then use a simple isostasy calculation to convert it to topography. This calculation assumes that the density difference between the lithosphere and mantle, which depends on both temperature and composition, is known. If the lithosphere is assumed to be compositionally similar to the mantle, thermal effects control density variations, and are such as to predict that topography anticorrelates with lithospheric thickness. If, on the other hand, the lithosphere is assumed to be compositionally distinct and of a lower chemical density, topography is predicted to correlate with thickness. These isostasy results are an independent extension to the lithospheric thickness calculation; the lithospheric thickness calculations do not require assumptions about the compositions or densities of the lithosphere and mantle. The isostasy model relates a feature that generally has to be indirectly inferred (lithospheric thickness), to an observation that is more readily obtained (topography). Improved observations of surface heat fluxes and their relationships to lithospheric thickness and topography will test different models for the controls on Io's lithospheric thickness (that presented in this thesis and that from Steinke et al., 2020). With a means of critically evaluating these models, the structure of tidal heating can feasibly be constrained by future estimates of lithospheric thickness.

5.2 Methodology

My model consists of two main parts: a theory for magmatic segregation and volcanism, and another for tidal dissipation. I also append a separate isostasy calculation. The one-dimensional magmatic segregation and volcanism model is a generalisation of the asymptotic approximation presented in Chapter 3. In it, melting is driven by the tidal dissipation model, which most closely follows the approach of Beuthe (2013), utilising a Maxwell viscoelastic rhology. Rheological parameters required by the tidal calculation are predicted by the segregation and volcanism model, completing the coupling of the two systems. The isostasy calculations utilise the equal-pressure formulation of Hemingway and Matsuyama (2017).

The dynamics are described by the magmatic segregation and volcanism model. In Chapter 3 I derived a system where tidal heating causes the formation of magma in the mantle that rises buoyantly toward the solid lithosphere. High magma overpressure just below the base of the lithosphere facilitates a transfer of magma from the pore space into a lithospheric magmatic plumbing system, which can be thought of as a system of dikes. Magma rising in this plumbing system can freeze into the cold, surrounding lithosphere, forming permanent magmatic intrusions, delivering both mass and energy to the surroundings. The rest of the magma in the plumbing system rises to the surface and erupts, imparting a compensating downward flux of the (now cold) erupted products. In Chapter 3 I found that the delivery of heat from the freezing of magmatic intrusions is required to raise the temperature of cold, downwelling lithosphere such that a lithospheric thickness within observational constraints can be maintained. The formulations for emplacement utilised in this chapter are discussed below.

The dynamic model is coupled to tidal dissipation to yield a consistent, three-dimensional structure. I use a spherically symmetric structure to calculate a three-dimensional heating rate. This heating rate distribution (which importantly is not spherically symmetric) is applied to a suite of column models, producing a three-dimensional structure. This structure is averaged over spherical shells and used to re-calculate the heating distribution. This processes is iterated until the heating-distribution converges, yielding the three-dimensional structures that I present here. I utilise a Maxwell viscoelastic law despite the well-documented inability of such a rheological law to produce observed dissipation rates at realistic mantle viscosities (Bierson and Nimmo, 2016; Renaud and Henning, 2018). I also neglect all lateral flow, justified by the long-wavelength of the tidal forcing; the one-dimensional columns are considered isolated. This is a significant simplification that I discuss below, and I note that future work should aim to analyse the propensity for lateral flow. I also inherit some of the assumption I made in Chapter 3, namely that I ignore the chemical composition and as a consequence neglect the possibility of compositional convection in the mantle. Parameter values are given in table 5.1.

5.2.1 Magmatic segregation and volcanism

The model presented in Chapter 3 is based on conservation equations for mass, momentum, and energy in a compacting two-phase medium, together with conservation of mass in a magmatic plumbing system that transports magma through the solid lithosphere. Here, I make use of the simplified model described in Appendix 3.B. In the mantle, which is at the melting temperature T_m, tidal heating produces melt, and mass conservation of the melt phase reads

$$\frac{1}{r^2}\frac{\partial\left(r^2 q\right)}{\partial r}=\frac{\psi}{\rho_m L} \tag{5.1}$$

where $q = K_0\phi^n\Delta\rho g/\eta_l$ is the Darcy segregation flux related to the porosity ϕ, ρ_m is the density of the mantle, ψ is the local volumetric heating rate (see section 5.2.2), and L is the latent heat. Here K_0 is a permeability constant, n is the permeability exponent, $\Delta\rho$ is the

Table 5.1: Model parameters

Quantity	Symbol	Preferred Value	Units
Dynamics model			
Radial position	r		m
Radius	R	1820	km
Core radius[1]	r_m	700	km
Solid velocity	u		m/s
Segregation flux	q		m/s
Volcanic plumbing flux	q_p		m/s
Porosity	ϕ		
Permeability constant[2]	K_0	10^{-7}	m^2
Permeability exponent[2]	n	3	
Reference mantle density	ρ_m	3000	kg/m^3
Solid–liquid density difference	$\Delta\rho$	500	kg/m^3
Gravitational acceleration	g	1.5	m/s^2
Liquid viscosity	η_l	1	Pas
Emplacement rate	M		s^{-1}
Emplacement constant*	λ_c	1.66	Myr^{-1}
Emplacement constant*	λ_q	0.05	km^{-1}
Temperature	T		K
Melting temperature	T_m	1500	K
Surface temperature	T_s	150	K
Latent heat	L	4×10^5	J/kg
Specific heat capacity	C	1200	J/kg/K
Thermal diffusivity	κ	10^{-6}	m^2/s
Tidal heating model			
Colatitude	θ		rad
Longitude	φ		rad
Orbital frequency	ω_f	4.11×10^{-5}	s^{-1}
Orbital eccentricity	e	4.1×10^{-3}	
Time	t		s
Complex stress tensor	$\tilde{\boldsymbol{\sigma}}$		Pa
Complex strain tensor	$\tilde{\boldsymbol{\epsilon}}$		
Tidal potential	Ω		m^{2}s^{-2}
Associated Legendre polynomial	$P_l^m(x)$		
Shear viscosity	η		Pas
Reference shear viscosity**	η_0		Pas
Activation energy	E_A	3×10^5	J/mol
Reference temperature	T_0		K
Porosity constant	Λ	27	
Tidal heating rate	ψ		W/m^{-3}
Isostasy model			
Pressure	P		Pa
Depth	z		km
Compensation depth	r_{ccd}		km
Reference lithosphere density	ρ_l	ρ_m	kg/m^3
Lithosphere density	ρ		kg/m^3
Thermal expansivity	α	3×10^{-5}	K^{-1}
Lithospheric thickness	l		km
Topography	h		km

[1]Bierson and Nimmo (2016), [2]Katz (2008), [3]Lainey et al. (2009)

* Chosen to give an average lithospheric thickness of ∼ 35 km

** Chosen to give a total heating rate of 10^{14} W density difference between the solid and liquid, and η_l is the magma viscosity (numerical values are given in table 5.1). The magma flux is therefore

$$q = \frac{1}{\rho_m L}\frac{1}{r^2}\int_{r_m}^{r} \psi r^2 \, \mathrm{d}r, \tag{5.2}$$

where r_m is the base of the mantle. At the base of the lithosphere this flux is transferred to the plumbing system, in which the flux is denoted q_p. Conservation of mass and energy in the lithosphere are described by

$$\frac{1}{r^2}\frac{\partial}{\partial r}\left(r^2(u+q_p)\right) = 0, \tag{5.3a}$$

$$\frac{1}{r^2}\frac{\partial}{\partial r}\left(r^2 q_p\right) = -M, \tag{5.3b}$$

and

$$\frac{1}{r^2}\frac{\partial}{\partial r}\left(r^2 uT\right) = \frac{1}{r^2}\frac{\partial}{\partial r}\left(r^2\kappa\frac{\partial T}{\partial r}\right) + \frac{\psi}{\rho_m C} + M\left(T_m + \frac{L}{C}\right), \tag{5.4}$$

where u is the solid velocity, T is the temperature, M is the emplacement rate (the rate at which magmatic intrusions remove material from the plumbing system), and C is the specific heat capacity. The final term in equation (5.4) represents the heating that emplacement provides to the downwelling lithosphere. The solution of equations (5.3) – (5.4) together determines the temperature profile in the lithosphere as well as the lithospheric thickness (see Chapter 3 for details).

In Chapter 3 I introduced three feasible parametrisations for the magmatic emplacement rate M; the first related to the temperature difference between volcanic material and the surroundings, the second related to the flux through the volcanic systems, and the third had a constant emplacement rate. I showed that all three mechanisms produced broadly the same behaviour, with high emplacement rates producing low lithospheric thicknesses, and demonstrating that emplacement must be predominantly in the lower-lithosphere in order to produce the large elastic thicknesses required of supporting Io's mountains. In this Chapter

I investigate the two simpler forms of emplacement that I have introduced, both of which can be used to derive analytical expressions for the lithospheric thickness, as I show below. To allow emplacement to be proportional to the volcanic flux, or a constant, I take

$$M = \lambda_c + \lambda_q q_p, \tag{5.5}$$

and explore cases where only one of λ_c or λ_q is non-zero at a time. Taking a constant emplacement rate ($\lambda_c \neq 0$ and $\lambda_q = 0$) can be interpreted as modelling a system of dikes where the number of dikes is fixed but the flux through them varies. If emplacement is a function of contact area with the host rock, such a system could result in emplacement rate being independent of the magma flux. This is similar to, but more simple than the temperature dependence taken in Chapter 3. Taking emplacement to be proportional to the amount of melt in the plumbing system ($\lambda_c = 0$ and $\lambda_q \neq 0$) can also be interpreted as a system of dikes, but where the dikes have equal fluxes and the number of dikes varies. As the flux (and thus the number of dikes) increases, the contact area with the host rock also increases, and so the total emplacement rate increases. In summary, I consider cases where emplacement is positively related to, or independent of the magma flux. I do not consider the possibility of a negative relationship between emplacement rate and magma flux as I cannot conceive of a realistic physical system that this would represent.

Finally, it is important to note that λ_c and λ_q parametrise long-timescale averages of a range of complex processes. As such, I do not attempt to closely interpret the numerical values of these parameters; I use values that give rise to a globally-averaged lithospheric thickness that is comparable to that inferred from observations. I focus on the broad behaviour of the model in response to these parameters. I also note from equation (5.5) that λ_c has the same units as M (s^{-1}), whereas because q_p multiplies a flux, it has units m^{-1}.

5.2.2 Tidal heating

For the calculation of tidal heating I most closely follow the methodology of Beuthe (2013). Volumetric tidal dissipation averaged over an orbit is given by (Tobie et al., 2005)

$$\psi(r,\theta,\varphi) = \frac{\omega_f}{2}\left[\mathrm{Im}(\tilde{\sigma}_{ij})\mathrm{Re}(\tilde{\epsilon}_{ij}) - \mathrm{Re}(\tilde{\sigma}_{ij})\mathrm{Im}(\tilde{\epsilon}_{ij})\right], \tag{5.6}$$

where $\omega_f = 4.11 \times 10^{-5}\ \mathrm{s}^{-1}$ is the orbital frequency, θ is the colatitude, φ is the longitude, $\tilde{\sigma}_{ij}$ and $\tilde{\epsilon}_{ij}$ are the components of the complex stress and strain tensors, and summation over components i and j is implied. I present a derivation of equation (5.6) from force balance equations in a two-phase medium in Appendix 5.B. I calculate the complex stress and strain tensors using the propagator matrix approach detailed in Sabadini and Vermeersen (2004), and explained in appendix A of Roberts and Nimmo (2008). I give some details of this approach in Appendix 5.B. Broadly, the calculation starts with the formulation of momentum conservation and Poisson equations for a body subjected to gravitational and rotational potentials. These equations are then expanded in spherical harmonics. This results in a set of six ODEs for the radially-varying spherical harmonic coefficients, which are solved in each layer of a spherically symmetric body. Together with a rheological law these coefficients yield the complex stress and strain tensors.

The tidal potential that forces the system arises from consideration of a synchronous eccentric orbit, to first order in eccentricity. It is given by (Kaula, 1964; Tobie et al., 2005)

$$\Omega = r^2\omega_f^2 e\left[-\frac{3}{2}P_2^0(\cos\,\theta)\cos(\omega_f t) + \frac{1}{4}P_2^2(\cos\,\theta)\left[3\cos(\omega_f t)\cos(2\varphi) + 4\sin(\omega_f t)\sin(2\varphi)\right]\right], \tag{5.7}$$

where $e = 4.1 \times 10^{-3}$ is the orbital eccentricity, θ and φ are the colatitude and longitude (the latter being zero at the sub-Jovian point), t is the time, and P_2^0 and P_2^2 are associated Legrendre polynomials.

To couple the tidal heating model to the dynamical model I follow the approach of Bierson and Nimmo (2016). I take the shear viscosity to be a function of temperature and porosity through the relationship (Katz, 2010)

$$\eta = \eta_0 \exp\left[\frac{E_A}{R_g}\left(\frac{1}{T} - \frac{1}{T_0}\right) - \Lambda\phi\right], \tag{5.8}$$

where $E_A = 3 \times 10^5$ J/mol is the activation energy, R_g is the gas constant, η_0 is a reference viscosity at the reference temperature T_0 (taken to be the melting point), and $\Lambda = 27$ is a positive constant. Temperature T and porosity ϕ are extracted from the model in section 5.2.1 and averaged over spherical shells, so η depends only on radius r. The value of η_0 used is chosen so that the total global rate of tidal dissipation approximately matches the observed dissipation rate of $\sim 1 \times 10^{14}$ W (Lainey et al., 2009). It is well documented that a Maxwell viscoelastic constitutive law requires a very low viscosity to produce the amount of tidal heating observed in Io (Segatz et al., 1988; Tackley, 2001; Bierson and Nimmo, 2016; Steinke et al., 2020). I assume that this is a failure in the present understanding of the rheology that affects dissipative processes (Bierson and Nimmo, 2016; Renaud and Henning, 2018), rather than a reasonable assesment of Io's long-timescale mantle viscosity. Bierson and Nimmo (2016) also take a porosity dependence of the elastic shear modulus, but I neglect this small effect in line with my simplified approach. I refer to the first coupled model, using (5.8), as the 'mantle heating' model.

Numerous previous works have considered the possibility that tidal dissipation is concentrated within a lower-viscosity asthenosphere (e.g., Segatz et al., 1988; Tackley, 2001; Hamilton et al., 2013; Davies et al., 2015). Such a dissipative layer does not arise in the above formulation, even when a large decompacting boundary layer is included in the dynamic model because the porosity dependence in a Maxwell viscoelastic model is too weak. In order to investigate the lithospheric thickness and long-wavelength topography implications of such a dissipation structure, I calculate an alternative 'asthenospheric heating' model, where the shear viscosity in a 300 km layer beneath the lithosphere is set to be a factor of 1000 lower than the rest of the mantle. In the asthenospheric heating model I do not include the temperature and porosity dependence of shear viscosity; in this case the tidal heating model is decoupled from the dynamical model. I do, however, set the shear viscosity in the cold lithosphere is be effectively infinite so no dissipation occurs there, consistent with the calculated dissipation structure in the coupled mantle heating model.

The tidal heating code has been benchmarked against the radial functions in figure 2 of Tobie et al. (2005), against the TiRADE software used in Roberts and Nimmo (2008), and by reproducing figures 8 and 10 of Segatz et al. (1988).

5.2.3 Isostasy calculations

For my isostasy calculations I follow Hemingway and Matsuyama (2017) in using an equal-pressure formulation of isostasy in spherical coordinates. This assumes that compensated columns have equal pressures at their bases (the compensation depth, r_{ccd}). Equal pressure isostasy assumes that we have (Hemingway and Matsuyama, 2017)

$$P = \int_{r_{ccd}}^{R} \rho g \, \mathrm{d}r, \tag{5.9}$$

where P is a constant (independent of latitude and longitude), ρ is the density profile, and R is the local planetary radius. I take gravity g to be uniform for simplicity, a reasonable assumption given the likely heavy core. I assume that density in the lithosphere is a function of temperature only

$$\rho = \rho_l [1 - \alpha (T - T_m)], \tag{5.10}$$

where $\alpha = 3 \times 10^{-5}$ K^{-1} is the coefficient of thermal expansion, and ρ_l is the reference density of the lithosphere at the melting temperature T_m. It is at this point that the distinction between ‘crust’ and ‘lithosphere’ becomes important for Io. In terrestrial systems, the base of the crust represents a petrological boundary between the low-density crust and the high-density mantle. In Chapter 4 I proposed that efficient recycling of erupted material back into the partially molten mantle removes any significant compositional variation across this boundary. In such a view there is no petrologically distinct crust, and so there is no compositionally derived density change between the lithosphere and upper mantle. Consistent with that result, I take $\rho_l = \rho_m$ for our initial topography calculations. It is plausible, however, that certain chemical species are melted and mobilised at lower temperatures, potentially resulting in a density stratification, even if the bulk of the lithospheric material is efficiently recycled into the mantle. I investigate the effect of an upper-most layer with a density $\rho_l \neq \rho_m$ in Appendix 5.A.

The integral in equation (5.9) can be split at the base of the lithosphere, which has a thickness l to write

$$P = \rho_m g(R - l - r_{ccd}) + \int_0^l \rho g \, \mathrm{d}z, \tag{5.11}$$

where $z = R - l$ is the distance downward from the surface. Both l and ρ (in terms of temperature T) are known from the magmatic segregation and volcanism model, so this expression can be re-arranged to determine the variable radius R relative to its spatial average $\overline{R}$. Since P and r_{ccd} are constant, we obtain this topography $h = R - \overline{R}$ as

$$h = l - \int_0^l \frac{\rho}{\rho_m} \, \mathrm{d}z + \text{constant}, \tag{5.12}$$

where the constant is chosen to make the spatial average of h zero.

5.3 Results and discussion

Figure 5.1 shows model solutions for the lithospheric temperature distribution, mantle porosity, and tidal heating distribution at Io's north pole and three points around the equator, for the (coupled) mantle heating model and the (de-coupled) asthenosphere heating model. In the mantle-heating case (figure 5.1a–c), heating rate is highest at the poles, and lowest at the sub- and anti-Jovian points, whereas in the asthenosphere-heating case (figure 5.1d–f), heating rate is highest at the sub- and anti-Jovian points, and lowest at the poles. A higher heating rate leads to increased melt production, though for the permeabilities used here melt fractions only vary by $\sim 1\%$. Lower permeabilities lead to higher porosities and greater porosity variation between localities (Moore, 2001; Bierson and Nimmo, 2016). Throughout this work, eruption rate and surface heat flux are a proxy for radially integrated heating rate.

The rate of emplacement is controlled by λ_c and λ_q (5.5). The values of λ_c and λ_q used in this work were chosen to yield an average lithosphere thickness of ~ 35 km. Increasing these parameters results in a reduction of the average lithospheric thickness, whilst decreasing them increases the average thickness. This reflects the role of the emplacement constant M in controlling lithospheric thickness, as discussed in Chapter 3.

An analysis of the equations can be used to obtain a useful analytical approximation for the lithospheric thickness. When the emplacement rate is a constant ($\lambda_c \neq 0$ and $\lambda_q = 0$), integration of equation (5.3b) in the lithosphere yields

$$q_p = \frac{q_e R^2}{r^2} + \frac{\lambda_c}{3}\left(\frac{R^3}{r^2} - r\right), \quad R - l \leq r \leq R, \tag{5.13}$$

where $q_e = q_p(r = R)$ is the eruption rate. Assuming negligible surface conduction, the eruption rate must be given by a column-wise energy balance as

$$q_e = \frac{1}{R^2(\rho_m L + \rho_m C(T_m - T_s))} \int_{r_m}^{R} \psi r^2 \, \mathrm{d}r, \tag{5.14}$$

where the integral is the total tidal heating delivered to the column. From equation (5.2), the plumbing flux at the base of the lithosphere is

$$q_p(r = R - l) = \frac{1}{(R-l)^2 \rho_m L} \int_{r_m}^{R-l} \psi r^2 \mathrm{d}r. \tag{5.15}$$

Since negligible tidal heating takes place in the lithosphere (figure 5.1, note that the green shaded region denotes the upper 100 km, which includes part of the upper mantle where dissipation is not negligible), the integrals in (5.14) and (5.15) are essentially identical. Thus, equating (5.15) with (5.13) at the base of the lithosphere yields an analytical expression for the lithospheric thickness in terms of the local eruption rate

$$l = R - R\left(1 - \frac{3q_e}{R\lambda_c}\frac{C(T_m - T_s)}{L}\right)^{1/3}. \tag{5.16}$$

A Taylor expansion of the term in brackets provides some intuition into this expression. Expanding to the first non-trivial term yields

$$l \approx \frac{C(T_m - T_s)}{L}\frac{q_e}{\lambda_c}. \tag{5.17}$$

The thickness of the lithosphere is controlled by the balance between latent heat release in the lithosphere and sensible heat loss at the surface. The greater the temperature difference between erupting lava and the surface, the more heat that must be provided to downwelling material to raise it to its melting point. As the eruption rate increases, material downwells more quickly, and with no corresponding increase in emplacement rate, the thickness of the lithosphere grows. This effect can be seen in the main panels of figure 5.1. A higher rate of emplacement means that downwelling material is heated more rapidly, reducing the lithospheric thickness. I note that an average lithospheric thickness can be estimated using the modelled global average eruption rate in Chapter 3.

The insets in panels a and d of figure 5.1 show the lithospheric temperature profiles when emplacement rate is proportional to the plumbing system flux ($\lambda_c = 0$ and $\lambda_q \neq 0$). In this case equation (5.3b) can be integrated to give

$$q_p = \frac{R^2 q_e}{r^2} \mathrm{e}^{\lambda_q (R-r)}. \tag{5.18}$$

Again assuming negligible surface conduction and equating equation (5.18) to the total melt production in the interior (equation (5.15)) gives an expression for the lithospheric thickness,

$$l = \frac{1}{\lambda_q} \ln \left(1 + \frac{C(T_m - T_s)}{L} \right). \tag{5.19}$$

Interestingly, this is independent of the melting rate, so lithospheric thickness is expected to be virtually constant when emplacement rate is proportional to the plumbing system flux. A Taylor expansion of (5.19) to first order yields equation (5.17) but with q_e/λ_c replaced by $1/\lambda_q$, illustrating that in this case, the relationship between eruption flux and emplacement is fixed. The small variations in lithospheric thickness seen in the insets in panels a and d of figure 5.1 are due to conduction (which is neglected in arriving at the estimate, equation (5.19)), with higher heating rates producing thinner lithospheres.

Figure 5.2 shows lithospheric thickness, eruption rate, and topography as a function of latitude and longitude in the coupled mantle-heating model. The top row of figure 5.2 shows the case where emplacement rate is a constant and the bottom row shows the case where emplacement rate is proportional to the plumbing system flux. A constant emplacement rate means that lithospheric thickness correlates with the eruption rate, as specified by equation (5.16). Lithospheric thickness varies by about 25 km, with the most pronounced variation being between the thick polar lithosphere and the thin equatorial lithosphere. In figure 5.2 I assume that there is no compositionally derived density change at the base of the lithosphere, and so take $\rho_l = \rho_m$. The lack of a compositionally density step means that the cold lithosphere is more dense than the underlying, partially molten mantle; this results in topographic highs where the lithosphere is thinnest. The coupled, mantle-heating model

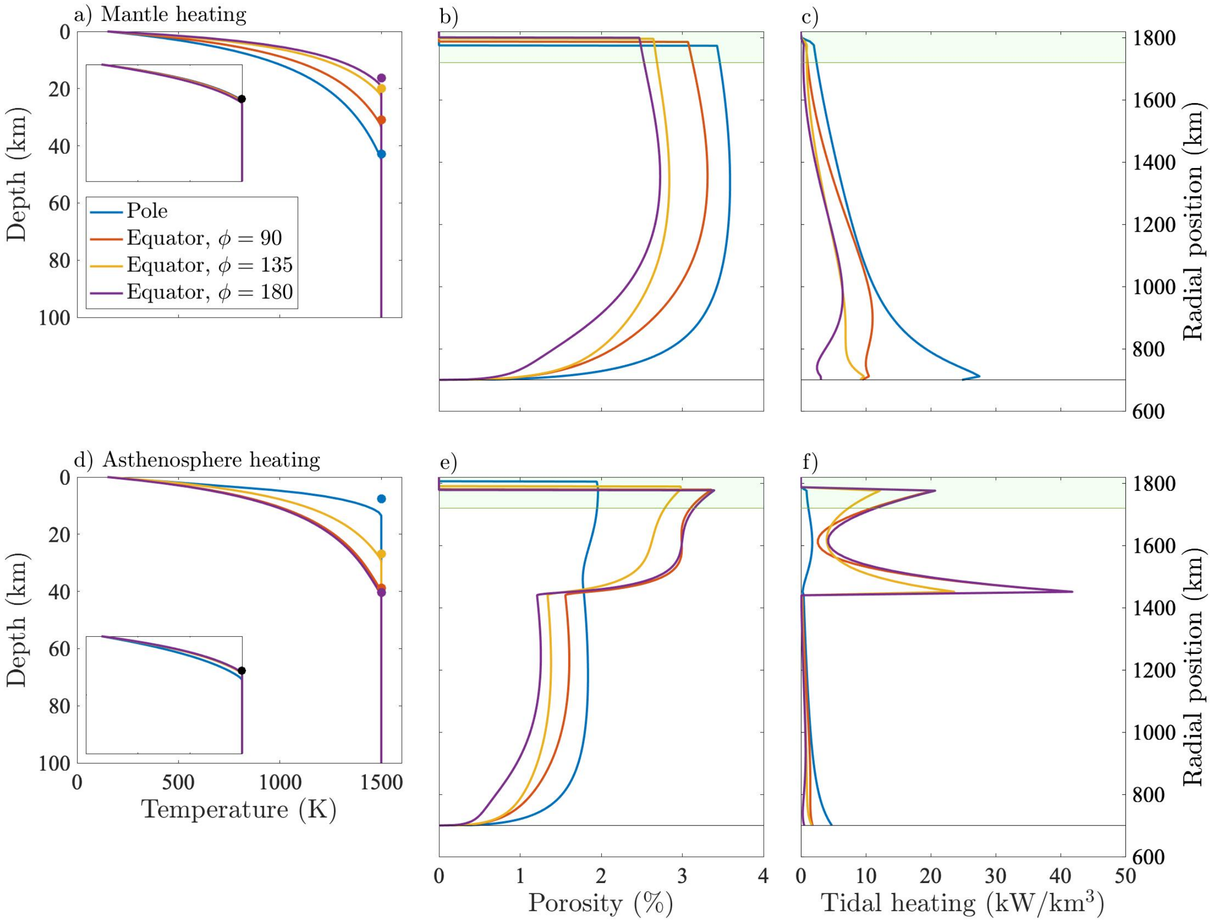

Figure 5.1: Lithospheric temperature profiles, mantle porosities, and tidal heating distributions at the poles and three points around the equator, for the mantle heating (a–c) and asthenosphere heating (d–f) models, with constant emplacement rate, $\lambda_c = 1.66$ Myr^{-1}. Panels a and d show the temperature profile in the top 100 km layer of Io; this region is indicated by the green strip in the other panels, which show porosity and heating in the whole mantle and lithosphere. Where radially integrated heating rate is highest, melt production and porosity is highest. This results in an increased eruptive flux and the growth of a thicker lithosphere. The insets in panels a and d show the case when emplacement rate is proportional to plumbing system flux, with $\lambda_q = 0.05$ km^{-1}. In this case, lithospheric thicknesses vary weakly (porosity and tidal heating profiles in the mantle are almost exactly the same as constant emplacement rate). Dots indicate estimates of lithospheric thickness using equations (5.17) (panels a and d) and (5.19) (insets). Differences between the analytical estimates and the model are caused by conduction, which is neglected in the analytical estimates.

with constant emplacement rate predicts long-wavelength topography with an amplitude of about 250 m. In the case where emplacement rate is proportional to the amount of material in the plumbing system, shown in the bottom row of figure 5.2, the lithospheric thickness only varies by a couple of kilometres and the amplitude of long-wavelength topography is

< 40 m. This can be understood through equation (5.19); increased heating and the resultant increased eruption rate is balanced by increased emplacement, resulting in an almost uniform lithospheric thickness. In this case, the long-wavelength lithospheric thickness and topography variations are a result of different conductive heat fluxes and so lithospheric thickness is anti-correlated with eruption rate (Ross et al., 1990; Steinke et al., 2020). I stress that the lithospheric-thickness solutions are independent of the topography estimates. The topography estimates rely on an assumption of the compositionally derived density difference (or lack thereof) between the lithosphere and mantle, but the lithospheric thickness estimates do not. An exploration of the effect of varying the mantle density is presented in Appendix 5.A.

Figure 5.3 shows the same plots as figure 5.2, but for the case of asthenospheric heating. All of the relationships between heating rate, eruption rate, lithospheric thickness, and topography are the same in this case, but the pattern of dissipation and so the pattern of the plotted solutions is different. Asthenospheric heating predicts higher eruption rates at the equator. If emplacement rate is constant, this predicts a thicker lithosphere at the equator (amplitude $\sim$ 30 km), and assuming $\rho_l = \rho_m$, topographic highs at the poles (amplitude $\sim$ 300 m). If emplacement rate is proportional to the amount of material in the plumbing system, lithospheric thickness is much more uniform (amplitude $\sim$ 6 km) and topography is reduced (amplitude $\sim$ 90 m), with lithospheric thickness variations being controlled by variation in conductive heat fluxes.

Assuming dominantly vertical flow — a significant assumption that I discuss below — the global pattern of heat flow should be reflective of the tidal heating distribution, as has been noted elsewhere (e.g., Segatz et al., 1988; Tackley, 2001; Veeder et al., 2012; Davies et al., 2015). The primary means to distinguish between lower mantle and asthenospheric heating models is on the basis of heat flux. Lower mantle heating predicts higher polar heat fluxes, whereas asthenosphere heating predicts higher equatorial heat fluxes. With

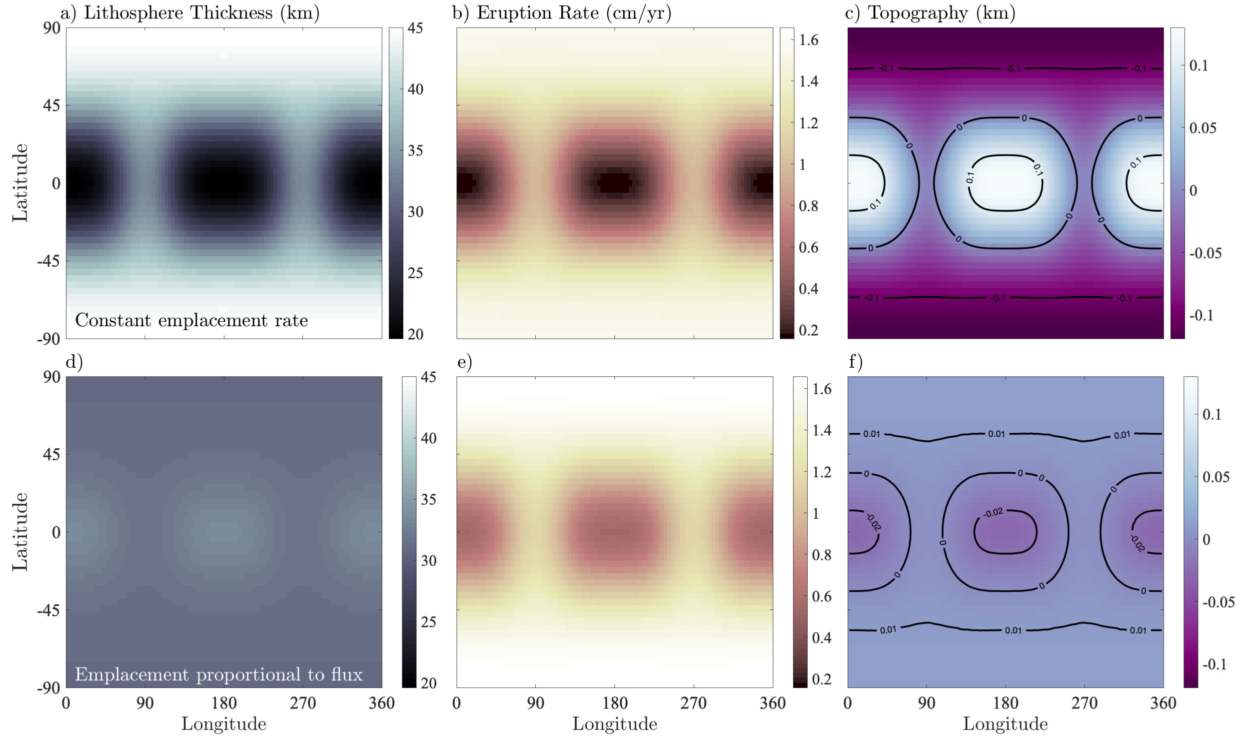

Figure 5.2: Solutions for lithospheric thickness, eruption rate, and topography in the case of coupled dynamics and tidal heating, assuming the mantle and lithosphere have the same density at equal temperature. Tidal heating is concentrated in the lower mantle in the coupled model, producing maximum eruption rates at the poles (see figure 5.1). Panels a–c show the case where emplacement rate is constant, and panels d–f show the case where emplacement rate is proportional to the plumbing system flux. Constant emplacement rate predicts a correlation of lithospheric thickness with eruption rate (or heat loss), and topographic lows where heat flux is high. An emplacement rate proportional to plumbing system flux predicts a relatively uniform lithospheric thickness and little long-wavelength topography.

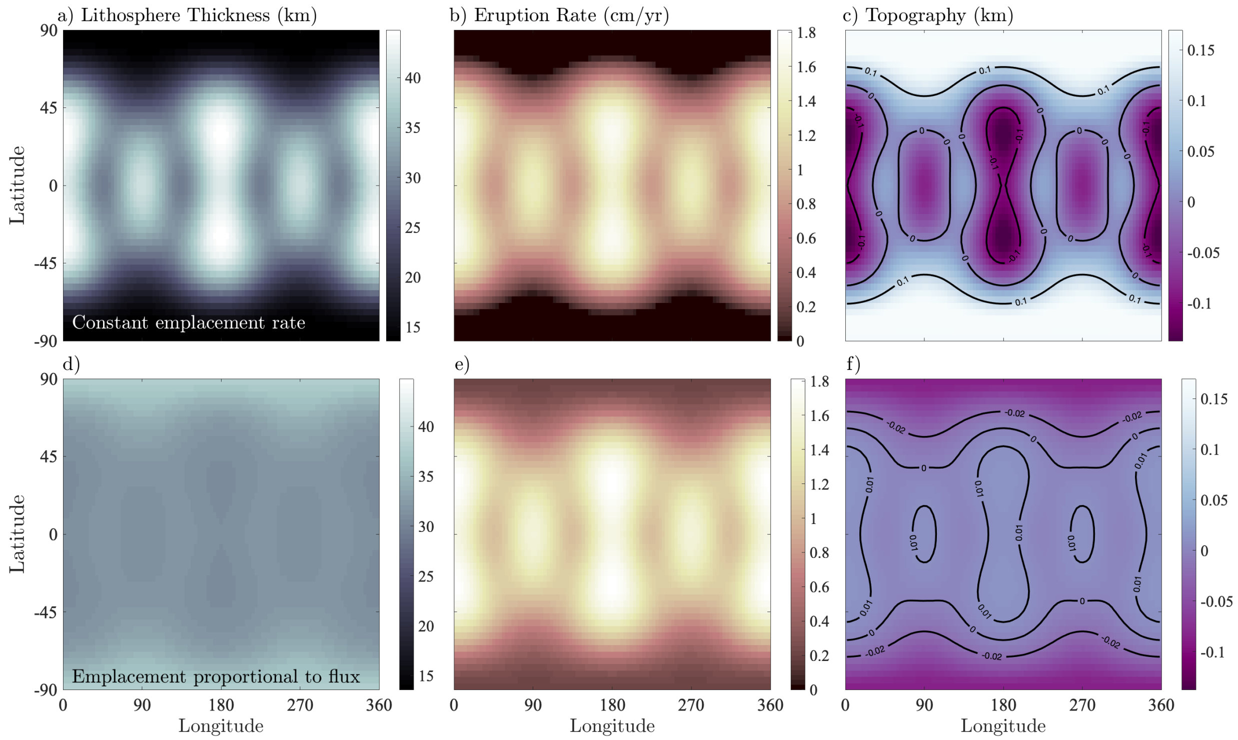

Figure 5.3: Solutions for lithospheric thickness, eruption rate, and topography in the case of asthenosphere heating. Panels a–c show the case where emplacement rate is constant, and panels d–f show the case where emplacement rate is proportional to the plumbing system flux. Relationships between lithospheric thickness, eruption rate, and topography are the same as in figure 5.2, but patterns and amplitudes are different due to the different heating mode.

the present dearth of polar observations, this is a difficult distinction to make. Rigorous observation of Io's poles is required to understand which mode of heating is more likely to be occurring. However, if the mode of emplacement can be established, lithospheric thickness and topography can serve as a useful proxy for long-timescale heat flux.

This work predicts that the long-wavelength variations in lithospheric thickness should either correlate with the long-timescale eruption rate/heat flux, or be weakly anti-correlated, as summarised schematically in figure 5.4. In the constant emplacement rate model, I predict that lithospheric thickness correlates with eruption rate. An explanation for why emplacement would be independent of magma flux could be that volcanic conduits are not formed by magma pressure at depth, but rather tectonic processes in the lithosphere. Io's eruption and burial tectonics are thought to form mountains by thrust faulting (McKinnon et al., 2001; Kirchoff and McKinnon, 2009). If, for example, such faults can act as conduits for magma ascent, freezing of ascending magma on their walls may be largely independent of the flux through the conduit. Alternatively, in the flux-proportional emplacement rate model, I predict that long-wavelength lithospheric thickness varies by only a few kilometers, and is weakly anti-correlated with heat flux. A rationale for why emplacement rate would be proportional to volcanic plumbing flux may be that volcanic conduits are created by overpressured magma at the base of the lithosphere. It is plausible that higher melt production in the interior would lead to a larger number of conduits. If magma in each of these conduits has a chance of stalling within the lithosphere, this would imply a positive relationship between lithospheric magma flux and emplacement rate.

The flux-proportional emplacement rate model makes predictions for variations in lithospheric thickness that are similar to the results of Steinke et al. (2020). When comparing this work to Steinke et al. (2020), it is important to note that whilst both can predict a conductive control on lithospheric thickness variations, the controls on the absolute values of lithospheric thickness are different. In this work the lithospheric thickness is primarily

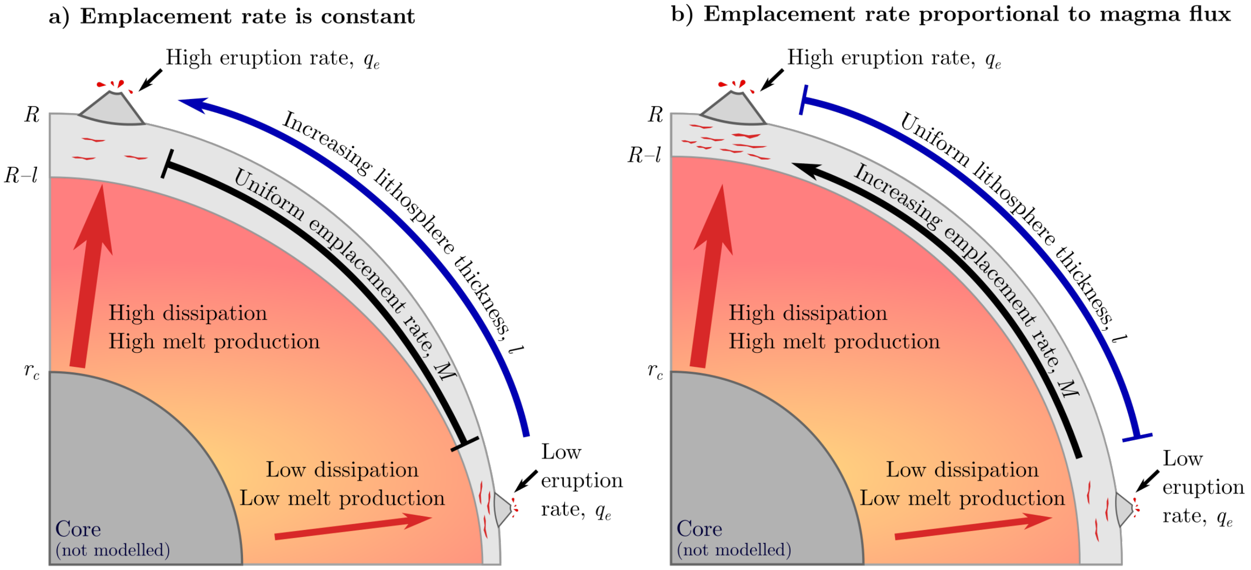

a) Emplacement rate is constant

b) Emplacement rate proportional to magma flux

Figure 5.4: Schematic illustrating the primary results of this chapter. The lithospheric thickness is correlated with radially integrated heating rate if magmatic intrusions form at a constant rate (panel a), but is approximately uniform (or weakly anti-correlated) if intrusions form at a rate proportional to the flux through volcanic conduits (panel b).

controlled by the rate of magmatic emplacement, whereas in Steinke et al. (2020) the lithospheric thickness is controlled entirely by conduction through a stagnant lid. To address the relative importance of convective heat transport in the mantle likely requires a model that couples two-phase flow and convection, a significant challenge due to the different timescales on which these processes operate.

The proposed link between lithospheric thickness and topography provides a means of relating more readily-obtainable observations (topography) to the predictions of lithospheric thickness in works like this one and Steinke et al. (2020). However, to quantify this prediction requires an additional assumption about the relative densities of the lithosphere and mantle. In Chapter 4 I demonstrated that in Io's top-down tectonics, the lithosphere is expected to be efficiently recycled into the mantle, resulting in the lithosphere and upper mantle having the same composition. This is the case presented in figures 5.2 – 5.3, where the densities of the mantle and lithosphere are the same when their temperatures are equal ($\rho_m = \rho_l$). It is nonetheless plausible that as erupta are buried through the lithosphere, fusible components are melted and mobilised first, which may in turn lead to a density stratification. The extent of this effect is perhaps small, however, given the expected mafic nature of Io's lithosphere. In Appendix 5.A I show that if Io does have a distinct layer of different chemical density, its effect on topography depends on the density difference $\rho_m - \rho_l$. At a critical density difference of ~ 30 kg/m^3, the compositional density effect cancels out the temperature dependence of density, resulting in no topography. If $\rho_m - \rho_l$ is sufficiently large, topography is inverted from that presented in figures 5.2 – 5.3. If the density difference can indeed be estimated, topography observations can be compared to eruption rates and volcanic heat fluxes to clarify the heat-transfer and emplacement mechanisms in the lithosphere. Alongside recent work that demonstrates a way to constrain interior structure from libration amplitudes (Van Hoolst et al., 2020), this provides a means to investigate Io's interior structure and heating distribution.

My isostasy calculations assume that compositional variation within the lithosphere can be approximated by a density step at the base of the lithosphere. It is likely that the compositional profile in the lithosphere is complex, reflecting shallow magma fractionation, sulfur cycling, and other processes. If the vertical structure of the lithosphere is approximately uniform with latitude and longitude, and simply scaled to lithospheric thickness, the results in this chapter should be largely unchanged. If, however, there is significant variation in lithosphere composition with latitude and longitude, the applicability of the isostatic model presented here would be reduced. It is not clear, however, that any such variation would mirror the degree-two tidal forcing, and so may average out on the long wavelengths considered here.

White et al. (2014) created a partial stereo-topographic DEM of Io that found a system of longitudinally arranged alternating basins and swells near the equator, with amplitudes $\sim$ 1–2 km and a wavelength ~ 400 km. This large amplitude may imply that compositional density differences are important in controlling topography (see Appendix 5.A), or that dynamic topography caused by upwelling mantle plumes is significant (Tackley et al., 2001). It is important to note however that there are considerable discrepancies between stereo-derived and limb-profile-derived long-wavelength topography (White et al., 2014), and hence that long-wavelength topography is not well constrained. Further, the long-wavelength, isostatic topography described here may be difficult to disentangle from tidal and rotational deformation. Efforts are generally made to remove tidal and rotational effects from global topographic maps, but this process may also inadvertently remove all or part of the topography described here. Improved observations of long-wavelength topography, particularly in the polar regions, as well as a means of disentangling different contributions to long-wavelength topography are required to make robust comparisons between modelled topography and data.

A primary limitation of the work in this chapter is the neglect of lateral flow in either the lithosphere or mantle. Differences in lithospheric thickness are expected to be counteracted by deformation of the lithosphere. Such calculations are common in studies of the ice-shells of icy satellites (Stevenson, 2000; Nimmo and Stevenson, 2001; Nimmo, 2004), where there is a clear rheological and density transition at the base of the shell. The application of such a model to Io is not straightforward because rheological and density transitions are expected to be more gradual (Chapter 4). It is not clear whether there is an easily defined petrological 'crust' of Io. Nonetheless such lateral flow is possible, and would be best investigated by a two-dimensional model of upper Io. Lateral flow is also possible in the partially molten mantle. Pressure gradients would be expected to drive flow of the mobile magma phase. Pressure gradients could be produced by processes such as different melting rates or spatially variable extraction rates to the lithosphere. An investigation of lateral melt flow would likely require a two-dimensional model of the partially molten mantle. Here I simply note that the relationships proposed in this model are expected to hold if vertical motion is much greater than lateral motion, as generally expected in Io's eruption and burial tectonics at long wavelengths.

5.4 Conclusions

I have demonstrated how spatially variable tidal heating leads to long-wavelength variations in lithospheric thickness in a model of magmatic segregation and volcanic eruptions. My models predict that such variations are controlled by how magma intrudes into the lithosphere. If permanent magmatic intrusions form at a rate independent of the magma flux through volcanic conduits, the lithosphere should be thickest where tidal heating is greatest. In this case the lithopshere thickness can vary by 10s of km. If however magmatic intrusions form at a rate proportional to the magma flux through volcanic conduits, lithospheric thickness will only vary by a few km, and will be anti-correlated with eruption rates. I also predict that if density differences are predominantly derived from temperature differences, then areas of thin lithosphere will sit on topographic highs. Improved observational constraints on eruption rates, heat fluxes, and long-wavelength topography, particularly at Io's poles, will help distinguish between different models for the controls on lithospheric thickness.

Appendix

5.A Topographic effects of a petrologically distinct crust

The isostasy calculations presented in this chapter require an assumption about the chemical densities of the lithosphere and the underlying mantle. If the lithosphere and upper mantle have different chemical densities, then this will affect topography. In Io's top-down, heat-pipe tectonics, compositions are expected to become increasingly refractory with depth. Keszthelyi and McEwen (1997) proposed that the near surface would be fusible and composed of low density, silica rich components. This view fell out of favour when improved observations illuminated the mafic to ultra-mafic nature of the lithosphere (Keszthelyi et al., 2007). In Chapter 4, I demonstrated that efficient recycling of erupted lavas back into the mantle prevents the mafic near-surface from significantly differentiating; I proposed that the lithosphere and upper mantle have approximately the same composition. Heat-pipe tectonics appears to result in a relatively uniform composition in the near surface; Io may well lack a petrologically distinct crust.

Figures 5.2 – 5.3 incorporate this assumption, taking the lithosphere and mantle to have the same density at equal temperatures ($\rho_m = \rho_l$). It is plausible, however, that a degree of

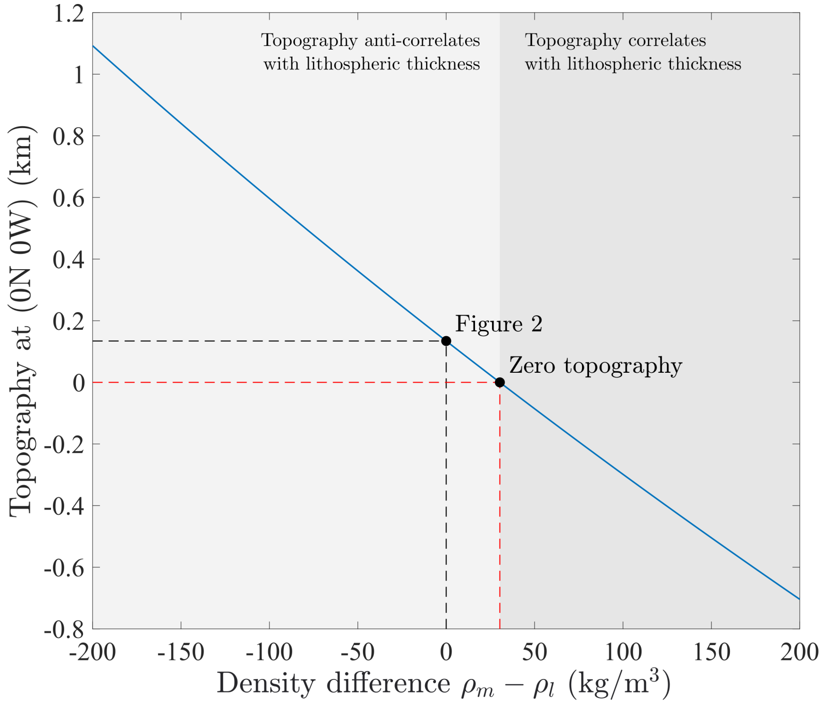

Figure 5.A.1: Topography at the sub- or anti-Jovian point (0N 0/180W) for the coupled mantle heating model as a function of the chemical density difference $\rho_m - \rho_l$ between the upper mantle and lithosphere. If the lithosphere is buoyant with respect to the mantle, topography is expected to correlate with lithospheric thickness. For a density difference of ~ 30 kg/m^3 topography derived from the low lithospheric temperature is cancelled out, resulting in no topography. Figures 5.2 – 5.3 assumed $\rho_m = \rho_l$.

compositional differentiation does take place in the near surface, with more fusible material being mobilised first, which may in turn result in a density difference ($\rho_m \neq \rho_l$). This process likely doesn't produce large density differences for the reasons described above, but may still play a significant role in controlling topography.

Figure 5.A.1 shows the topography at the sub- or anti-Jovian point for the coupled, mantle-heating model as a function of the density difference $\rho_m - \rho_l$. Figure 5.A.1 shows that if the mantle is ~ 30 kg/m^3 more dense than the lithosphere, then the temperature dependence of density in the lithosphere is cancelled out, resulting in no topography. If the density difference is greater than this then the topography patterns in figures 5.2 – 5.3 are inverted.

5.B Calculating spatially variable tidal heating

5.B.1 Derivation of the tidal dissipation rate from force balances

The calculation of tidal heating from the complex stress and strain tensors (globally, equation (2.2), and locally equation (5.6)) is well established in the literature (e.g., Tobie et al., 2005; Beuthe, 2013; Steinke et al., 2020). Here I derive these equation in the context of a two-phase solid-liquid system, ultimately neglecting terms associated with the dissipative processes in two-phase flow.

Force balances for each phase were not explicitly stated in Chapter 3 as the derivation started with Darcy's law, which arises as a consequence of these. Force balances for the solid and liquid phases respectively are

$$-(1-\phi)\,\boldsymbol{\nabla}\, p+\boldsymbol{\nabla}\cdot\boldsymbol{\sigma}'+\phi\frac{\mu}{k_\phi}\boldsymbol{q}+(1-\phi)\rho_s\boldsymbol{g}=0, \tag{5.20}$$

$$-\phi\,\boldsymbol{\nabla}\, p-\phi\frac{\eta_l}{k_\phi}\boldsymbol{q}+\phi\rho_l\boldsymbol{g}=0, \tag{5.21}$$

where $p=p_s-p_l$ is the effective pressure (note that this is related to but distinct from the compaction pressure P defined above), and $\boldsymbol{\sigma}'$ is the deviatoric stress tensor. Inertial terms have been neglected due to the small Reynolds number in the mantles of silicate bodies. In the solid equation the first term is the force caused by pressure differences between phases; the second term is the force caused by deviatoric stresses; the third term is an inter-phase force, and the fourth term is gravity. The liquid equation is similar but I assume that the liquid cannot support deviatoric stress. The rate of mechanical work is computed as the dot product of the phase velocity with the force balance equations (5.20)–(5.21), which are then summed to give

$$\boldsymbol{u}\cdot\boldsymbol{\nabla}\cdot\boldsymbol{\sigma}'-(\boldsymbol{u}+\boldsymbol{q})\cdot\boldsymbol{\nabla}\, p=\frac{\eta_l}{k_\phi}\boldsymbol{q}\cdot\boldsymbol{q}-\boldsymbol{v}_p\cdot\boldsymbol{g}, \tag{5.22}$$

where $\boldsymbol{v}_p = \phi\rho_l\boldsymbol{v}_l + (1-\phi)\rho_s\boldsymbol{u}$. The first term represents the rate at which deviatoric stresses in the solid do work; the second term represents the rate at which liquid pressure gradients do work on both phases; the third term represents the rate of irreversible dissipation by Darcy flow, and the fourth term represents the rate of change of potential energy.

I now consider the power input to the system, which for a two-phase deforming medium is given by

$$P = \int_S \boldsymbol{\sigma}_s \cdot \boldsymbol{u}(1-\phi) \cdot \mathrm{d}\boldsymbol{S} + \int_S \boldsymbol{\sigma}_l \cdot \boldsymbol{v}_l\phi \cdot \mathrm{d}\boldsymbol{S} + \int_V \boldsymbol{v}_p \cdot \boldsymbol{g}\mathrm{d}V, \tag{5.23}$$

which I have written generally, in terms of the full solid tensor $\boldsymbol{\sigma}_s$ and full liquid tensor $\boldsymbol{\sigma}_l$. The solid and liquid tensors, as well as the local gravitational acceleration $\boldsymbol{g}$ are determined by the specific tidal problem in question (see below). Using the definition of the effective stress tensor $\boldsymbol{\sigma} = -p\boldsymbol{I} + \boldsymbol{\sigma}'$, assuming that $\boldsymbol{\sigma}_l' = 0$, and applying Gauss' theorem, this becomes

$$P = \int_V \left(\boldsymbol{u} \cdot \boldsymbol{\nabla}\cdot \boldsymbol{\sigma}' + \boldsymbol{\sigma}' : \boldsymbol{\nabla}\, \boldsymbol{u} - (\boldsymbol{u} + \boldsymbol{q}) \cdot \boldsymbol{\nabla}\, p - p\, \boldsymbol{\nabla}\cdot(\boldsymbol{u} + \boldsymbol{q}) + \boldsymbol{v}_p \cdot \boldsymbol{g}\right) \mathrm{d}V. \tag{5.24}$$

Then, using total mass conservation (4.3) with the assumption that $M = E = 0$ on the timescale of dissipation, and equation (5.22) we have

$$\begin{aligned} P &= \boldsymbol{\sigma}' : \boldsymbol{\nabla}\, \boldsymbol{u} + \frac{\eta_l}{k_\phi}\boldsymbol{q} \cdot \boldsymbol{q}, \\ &= \boldsymbol{\sigma}' : \dot{\boldsymbol{\epsilon}} + \frac{\eta_l}{k_\phi}\boldsymbol{q} \cdot \boldsymbol{q}, \end{aligned} \tag{5.25}$$

where $\dot{\boldsymbol{\epsilon}}$ is the deviatoric strain rate tensor, and I have dropped the integration over the arbitrary volume. P now represents the power input per unit volume. Utilising the first law of thermodynamics ($\dot{E} = P + Q$) for an adiabatic system ($Q = 0$), this power represents the rate of change of internal energy per unit volume. In equation (5.25) the first term represents the change in internal energy caused by deformation of the matrix, and the second term is the irreversible dissipation in Darcy flow. I neglect this Darcy flow dissipation, but note that it may well play an important role in dissipation. With this assumption I arrive at the rate of change of internal energy

$$\dot{E} = P = \boldsymbol{\sigma}' : \dot{\boldsymbol{\epsilon}}. \tag{5.26}$$

We are interested in cyclic deformation with a period T, so I define the volumetric, cycle-averaged power

$$\begin{aligned} P_\circ &\equiv \frac{1}{T} \oint P \mathrm{d}t, \\ &= \frac{1}{T} \int_t^{t+T} \boldsymbol{\sigma}' : \dot{\boldsymbol{\epsilon}} \, \mathrm{d}t. \end{aligned} \tag{5.27}$$

For a purely elastic solid equation (5.27) will integrate to zero, but for a viscoelastic material the phase lag between stress and strain rate will result in dissipation. The relationship between stress and strain rate is determined by the rheological law used. In this chapter I use Maxwell viscoelasticity, as is done in most previous works (e.g., Segatz et al., 1988; Tobie et al., 2005; Roberts and Nimmo, 2008; Steinke et al., 2020), but I do note that other rheological laws have been utilised and may be more appropriate (Bierson and Nimmo, 2016; Renaud and Henning, 2018). The constitutive equation for Maxwell viscoelasticity is

$$\dot{\boldsymbol{\sigma}}' + \frac{\mu}{\eta} \left(\boldsymbol{\sigma}' - \frac{1}{3} \mathrm{Tr}(\boldsymbol{\sigma}') \right) = 2\mu \dot{\boldsymbol{\epsilon}} + \left(K - \frac{2}{3}\mu \right) \mathrm{Tr}(\dot{\boldsymbol{\epsilon}}), \tag{5.28}$$

where μ is the shear modulus, η is the viscosity, and K is the bulk modulus. Equation (5.28) is much simplified by making a Fourier transformation. The correspondence principle states that in the frequency domain the constitutive law for a linear viscoelastic material is of the same form as that of an elastic material in the time domain, where rheological constants are replaced by complex analogues (Biot, 1954). I follow previous works (e.g., Tobie et al., 2005; Roberts and Nimmo, 2008; Beuthe, 2013) in utilising the correspondence principle to calculate the complex (Fourier transformed) stress and strain tensors. The method for the calculation of these is presented below. The stress and strain rate tensors are related to their complex forms by an inverse Fourier transform (Tobie et al., 2005; Beuthe, 2013)

$$\boldsymbol{\sigma}' = \int_0^\infty \tilde{\boldsymbol{\sigma}}(\omega) e^{i\omega t} \delta(\omega - \omega_f) \ \mathrm{d}\omega = \tilde{\boldsymbol{\sigma}}(\omega_f) e^{i\omega_f t}, \tag{5.29}$$

$$\dot{\boldsymbol{\epsilon}} = \frac{\partial}{\partial t} \int_0^\infty \tilde{\boldsymbol{\epsilon}}(\omega) e^{i\omega t} \delta(\omega - \omega_f) \ \mathrm{d}\omega = \frac{\partial}{\partial t} \left(\tilde{\boldsymbol{\epsilon}}(\omega_f) e^{i\omega_f t} \right) = i\omega_f \tilde{\boldsymbol{\epsilon}}(\omega_f) e^{i\omega_f t}, \tag{5.30}$$

where I have assumed that the the body responds only at the orbital forcing frequency ω_f, enforced by the delta function $\delta(\omega - \omega_f)$. Equations (5.29) – (5.30) show that the stress and strain rate tensors are complex; in equation (5.27), the physical solution is just the real part. Substituting equations (5.29) – (5.30) into equation (5.27) we have

$$\begin{aligned} P_\circ &= \frac{1}{T} \int_t^{t+T} (\tilde{\boldsymbol{\sigma}}(\omega_f) e^{i\omega_f t})_{\mathrm{re}} : (i\omega_f \tilde{\boldsymbol{\epsilon}}(\omega_f) e^{i\omega_f t})_{\mathrm{re}}, \\ &= \frac{1}{T} \int_t^{t+T} \frac{1}{4} \left[\tilde{\boldsymbol{\sigma}} : (i\omega_f \tilde{\boldsymbol{\epsilon}}) \ e^{2i\omega_f t} + \tilde{\boldsymbol{\sigma}}^* : (i\omega_f \tilde{\boldsymbol{\epsilon}})^* e^{-2i\omega t} + \tilde{\boldsymbol{\sigma}}^* : (i\omega_f \tilde{\boldsymbol{\epsilon}}) + \tilde{\boldsymbol{\sigma}} : (i\omega \tilde{\boldsymbol{\epsilon}})^* \right] \ \mathrm{d}t, \end{aligned} \tag{5.31}$$

where I note that the real part of a complex vector $\boldsymbol{a} = \tilde{\boldsymbol{a}} \ \exp(i\omega t)$ can be computed as $\boldsymbol{a}_{re} = (\tilde{\boldsymbol{a}} \ \exp(i\omega t) + \tilde{\boldsymbol{a}}^* \exp(-i\omega t))/2$, and * denotes the complex conjugate. Averaging over a full orbital period, all oscillatory terms disappear and we are left with

$$\begin{aligned} P_\circ &= \frac{1}{4} \left[\tilde{\boldsymbol{\sigma}}^* : (i\omega_f \tilde{\boldsymbol{\epsilon}}) + \tilde{\boldsymbol{\sigma}} : (i\omega_f \tilde{\boldsymbol{\epsilon}})^* \right] \\ &= \frac{1}{2} \left[\tilde{\boldsymbol{\sigma}}^* : (i\omega_f \tilde{\boldsymbol{\epsilon}})_{\mathrm{re}} \right] \\ &= \frac{\omega_f}{2} [i(\tilde{\boldsymbol{\sigma}}^* : \tilde{\boldsymbol{\epsilon}})]_{\mathrm{re}}. \end{aligned} \tag{5.32}$$

This is the cycle-averaged power density. Expanding terms we arrive at the expression for cycle-averaged power density, or equivalently volumetric dissipation rate, given by Tobie et al. (2005)

$$P_\circ = \psi = \frac{\omega_f}{2} \left[\mathrm{Im}(\tilde{\sigma}_{ij}) \mathrm{Re}(\tilde{\epsilon}_{ij}) - \mathrm{Re}(\tilde{\sigma}_{ij}) \mathrm{Im}(\tilde{\epsilon}_{ij}) \right], \tag{5.33}$$

where summation over components i and j is implied.

5.B.2 Calculation of complex stress and strain rate tensors

To calculate the dissipation rate ψ with equation (5.6) requires knowledge of the complex stress and strain tensors. To calculate these I follow the methodology of Sabadini and Vermeersen (2004), Roberts and Nimmo (2008) and Beuthe (2013). I detail my implementation here because my notation and the form of my equations combine aspects of each of these works. I calculate dissipation assuming that material parameters are a function of radius only, allowing the problem to be formulated as the product of six radial functions y_i with spherical harmonics (Sabadini and Vermeersen, 2004). The six components of the vector $\boldsymbol{y}$ correspond to the radial and tangential displacements, the radial and tangential stresses, the potential, and the 'potential stress' (Sabadini and Vermeersen, 2004). The vector of solutions $\boldsymbol{y}_l$ at spherical harmonic degree l are the solutions to the system

$$\frac{\partial \boldsymbol{y}_l(r)}{\partial r} = \boldsymbol{A}_l(r)\boldsymbol{y}_l(r), \tag{5.34}$$

where the coefficients of the matrix $\boldsymbol{A}_l$ are given by equation (1.95) in Sabadini and Vermeersen (2004). I solve this system with the propagator matrix approach detailed in Sabadini and Vermeersen (2004), and also well explained in appendix A of Roberts and Nimmo (2008) (though I note that the definitions of y_2 and y_3 are reversed in these two works; I use that of Sabadini and Vermeersen, 2004).

The tidal potential for a synchronous orbit to first degree in eccentricity is given by (Kaula, 1964; Tobie et al., 2005; Roberts and Nimmo, 2008)

$$\Phi = R^2\omega_f^2 e\left[-\frac{3}{2}P_2^0(\cos\,\theta)\cos(\omega_f t) + \frac{1}{4}P_2^2(\cos\,\theta)\left[3\,\cos(\omega_f t)\,\cos(2\phi) + 4\,\sin(\omega_f t)\sin(2\phi)\right]\right], \tag{5.35}$$

where e is the eccentricity, P_l^m is the associated Legendre polynomials at spherical harmonic degree l and order m, θ is colatitude, and ϕ is longitude, which is zero at the sub-Jovian point. The six unique components of the strain tensor are related to the six components of the vector $\boldsymbol{y}$ and derivatives of the tidal potential by (Beuthe, 2013)

$$\begin{aligned}
\epsilon_{rr} &= \frac{\mathrm{d}y_1}{\mathrm{d}r}\Phi, \\
\epsilon_{\theta\theta} &= \frac{y_2}{r}\frac{\partial^2\Phi}{\partial\theta^2} + \frac{y_1}{r}\Phi, \\
\epsilon_{\phi\phi} &= \frac{y_2}{r\ \sin^2\theta}\left[\frac{\partial^2\Phi}{\partial\phi^2} + \cos\theta\ \sin\theta\frac{\partial\Phi}{\partial\theta}\right] + \frac{y_1}{r}\Phi, \\
\epsilon_{r\theta} &= \frac{y_4}{2\mu}\frac{\partial\Phi}{\partial\theta}, \\
\epsilon_{r\phi} &= \frac{y_4}{2\mu\ \sin\theta}\frac{\partial\Phi}{\partial\phi}, \\
\epsilon_{\theta\phi} &= \frac{y_2}{r\ \sin\theta}\left[\frac{\partial^2\Phi}{\partial\theta\partial\phi} - \cot\theta\frac{\partial\Phi}{\partial\phi}\right],
\end{aligned} \tag{5.36}$$

where again I note that my definitions of y_{2-3} follow Sabadini and Vermeersen (2004) and so are interchanged in the equations of Beuthe (2013). The correspondence principle (Biot, 1954) states that constitutive laws for linear viscoelasticity in the frequency domain are the same in form as for elastic materials in the time domain, with the substitution of complex rheological parameters. A Fourier transform of the constitutive Maxwell viscoelasticity equation (5.28) gives (Roberts and Nimmo, 2008)

$$\tilde{\boldsymbol{\sigma}} = 2\tilde{\mu}(\omega)\tilde{\boldsymbol{\epsilon}} + \left[K - \frac{2}{3}\tilde{\mu}(\omega)\right]\mathrm{Tr}(\tilde{\boldsymbol{\epsilon}}). \tag{5.37}$$

where the Maxwell complex shear modulus is given by (Tobie et al., 2005)

$$\tilde{\mu} = \frac{\mu\omega^2\eta^2 + i\mu^2\omega\eta}{\mu^2 + \omega^2\eta^2}. \tag{5.38}$$

Other rheological laws have other forms for the complex shear modulus. Through the solution to the system of equations (5.34), and the relationships in equations (5.36) – (5.37), we can now compute tidal heating as a function of colatitude, longitude, and radius using equation (5.6).

CHAPTER 6

Conclusions

6.1 Thesis summary

The heat transfer processes operating within Io's interior have been known for some time; magmatic segregation exports energy from the partially-molten mantle, and volcanic systems export it through the lithosphere. There has, however, been little work that aims to couple these processes. In this thesis I have presented a suite of one-dimensional models of tidal heating, mantle magmatism, and lithospheric volcanism that move toward a more complete picture of planetary volcanism. I have demonstrated how these different processes combine to determine Io's structural, thermal, and compositional evolution.

In this thesis I have demonstrated that the formation of magmatic intrusions is a fundamental process in Io's evolution, from controlling the thickness of the lithosphere to setting the compositions of erupted products. I have shown how models that couple the near-surface to the deep interior can make specific, quantifiable predictions of surface observations that can directly constrain the deep interior. By providing these links, my models broaden the scope of new observations, allowing them to constrain a wider array of features and processes.

In this chapter I summarise the findings of this thesis, assess the limitations of this work, and outline future avenues of research that build on the work I have presented. Through this process I will provide a broader contextualisation of my thesis work, demonstrating its applicability to a range of planetary problems.

6.1.1 Couped magmatism and volcanism

In Chapter 3 I developed a framework for coupling the rapid, complex processes of volcanic systems to the slowly evolving underlying mantle. This framework enables us to investigate how the heat-pipe system in Io's lithosphere couples to magma generation and flow in its underlying mantle. Tidal heating drives melting in Io's mantle, producing magmas that segregate buoyantly upward. As these magmas approach the impermeable lithosphere, magma overpressure increases and melt accumulates. My framework allows this high pressure magma to transfer into a volcanic system, which enables its continued rise. As this magma rises through the volcanic system, some of it freezes within the lithosphere, forming magmatic intrusions that deliver mass and energy to the surroundings. The rest of the magma rises to the surface and erupts, imparting a downward flux of solid back down into the interior. By allowing the lithosphere–mantle boundary to evolve dynamically, I showed that the eruption and burial process is extremely efficient at advecting the cold surface temperature down into the interior. In the absence of a heating process within the lithosphere, heat-piping predicts the formation of a > 600 km thick lithosphere.

The formation of magmatic intrusions delivers a significant amount of energy to Io's lithosphere. As buried lavas descend, they are heated by intrusions, counteracting the downward advection of the cold surface temperature. This balance between cold downwelling material and intrusive heating controls Io's lithospheric thickness, resulting in thicknesses in agreement with observations. I contextualised this with an analytical global heat balance. The proportion of magma generated within Io's mantle that freezes intrusively within the lithosphere is given by

$$\text{Intrusive fraction} = \frac{C(T_m - T_s)}{L + C(T_m - T_s)}, \tag{6.1}$$

where C is the specific heat capacity, L is the latent heat, T_m is the temperature of erupting lava, and T_s is the surface temperature. For Io, equation (6.1) predicts that about 80% of magma generated forms lithospheric intrusions.

In Chapter 3 I also showed that the distribution of intrusive heating, not just its rate, is important in explaining observations of Io. Io hosts some of the Solar System's highest mountains, with the highest reaching over 17 km. To support such high mountains, Io's lithosphere must be very strong. I showed that if intrusions form predominantly in the lower lithosphere, the upper lithosphere is cold and thus capable of supporting large mountains. This lead me to propose that significant intrusive magmatism is taking place in Io's lower lithosphere, but that little is taking place in the upper lithosphere.

Modelling the coupled evolution of the lithosphere and underlying mantle also illuminated aspects of the lithosphere–mantle boundary. As solid lithosphere downwells into the mantle, high magma pressure forces the solid to rapidly decompact, leading to the production of a high melt fraction region beneath the lithosphere. The melt fractions reached in this layer are a function of material parameters and the magma pressure below the boundary. If high magma pressures are required for magma to migrate into the lithosphere, or if the shear or magma viscosity is high, high porosities can form. A decompacting boundary layer provides another potential explanation for observations of a high melt fraction layer within Io (Khurana et al., 2011).

More broadly, the work presented in Chapter 3 provides a framework for linking deep interior processes to the surface and near surface of volcanic worlds. By providing such direct links, this model and subsequent ones constructed in the same manner broaden the scope of new surface observations by allowing them to potentially inform on deep interior processes. Such an approach is valuable in the field of planetary science where geophysical measurements that directly constrain the deep interior are sparse if they exist at all.

6.1.2 Compositional evolution

A key way in which we may aim to relate surface observations of volcanic worlds to internal magmatic processes is through the compositions of erupted products. In Chapter 4 I expanded my model to incorporate a simple compositional system to investigate the effects of magmatic segregation and volcanism on compositional evolution. I employed a binary phase diagram consisting of a fusible (low-melting-point) and a refractory (high-melting-point) component. As melting progresses, the fusible component melts and is extracted toward the near surface by magmatic segregation. This produces a near surface that is increasingly enriched in the fusible component, and leaves behind an increasingly refractory lower mantle. Ultimately a steady state is reached where the lower mantle is composed purely of the refractory component, and the near surface is fusible. Magmatic segregation and volcanism provides a pathway for fusible material to migrate upward, but the burial of erupta cannot return it to the lower mantle; this results in a stratification of the mantle.

Above the pure-refractory, lowermost mantle, a transitional region forms where material is heated from the melting point of the fusible component to that of the refractory component as it downwells out of the upper mantle. In this region, tidal dissipation predominantly acts to raise the temperature of downwelling material and so the melting rate is low. This low melting rate, and the resulting low melt fraction and permeability means that this layer acts as an impermeable barrier to hot, refractory magmas formed in the lowermost mantle. This causes melt to accumulate in the lower mantle, and in Chapter 4 I proposed that this melt must be able to leave the lower mantle in order to facilitate heat loss. In my model I allow this accumulating melt to enter a volcanic system to enable its continued ascent. I showed that Io's evolution depends strongly on the fate of this rising, refractory magma.

If refractory magmas that form in the lower mantle freeze quickly after rising into the cooler, fusible upper mantle, Io's mantle becomes stratified. In this case, the upper mantle and lithosphere are formed purely of fusible material. If, however, rising refractory magma can rise all the way to the surface and erupt, the upper mantle will have more intermediate compositions as refractory material is cycled throughout silicate Io. In Chapter 4 I proposed that Io is more likely to be in this second mode, with the eruptions of hot, refractory material from the lower mantle providing an explanation for Io's highest temperature eruptions.

In Chapter 4 I also provided plots that demonstrated how observations of the average compositions and temperatures of surface erupta could be used to constrain Io's bulk composition, as well as evaluating the extent to which its mantle has segregated. Naturally this work is but an initial step into the complex world of coupling igneous petrology and geodynamics, and it has a number of limitations (that I discuss below). It does, however, provide a framework upon which to base more detailed models that closer tie surface melts to the interior processes that form and transport them.

6.1.3 Spatially variable tidal heating

It is important to remember that whilst aspects of Io's structure and evolution can be investigated with idealised, spherically-symmetric models, more detailed models are required to interpret increasingly high-fidelity observations. These improving observations not only require increasingly detailed one-dimensional models, but also two- and three-dimensional models that aim to describe the real, three-dimensional Io. An initial step in this direction is to asses the effects of its primary, non-spherically-symmetric tidal forcing. In Chapter 5 I coupled a three-dimensional tidal heating model to a suite of one-dimensional column models containing physics similar to that presented in Chapter 3, with the aim of understanding how tidal heating can impart non-spherically symmetric (but long-wavelength) structure to Io. I investigated two configurations for the tidal heating model; the first couples tidal heating to porosity and temperature, calculated using the simplified magmatism and volcanism model presented in Appendix 3.B. It predicts high levels of heating in the lower mantle, with high polar heat fluxes. The second includes a dissipative layer beneath the lithosphere — following from a number of previous works that hypothesise the presence of such a layer (e.g., Kirchoff et al., 2011; Hamilton et al., 2013; Rathbun et al., 2018; Cantrall et al., 2018) — that produces a dissipation structure with high equatorial heat fluxes. I showed how non-uniform tidal heating affects magmatic segregation in the interior. High radially integrated heating rates lead to higher melt fractions in the interior, higher eruption rates, and high surface heat fluxes.

The effect of spatially variable tidal heating on lithospheric thickness depends on how intrusions form within the lithosphere. If intrusions form at a constant rate irrespective of the magma flux (and by extension the heating rate), my model predicts the lithosphere to be thickest where radially integrated heating rate is highest. In these regions there is an increased eruption flux, which increases the downward advection of the cold surface material without a corresponding increase in emplacement rate; this leads to a thickening of the lithosphere. Alternatively, if magmatic intrusions form at a rate proportional to the magma flux through the volcanic system, increased emplacement balances the increased advection of the cold surface, resulting in an almost uniform lithosphere thickness. By whatever mechanism magmatic intrusions form, there appears to be a close relationship between the mechanism of their emplacement and the lithospheric thickness.

Each of the proposed emplacement mechanisms have plausible physical interpretations. A constant rate of emplacement may be expected if magma rises through pre-existing conduits. In such a case, an increased heating rate may increase magma flux through these conduits without increasing the total number of conduits; if the contact area with the cold host rock remains almost constant, it is plausible that emplacement rate doesn't increase with volcanic flux. Alternatively, intrusions may form at a rate proportional to magma flux if volcanic conduits form by basal magma pressure. In this case a high heating rate will produce more magma, which creates more volcanic conduits, increasing contact area with the host rock. With a higher contact area with the host rock, emplacement rate would be expected to increase. For each of these possibilities I derived analytical expressions for the lithospheric thickness l, which can be approximated as

$$\text{Constant emplacement rate} \qquad l \approx \frac{C(T_m - T_s)}{L}\frac{q_e}{\lambda_c} \tag{6.2}$$

$$\text{Flux dependant emplacement rate} \qquad l \approx \frac{C(T_m - T_s)}{L}\frac{1}{\lambda_q} \tag{6.3}$$

where q_e is the eruption rate, and λ_c and λ_q are constants that describe the rate of emplacement in each of the two systems. The prediction of absolute lithospheric thicknesses clearly requires a knowledge of the largely unconstrained constants λ_c and λ_q. The present usefulness of these equations lies primarily in their predictions of lithospheric thickness variations, but their applicability could be expanded if λ_c and λ_q can be related to physical processes in the lithosphere.

In Chapter 5 I used a simple isostatic balance to relate long-wavelength lithospheric thickness variations to topography. Assuming that Io doesn't have a petrologically distinct, low density crust (see Chapter 4), I predict that thick lithosphere sits in topographic lows because of its high density. This relates a readily observable feature in topography to a much harder to observe feature in lithospheric thickness. Improved observations, in particular in the polar regions, will enable these competing models to be tested, but a full examination would likely require an orbiter that can make independent estimates of the lithosphere thickness, perhaps from multi-frequency magnetic sounding (Keane et al., 2020).

Previously, attempts to relate surface observations to interior dissipation structure have focussed on volcanic activity (Ross et al., 1990; Kirchoff et al., 2020; Hamilton et al., 2013; Rathbun et al., 2018; Cantrall et al., 2018). We have been observing Io in some capacity for over 40 years now, but even so we cannot be sure that our observations of volcanic activity are representative of either long-timescale activity nor the underlying dissipation structure. The primary advantage of the work presented in Chapter 5 is that lithospheric thickness and topography are expected to vary on much longer timescales. I propose that long-wavelength lithospheric thickness variations and topography provide a more robust means of interpreting Io's interior dissipation structure.

6.2 Limitations and assumptions

The work in this thesis represents a novel way of investigating planetary volcanism. Whilst built upon a large amount of previous work in the fields of planetary science and two-phase fluid dynamics, the combined approach employed here is new to planetary research. This fact has, naturally, led me to employ a large number of assumptions and simplifications. In this section I discuss some of these and the resultant limitations that they introduce.

- Many of my results assume that Io is in a thermal steady state, based on the apparent match between the orbitally derived heating rate (from equation (2.1)) and the surface heat flux (Lainey et al., 2009). It is important to note, however, that there are a number of assumption that go into using equation (2.1), and that even if the heating rate matches the surface heat flux, the heating rate may, for example, be changing over time. Whilst my models do no require constant or steady state heating rates, my investigations and results have focussed on this being the case. The assumption of thermal steady state has been used to set the heating rate, either directly (in Chapters 3 and 4), or through the choice of parameters (in Chapter 5). If Io is not in a thermal steady state, the rate of heat production in the interior may be different to what has been employed in this model, or may be changing over time. The assumption of thermal steady state is also the basis for assuming that convective heat transport is at most a secondary process in transporting tidal heat. The arguments of Moore (2003) on which this assumption is built are weakened if Io is not in a thermal equilibrium.

- All of the dynamic models presented in this thesis are one-dimensional; they only allow radial flows. This precludes an investigation of convection in Io's interior. In the two-component model of Chapter 4, there is thermal drive for convection, as well as a plausible chemical drive (see below). My one-dimensional models cannot be used to investigate the character or consequences of any such convective motion. Further, lateral flow may be expected in the melt phase specifically, not just the solid or bulk two-phase system. Io's volcanoes are discrete features on its surface, so even if magma flow in the mantle is dominantly radial, lateral flow must be facilitating a transfer to a discrete set of volcanoes. Extraction of magma from the mantle is likely to be discrete, and this will have significant consequences for compaction pressure distributions in the upper mantle, and may control magma distribution beneath the lithosphere. My one-dimensional models are not able to investigate any such lateral magma flows, nor the consequences of discrete magma extraction.

- My parametrisation of the volcanic plumbing systems consider a long-timescale average of these systems. This means that care must be taken when comparing my model outputs to observations, which inevitably capture short-timescale processes. Caldera-like features have been observed on Io (Radebaugh et al., 2001), implying that magma does stall in the near surface on at least short timescales. On short, observational timescales, conductive heat loss through the lids of such features may imply a steep geothermal gradient, even though the main process that has exported this material from the mantle is advection through volcanic systems.

- My one-dimensional models assume that Io resurfaces uniformly on long timescales. Io's volcanoes are discrete and look remarkably fixed. Indeed Io's most eruptive feature, Loki, is an overturning lava lake that does not seem to significantly resurface the surroundings away from the lake (de Kleer et al., 2017). Much of the Io literature implicitly assumes either that the distribution of surface activity changes over time to allow uniform resurfacing, or that extensive flow-volcanism resurfaces areas distal to volcanoes. I inherit this assumption, and because of my long-timescale averaging of the volcanic systems, my models cannot investigate how Io's short-timescale volcanism leads to long-timescale resurfacing.

- In my models I have neglected the pressure dependence of melting temperature. Io's small size means that changes in melting temperature with depth are expected to be much smaller than on Earth, but nonetheless it may still have important effects. The high heating rate is expected to put the whole mantle onto the solidus, this would then manifest as an increase in temperature with depth. This temperature increase will reduce density, and if this is not balanced by the pressure dependence of density, it will provide a thermal drive for convection.
- The compositional model used in Chapter 4 is greatly simplified compared to real petrological systems. Io's lavas will reflect complex processes such as partial melting, magma mixing, and magma transport in a multi-chemical-component system. This complicates the process of making direct comparisons between the predictions of Chapter 4 and surface observations.
- My parametrisation of the volcanic system in the two-component model of Chapter 4 does not allow for magma compositions to evolve within the lithosphere. As magma traverses the thick lithosphere, it is likely that refractory phases are precipitated, producing cooler and more evolved magmas than those that entered the volcanic systems at their base. This means that if refractory lavas are not seen on Io's surface, it would not necessarily imply that refractory magmas do not migrate out of the deep interior.
- The petrological model in Chapter 4 does not consider the different densities of the two end-member compositions. At the pressures relevant to Io, Fe is expected to partition preferentially into the melt, and so in the context of Chapter 4, we would expect Fe to

become enriched in the near surface. This will increase the density of material in the near surface and may provide a drive for compositional convection (see below).

- There are a number of other assumptions in the petrological model of Chapter 4 that a more detailed model may aim to avoid. The different latent heats of refractory and fusible materials will have consequences for melting behaviour and the global heat balances I have presented. In theory, an accurate knowledge of long-timescale eruptive and conductive heat fluxes as well as the eruption rate could be used to constrain the compositions of erupta by constraining the latent heat.
- The tidal heating calculation in Chapter 5 is not formally three-dimensional. The methodology employed calculates a three-dimensional heating distribution from a spherically symmetric interior structure. This means that when iterating back from the dynamic model to the tidal heating model, the three-dimensional structure must be averaged over spherical shells. This limitation is not unique to this work, and is a feature common to a large number of works on tidal dissipation (e.g., Segatz et al., 1988; Moore, 2003; Bierson and Nimmo, 2016; Renaud and Henning, 2018).
- In Chapter 5 I use a Maxwell viscoelastic model despite its well documented failings when employed in tidal heating calculations. In order to produce heating rates in agreement with the observed surface heat flux requires extremely low mantle shear viscosities on the timescales of tidal deformation. In this work I am assuming that using a Maxwell constitutive law with a low shear viscosity produces the same heating distribution as the true (unknown) rheological law. This will not be the case if, for example, the true response results in greatly amplified dissipation in a high porosity layer. It is this possibility, as well as its presence in other works, that motivated my inclusion of the asthenosphere dissipation model. Other works have investigated an Andrade rheology as an alternative that produces high rates of dissipation because the mantle shear viscosity is low at tidal frequencies (e.g., Bierson and Nimmo, 2016;

Renaud and Henning, 2018). Such empirical models present their own issues, being heavily dependent on a number of poorly constrained rheological parameters. Linking deformation to dissipation through a rigorous and physically defined rheological law is a significant outstanding problem in both material science and planetary science.

This list covers a number of limitations from major to relatively minor, and with different levels of tractability. In the next section I will draw from some of the more interesting and tractable limitations to propose future directions for work that can continue to develop our understanding of planetary volcanism.

6.3 Future work

The models presented in this thesis initiate a new, more complete way of investigating planetary volcanism by coupling magmatism in the deep interior to volcanism in the lithosphere. There are a number of ways that this approach could be extended, as well as various other planetary bodies at which a form of this approach could be directed. In this section I set out recommended avenues for future research that directly build on the work presented in this thesis.

6.3.1 Io as a three-dimensional body

We can observe how magmatism facilitates heat loss from Io's surface, but a lack of understanding of how magma flows in the interior makes relating this to interior processes like tidal heating difficult. The models presented in this thesis focussed on purely radial flows, and other, higher-dimensional works have not directly modelled magma flow (e.g., Tackley, 2001; Tackley et al., 2001; Steinke et al., 2020). A two-dimensional model that investigates magma flow in the mantle and lithosphere together would provide a more realistic picture that could be rigorously compared to increasingly high-fidelity observations. Lateral magma flow in the mantle will drive the transition from deep, radial magmatic segregation (such as that discussed in this thesis) to the three-dimensional near-surface we observe. The complex details of how magma flows in partially molten mantles are as yet, however, largely unknown.

This decade is poised to provide unparalleled insight into planetary volcanism with the flight of the *JUpiter ICy moons Explorer* (*JUICE*), *Europa Clipper*, and the selection of two out of four NASA Discovery mission candidates targeting Venus, Triton, and Io. With the upcoming wealth of new observations of volcanic worlds, there is a need for a campaign to provide robust bridges between interior structure and specific, observable surface features. The first phase of this campaign has been detailed in this thesis, by relating global, leading-order structure to observations. The next phase is to develop two- and three-dimensional models of planetary volcanism that make specific, quantifiable predictions of spatially-variable surface observations.

My framework for coupling mantle magmatism to volcanic systems can be expanded initially into two dimensions. The model presented in Chapter 3 can be written in a two-dimensional finite volume representation with relatively few changes. Perhaps the simplest initial implementation would be to use the model derived in Chapter 3 and investigate whether the system is stable or unstable to two-dimensional perturbations. If spherical symmetry is indeed lost, the primary complexity becomes how magma is extracted to the volcanic systems. One approach that enforces a loss of spherically symmetry is to allow extraction only at a series of discrete regions of high magma overpressure (figure 6.1). The locations in the mantle where high overpressure is generated would then control where volcanoes form at the surface. It is likely that the compaction length would exert a leading-order control on the spacing of volcanoes by preventing the generation of high magma overpressure in the vicinity of already-active regions of extraction. This hypothesis would explain the statistically uniform spacing of Io's volcanoes, which suggests that volcanoes may be distributed such as to evenly share magma supply (Hamilton et al., 2013).

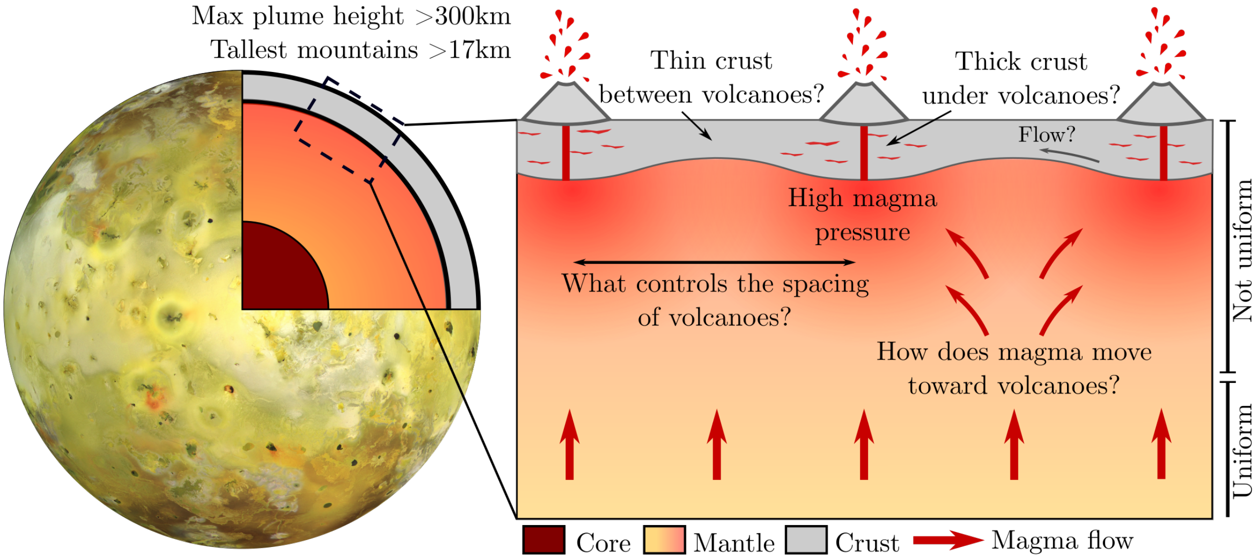

Figure 6.1: Schematic showing how a two-dimensional model for magmatism and volcanism on Io may be constructed, and some of the features it would investigate.

A new framework for the emplacement of magma within the lithosphere and on the surface would need to be developed in a two-dimensional extension to my models. As indicated in figure 6.1, local resurfacing would be expected to thicken the lithosphere around active volcanoes, but between volcanoes where there is little or no resurfacing the lithosphere would thin by conduction. It is possible that a steady state emerges where lateral solid-state flow in the lithosphere maintains a constant thickness, or that the intrusive emplacement of magma balances the thickening caused by eruptions. It is also possible, however, that no such steady state emerges. In this case it may be that a given configuration of volcanoes is not stable on long timescales, or that by some process, regions far from volcanoes can be resurfaced at a comparable rate to proximal regions.

A two-dimensional model would also allow an investigation into the propensity for convection in Io. This could initially be done by including a pressure dependent solidus and a solid density that is a function of temperature and pressure. It is, however, unlikely that the small changes in solidus temperature expected for the low pressures of Io (< 8 GPa) would provide a significant drive for thermal convection, given the high heating rate and magmatic segregation. The inclusion of this possibility would, however, provide a useful framework for investigating convection in two-chemical component system.

In Chapter 4 I noted that if Fe becomes concentrated in the fusible component, it may lead to an unstable density stratification. This compositional stratification, together with the thermal stratification may be expected to drive thermochemical convection. By allowing the density of both the solid and liquid to be a function of temperature and composition, the propensity for such a convective mode could be investigated. There are a number of plausible outcomes for such a model: convection may completely remove the mantle stratification described in Chapter 4, convection may produce a mixed layer between a fusible upper mantle and a refractory lower mantle, or dense Fe may be mobilised to the base of the mantle and removed from the system. A two-dimensional model would be able to address this, as well as tackling the rich mathematical problem of coupled magmatic segregation and two-phase convection.

It is also important to note that the distribution of volcanoes on Io is three-dimensional, not two-dimensional. A two-dimensional model would provide a mathematical idealisation that bridges the gap between a one-dimensional model and the true, three-dimensional system, but relating such a model to the actual surface is not necessarily straightforward. The tidal forcing is three-dimensional, and so the flows and structures that it produces will also be. A full understanding of Io as a three-dimensional body will ultimately require fully three-dimensional models.

6.3.2 A more detailed petrological model

To rigorously compare model predictions of Io's erupta to observations requires both to be defined at a similar level of fidelity. The two-component system described in Chapter 4 of this thesis was designed to be testable against observations of 'high' and 'low' temperature eruptions, or 'refractory' and 'fusible' erupta; the coarse detail of this basic system will be quickly eclipsed by improving observational fidelity. There are two clear possibilities for the next level of detail to be added to the model system. The first is to expand the two-component system to a three component phase diagram for SiO_2–MgO–FeO, and the second is to include a consideration of sulphur. In this section I discuss an extension to a three-component system of SiO_2–MgO–FeO; an incorporation of sulphur will be discussed in the subsequent section.

One approach to constructing a more detailed compositional system is through ideal solution theory. Ideal solution theory assumes thermodynamic equilibrium and uses this, together with definitions of partition coefficients, to evaluate a chemical assemblage from the local bulk composition and energy content. In this way the approach is similar to that which I employed in Chapter 4. In practice, the partition coefficients are often chosen to produce an expected phase diagram. Indeed as the components considered are often 'hypothetical' (in the same sense as my refractory and fusible components in Chapter 4), a rigorous calibration of partition coefficients is often not possible. Ideal solution theory is applied in a two-component system by Rudge et al. (2011), where a means for chemical disequilibrium is included, and is applied to three- and four-component systems by Keller and Katz (2016).

An alternative and perhaps more direct approach would be to simply fit surfaces to the solidii and liquidii of a desired N-component phase diagram. This approach yields analytical expressions for solidii and liquidii, but a root finding method is generally still required to find phase compositions within the enthalpy method. There is very little difference between this approach and ideal solution theory, and if the intention was to fit a desired phase diagram, the choice would likely come down to a preference between fitting solidus surfaces or tuning partition coefficients.

As stated in Chapter 4, the broad behaviour of the model as written would not be expected to change significantly by the incorporation of a more detailed phase diagram; a layered structure with increasingly refractory material with depth would be anticipated. Any part of the phase diagram that has a steep solidus would be expected to manifest as a region of low melt fraction, and would act as a barrier to melts rising from below. The true advantages of incorporating a more detailed phase diagram would be revealed by a simultaneous expansion to two-dimensions. In such a system the partitioning of dense, Fe-rich material may lead to thermochemical convection.

Finally a word can be said on the lessons that have been learned from the chemical geodynamic modelling of Chapter 4, which illuminated some useful numerical considerations that can be transferred to an N-component models if a time-evolving solution is sought:

- The phase diagram should be smooth. This point was illustrated in figure 4.2 where a smoothed form of a discontinuous solidus was presented. The required smoothness can be reduced under grid refinement, but can actually have relatively little effect on the solution, particularly at steady state.
- Artificial compositional diffusion may be required. In Appendix 4.B I noted that convergence of my numerics required a degree of compositional diffusion. It is of course possible that a different numerical method will not require this.
- The energy-composition system can fail to converge when solved alongside other significant non-linearities, such as the porosity dependence in Darcy's law. This is particularly the case when the solidus is steep and so compositions are changing rapidly. To avoid this problem I found it most effective to separate the energy-composition system from the momentum equation; I split my system into three sub-systems with their own non-linear solvers, and iterated between the solvers. See Appendix 4.B for details on my numerical implementation.

6.3.3 Sulphur cycling

The framework for coupled mantle magmatism and lithospheric volcanism that I have developed in this thesis could be turned to an investigation of Io's sulphur cycle. A fundamental aspect of planetary dynamics and habitability is the cycling of volatile elements through the solid interior (McGovern and Schubert, 1989; Dasgupta and Hirschmann, 2010; Kagoshima et al., 2015; Mallik et al., 2018; Hirschmann, 2018). As outlined in Chapter 1, chemical observations of Io's global volcanic system indicate that sulphur is the abundant volatile species and arrives at the surface through volcanic eruptions (Williams et al., 2011); this leads to a key question. What are the physical and chemical pathways by which sulphur is cycled through Io's interior? Further, how does the abundance and speciation of sulphur affect Io's interior dynamics and evolution? The pathways that transport sulphur will control the abundance and speciation of sulphur on Io's surface. Predictive models of sulphur cycling can therefore be tested against observations of Io's surface. This would help to illuminate the role that volatile cycling plays in the evolution of terrestrial planet interiors.

The petrological behaviour of sulphur is controlled by the oxidation state of Io's mantle, which is thus of crucial importance in understanding Io's sulphur cycle. Analysis of Io's volcanic plumes indicate a relatively oxidised plume source for its largest volcano, Loki (an overturning lava lake), between the Ni–NiO and hematite–magnetite buffers, whilst Pele (a lava lake with plume eruptions) has a plume source below the Ni–NiO buffer (Zolotov and Fegley, 1999). In the region of the Ni–NiO buffer, sulphide stability changes rapidly (Baker and Moretti, 2011). Below the Ni–NiO buffer, S^{2-} is the stable form of sulphur and, unless there is very little Fe present, virtually all sulphur forms FeS. Above the Ni–NiO buffer however, SO_4^{2-} is the stable form of sulphur, resulting in the formation of sulphates such as $CaSO_4$. The precise nature of this transition depends on temperature, pressure, and composition (Moretti and Baker, 2008), and most experiments on this transition have been conducted on hydrous rhyolitic melts (Baker and Moretti, 2011). Therefore, for the mafic and virtually anhydrous Io, an a priori assumption cannot be made as to whether sulphur is stable as sulphide or sulphate, and so both possibilities should be investigated.

The dynamics of mantle magmatism and lithospheric volcanism could have significant effects on the physical pathways by which sulphur is cycled in Io's interior. How sulphur interacts with this system depends on the liquid phase that carries the sulphur (i.e., an immiscible sulphide melt or the silicate melt), which is sensitive to the oxygen fugacity. It may also depend on the thermal and flow structure of the lithosphere and underlying mantle. If, the lower lithosphere is hot, as has been proposed in this thesis, this region could potentially remobilise downwelling, low-melting-point, sulphur rich material. Magmatic intrusions could also provide an opportunity for the segregation of high-density magma components. There is clearly a rich vein of geochemistry and geodynamics that could be investigated in a project such as this.

6.3.4 Applications to other bodies

Io is a unique body in the Solar System, but the physics that describe its evolution have wide-ranging applications to other bodies in the Solar System and beyond. Potential targets for the kind of modelling presented in this thesis include Venus and the early Earth, both of which are thought to have operated in a heat-pipe regime at some point in their history (Moore and Webb, 2013; Moore et al., 2017). Tidally heated exoplanets are also potential targets, such as those in the TRAPPIST-1 system, which are expected to be geologically active (Barr et al., 2018). Beyond silicate bodies, my models are also applicable to volcanic ice-moons such a Europa and Enceladus, where the physics of water–ice systems is similar to that of partially molten silicates, with the crucial difference being the densities of the phases. In these final few paragraphs I will describe how my models could be adapted for new targets, expanding the applicability of my approach to modelling planetary volcanism.

6.3.4.1 Venus and the early Earth

Present-day Earth, Venus, and Io operate in very different tectonic regimes. Earth and Venus both have convecting interiors but are both expected to have been much hotter in

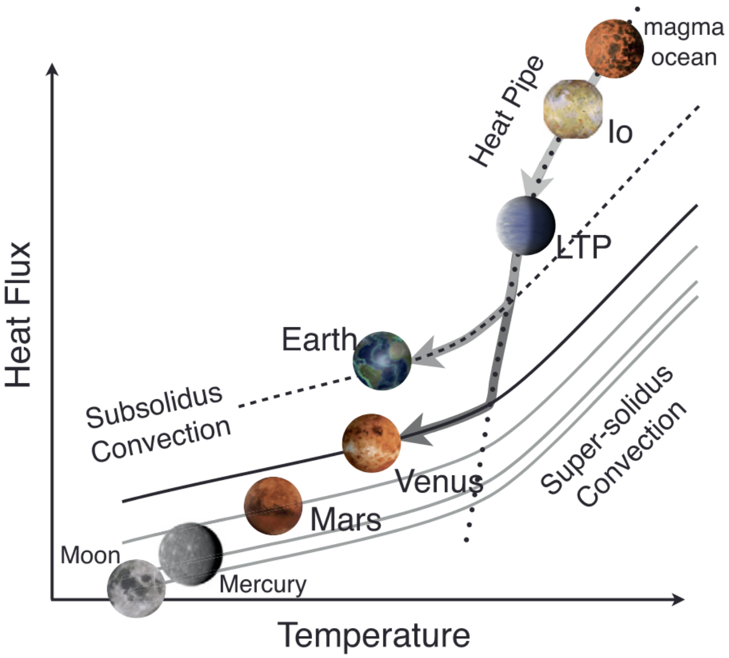

Figure 6.2: Illustration of planetary heat-flux against internal temperature, showing different heat-transfer regimes, reproduced from Moore et al. (2017). Initially hot bodies evolve to lower temperatures and heat fluxes, and convecting bodies like Earth and Venus may have evolved out of heat-pipe regimes. LTP stands for Large Terrestrial (exo)Planet, where an initial magma ocean stage is indicated as distinct from smaller bodies like Io.

the past (figure 6.2). In their early histories, both transitioned out of a magma ocean state into a partially-molten state with volcanic activity presumably not dissimilar to present day Io. The current states of both Earth and Venus are closely related to their atmospheres, which developed in their early, highly volcanic histories. Whilst a lot of research has been dedicated to understanding outgassing from a magma ocean (e.g., Carlson et al., 2014; Pahlevan and Stevenson, 2007; Rubie et al., 2016; Lammer et al., 2018), relatively little work has investigated interactions between the interior and atmosphere in a heat-pipe regime.

A highly volcanic period — and its more general role as a transitional stage between a magma ocean and solid-state convection — has significant implication for volatile cycling and atmospheric evolution. Most outgassing from the interiors of Earth and Venus occurred in the magma-ocean state, but we know that outgassing from the magma ocean was not complete due to the abundance of primordial volatiles such as ^{3}He in present day ocean island basalts

(Kurz et al., 1982). The divergent evolutions of Earth and Venus likely emerged at this early stage of transition from magma ocean to solid-state convection (Hamano et al., 2013), and an investigation into volatile cycling at this juncture could illuminate this divergence.

The incorporation of volatile species into the chemical systems presented in this thesis could be approached from a trace-element perspective, where the species are assumed to have no impact on melting behaviour, or by considering a three-component system of dunite, basalt, and hydrous basalt such as in Keller and Katz (2016). This compositional system would then be modelled together with a representation of the atmosphere, which could be done by treating the atmosphere as a box model, in which only mass exchanges at the planetary surface are considered. Such a system would enhance our understanding of how the interiors and atmosphere of highly volcanic bodies evolve, and could help to answer outstanding questions such as how much water Earth and Venus have lost, and how the presence or absence of water controls the evolution from magma ocean to solid-state convection (Hamano et al., 2013).

6.3.4.2 Tidally-heated exoplanets

Another potential suite of targets for the models developed in this thesis are tidally-heated exoplanets. In the last decade our capacity for observing exoplanets has exploded, and all signs indicate that this trend will continue as spectroscopic methods improve, allowing us to better characterise exoplanetary compositions, atmospheres, and geological activity. An emerging class of exoplanets are the tidally-heated exoplanets such as those in the TRAPPIST-1 system (Barr et al., 2018). These bodies are thought to be highly volcanically active with melting driven by tidal heating — in many ways they are thought to be similar to present day Io. In such a case, Io serves as our ‘exoplanet next door’, and models for its evolution can be directly applied to such exoplanets in an attempt to understand improving observations.

Another interesting and related class of exoplanets are those thought to host surface magma oceans. Exoplanets such as the super-Earth 55 Cancri e have small enough semi-major axes that the side facing their star is thought to be kept molten by solar insolation (Hammond and Pierrehumbert, 2017). This presents an interesting, alien system where the primary planetary heat source is external. To what depth would a magma ocean be expected? How would it interact with the planet's 'dark-side', which likely does not have a surface magma ocean? The dynamics of such a planet will be very different to Io, but the physics of melting will be similar and could be approach with the same general formulations as presented in this thesis.

6.3.4.3 Al-26 heated planetesimals

A closer-to-home suite of targets for the models I have developed are Al-26 heated planetesimals. Aluminium-26 is a short-lived radioactive isotope that is thought to have caused extensive melting in the Solar System's earliest forming planetesimals, allowing them to differentiate. The cooling history of these bodies are recorded by the achondrite meteorites. Their thermal evolution is a competition between heating by Al-26 decay and secular cooling, which is rapid because of the small size of these bodies. Lichtenberg et al. (2019) showed that parameters like the mantle grain size (and, by extension, the permeability) affect the mobility of magmas that form, which in turn affects the thermal evolution. The magma generation and flows in these bodies are very similar to those in the models I have presented in this thesis.

A key difference between the evolution of Al-26 heated planetesimals and that of Io is that the distribution of heating evolves as compositional structure evolves. Aluminium has different chemical affinities in different melts, resulting in its partitioning during evolution. An aspect of this that has not been investigated is its transport in volcanic systems. If magmas enter into a volcanic system, they could transport Al-26 upward into the cooling lid, providing a source of heat that keeps the near-surface hotter for longer. Such a transport would have significant implications for the cooling histories and melt distributions in these bodies, and may even be observable in the meteorite record.

Adapting the compositional model in this thesis for application to Al-26 heated planetesimals would require two primary changes. The first is the derivation of a relevant compositional systems that tracks the partitioning of aluminium during melting. Lichtenberg et al. (2019) achieved this by using an olivine–pyroxine–feldspar system and assuming that aluminium partitions into the feldspar. The second requirement is changing the heat-production term in the enthalpy equation to being determined by the local Al-26 content as well as the time (because of the rapid decay of Al-26). Finally, it is important to remember that these planetesimals are far smaller than Io. This means that they have much lower gravity, significantly reducing the drive for magmatic segregation. Despite these considerations, this avenue is probably the simplest application of my models to another type of planetary body.

6.3.4.4 Icy moons

The final potential targets for my models that I will discuss are the icy moons of the Solar System. Bodies such as Enceladus and Europa receive high levels of interest due to their potentially habitable sub-surface oceans. The obvious difference between partial melting of an icy moon as compared to a silicate body is that the melt generated is more dense than the solid residuum, and so under gravity it migrates downward. This explains the stability of a sub-surface ocean on these bodies; the density stratification of a water ocean underlying an icy shell is stable. A number of previous works have investigated the onset of convection in icy shells (e.g., Barr and McKinnon, 2007; Allu Peddinti and McNamara, 2019), and a smaller number of more recent works have investigated two-phase flow in ice shells (e.g., Kalousová et al., 2014; Hammond et al., 2018). Little work, however, has investigated the coupling of convection and melt segregation in the ice shells of icy satellites. The melt segregation modelling presented in this thesis could be developed into a two-dimensional model of an ice shell model that investigates both convection and two-phase flow by using a full Stokes-Darcy formulation.

A model for ice shell evolution could be expanded along similar lines to the work presented in this thesis. An important aspect of icy moon evolution is in the distribution of salts, which can significantly alter melting points and affect melting dynamics. Similar to in terrestrial ice sheets, as the ice-shell freezes, salts are rejected downward. The increasing salinity of these waters results in gravity drainage and compositional convection in the pore-space, which ultimately controls the distribution of salts and impurities (Buffo et al., 2020). The types of two-phase flow model presented by Hammond et al. (2018) and Buffo et al. (2020) could be combined with cryovolcanism models (e.g., Manga and Wang, 2007; Quick and Marsh, 2016) in a framework similar to that proposed in this thesis to provide a more complete model for the dynamics of planetary ice shells.

Bibliography

Allu Peddinti, D. and McNamara, A. K. (2019). Dynamical investigation of a thickening ice-shell: Implications for the icy moon Europa. *Icarus*, 329:251–269.

Baker, D. R. and Moretti, R. (2011). Modeling the Solubility of Sulfur in Magmas: A 50-Year Old Geochemical Challenge. *Reviews in Mineralogy and Geochemistry*, 73(1):167–213.

Balay, S., Abhyankar, S., Adams, M. F., Brown, J., Brune, P., Buschelman, K., Dalcin, L., Dener, A., Eijkhout, V., Gropp, W. D., Karpeyev, D., Kaushik, D., Knepley, M. G., May, D. A., McInnes, L. C., Mills, R. T., Munson, T., Rupp, K., Sanan, P., Smith, B. F., Zampini, S., Zhang, H., and Zhang, H. (2020). PETSc users manual. Technical Report ANL-95/11 - Revision 3.13, Argonne National Laboratory.

Balay, S., Abhyankar, S., Adams, M. F., Brown, J., Brune, P., Buschelman, K., Dalcin, L., Dener, A., Eijkhout, V., Gropp, W. D., Karpeyev, D., Kaushik, D., Knepley, M. G., May, D. A., McInnes, L. C., Mills, R. T., Munson, T., Rupp, K., Sanan, P., Smith, B. F., Zampini, S., Zhang, H., and Zhang, H. (2019). PETSc web page. https://www.mcs.anl.gov/petsc.

Balay, S., Gropp, W. D., McInnes, L. C., and Smith, B. F. (1997). Efficient management of parallelism in object oriented numerical software libraries. In Arge, E., Bruaset, A. M., and Langtangen, H. P., editors, *Modern Software Tools in Scientific Computing*, pages 163–202. Birkhäuser Press.

Ballmer, M. D., Lourenço, D. L., Hirose, K., Caracas, R., and Nomura, R. (2017). Reconciling magma-ocean crystallization models with the present-day structure of the Earth's mantle. *Geochemistry, Geophysics, Geosystems*, 18(7):2785–2806.

Barr, A. C., Dobos, V., and Kiss, L. L. (2018). Interior structures and tidal heating in the TRAPPIST-1 planets. *Astronomy & Astrophysics*, 613:A37.

Barr, A. C. and McKinnon, W. B. (2007). Convection in ice I shells and mantles with self-consistent grain size. *Journal of Geophysical Research: Planets*, 112(E2).

Battaglia, S. M., Stewart, M. A., and Kieffer, S. W. (2014). Io's theothermal (sulfur) – Lithosphere cycle inferred from sulfur solubility modeling of Pele's magma supply. *Icarus*, 235:123–129.

Beuthe, M. (2013). Spatial patterns of tidal heating. *Icarus*, 223(1):308–329.

Bierson, C. J. and Nimmo, F. (2016). A test for Io's magma ocean: Modeling tidal dissipation with a partially molten mantle. *Journal of Geophysical Research: Planets*, 121(11):2211–2224.

Biot, M. A. (1954). Theory of Stress-Strain Relations in Anisotropic Viscoelasticity and Relaxation Phenomena. *Journal of Applied Physics*, 25(11):1385–1391.

Blaney, D. L., Johnson, T. V., Matson, D. L., and Veeder, G. J. (1995). Volcanic Eruptions on Io: Heat Flow, Resurfacing, and Lava Composition. *Icarus*, 113(1):220–225.

Blöcker, A., Saur, J., Roth, L., and Strobel, D. F. (2018). MHD Modeling of the Plasma Interaction With Io's Asymmetric Atmosphere. *Journal of Geophysical Research: Space Physics*, 123(11):9286–9311.

Bolmont, E., Selsis, F., Raymond, S. N., Leconte, J., Hersant, F., Maurin, A.-S., and Pericaud, J. (2013). Tidal dissipation and eccentricity pumping: Implications for the depth of the secondary eclipse of 55 Cancri e. *Astronomy & Astrophysics*, 556:A17.

Breuer, D. and Moore, W. B. (2015). 10.08 - Dynamics and Thermal History of the Terrestrial Planets, the Moon, and Io. In Schubert, G., editor, *Treatise on Geophysics (Second Edition)*, pages 255–305. Elsevier, Oxford.

Buffo, J. J., Schmidt, B. E., Huber, C., and Walker, C. C. (2020). Entrainment and Dynamics of Ocean-Derived Impurities Within Europa's Ice Shell. *Journal of Geophysical Research: Planets*, 125(10):e2020JE006394.

Cantrall, C., de Kleer, K., de Pater, I., Williams, D. A., Davies, A. G., and Nelson, D. (2018). Variability and geologic associations of volcanic activity on Io in 2001–2016. *Icarus*, 312:267–294.

Carlson, R. W., Garnero, E., Harrison, T. M., Li, J., Manga, M., McDonough, W. F., Mukhopadhyay, S., Romanowicz, B., Rubie, D., Williams, Q., and Zhong, S. (2014). How Did Early Earth Become Our Modern World? *Annual Review of Earth and Planetary Sciences*, 42(1):151–178.

Carr, M. H., Belton, M. J. S., Chapman, C. R., Davies, M. E., Geissler, P., Greenberg, R., McEwen, A. S., Tufts, B. R., Greeley, R., Sullivan, R., Head, J. W., Pappalardo, R. T., Klaasen, K. P., Johnson, T. V., Kaufman, J., Senske, D., Moore, J., Neukum, G., Schubert, G., Burns, J. A., Thomas, P., and Veverka, J. (1998). Evidence for a subsurface ocean on Europa. *Nature*, 391(6665):363.

Carr, M. H., Masursky, H., Strom, R. G., and Terrile, R. J. (1979). Volcanic features of Io. *Nature*, 280(5725):729–733.

Clow, G. D. and Carr, M. H. (1980). Stability of sulfur slopes on Io. *Icarus*, 44(2):268–279.

Dasgupta, R. and Hirschmann, M. M. (2010). The deep carbon cycle and melting in Earth's interior. *Earth and Planetary Science Letters*, 298(1):1–13.

Davies, A. G., Gunapala, S., Soibel, A., Ting, D., Rafol, S., Blackwell, M., Hayne, P. O., and Kelly, M. (2017). A novel technology for measuring the eruption temperature of silicate lavas with remote sensing: Application to Io and other planets. *Journal of Volcanology and Geothermal Research*, 343:1–16.

Davies, A. G., Keszthelyi, L. P., and McEwen, A. S. (2016). Determination of eruption temperature of Io's lavas using lava tube skylights. *Icarus*, 278:266–278.

Davies, A. G., Veeder, G. J., Matson, D. L., and Johnson, T. V. (2015). Map of Io's volcanic heat flow. *Icarus*, 262:67–78.

de Kleer, K. and de Pater, I. (2016). Time variability of Io's volcanic activity from near-IR adaptive optics observations on 100 nights in 2013–2015. *Icarus*, 280:378–404.

de Kleer, K., de Pater, I., Davies, A. G., and Ádámkovics, M. (2014). Near-infrared monitoring of Io and detection of a violent outburst on 29 August 2013. *Icarus*, 242:352–364.

de Kleer, K., de Pater, I., Molter, E. M., Banks, E., Davies, A. G., Alvarez, C., Campbell, R., Aycock, J., Pelletier, J., Stickel, T., Kacprzak, G. G., Nielsen, N. M., Stern, D., and Tollefson, J. (2019a). Io's Volcanic Activity from Time Domain Adaptive Optics Observations: 2013–2018. *The Astronomical Journal*, 158(1):29.

de Kleer, K., McEwen, A. S., and Park, R. (2019b). Tidal Heating: Lessons from Io and the Jovian System. In *Final Report for the Keck Institute for Space Studies*.

de Kleer, K., Nimmo, F., and Kite, E. (2019c). Variability in Io's Volcanism on Timescales of Periodic Orbital Changes. *Geophysical Research Letters*, 46(12):6327–6332.

de Kleer, K., Skrutskie, M., Leisenring, J., Davies, A. G., Conrad, A., de Pater, I., Resnick, A., Bailey, V., Defrère, D., Hinz, P., Skemer, A., Spalding, E., Vaz, A., Veillet, C., and Woodward, C. E. (2017). Multi-phase volcanic resurfacing at Loki Patera on Io. *Nature*, 545(7653):199–202.

de Pater, I., Davies, A. G., Ádámkovics, M., and Ciardi, D. R. (2014). Two new, rare, high-effusion outburst eruptions at Rarog and Heno Paterae on Io. *Icarus*, 242(Supplement C):365–378.

Geissler, P. E., McEwen, A. S., Keszthelyi, L., Lopes-Gautier, R., Granahan, J., and Simonelli, D. P. (1999). Global Color Variations on Io. *Icarus*, 140(2):265–282.

Hamano, K., Abe, Y., and Genda, H. (2013). Emergence of two types of terrestrial planet on solidification of magma ocean. *Nature*, 497(7451):607–610.

Hamilton, C. W., Beggan, C. D., Still, S., Beuthe, M., Lopes, R. M. C., Williams, D. A., Radebaugh, J., and Wright, W. (2013). Spatial distribution of volcanoes on Io: Implications for tidal heating and magma ascent. *Earth and Planetary Science Letters*, 361:272–286.

Hammond, M. and Pierrehumbert, R. T. (2017). Linking the Climate and Thermal Phase Curve of 55 Cancri e. *The Astrophysical Journal*, 849(2):152.

Hammond, N. P., Parmenteir, E. M., and Barr, A. C. (2018). Compaction and Melt Transport in Ammonia-Rich Ice Shells: Implications for the Evolution of Triton. *Journal of Geophysical Research: Planets*, 123(12):3105–3118.

Havlin, C., Parmentier, E. M., and Hirth, G. (2013). Dike propagation driven by melt accumulation at the lithosphere–asthenosphere boundary. *Earth and Planetary Science Letters*, 376:20–28.

Hay, H. C. F. C., Trinh, A., and Matsuyama, I. (2020). Powering the Galilean Satellites with Moon-moon Tides. *Geophysical Research Letters*, n/a(n/a):e2020GL088317.

Hemingway, D. J. and Matsuyama, I. (2017). Isostatic equilibrium in spherical coordinates and implications for crustal thickness on the Moon, Mars, Enceladus, and elsewhere. *Geophysical Research Letters*, 44(15):7695–7705.

Hewitt, I. and Fowler, A. (2008). Partial melting in an upwelling mantle column. *Proceedings of the Royal Society A: Mathematical, Physical and Engineering Sciences*, 464(2097):2467–2491.

Hirschmann, M. M. (2018). Comparative deep Earth volatile cycles: The case for C recycling from exosphere/mantle fractionation of major (H2O, C, N) volatiles and from H2O/Ce, CO2/Ba, and CO2/Nb exosphere ratios. *Earth and Planetary Science Letters*, 502:262–273.

Jackson, M. D., Blundy, J., and Sparks, R. S. J. (2018). Chemical differentiation, cold storage and remobilization of magma in the Earth's crust. *Nature*, 564(7736):405–409.

Kagoshima, T., Sano, Y., Takahata, N., Maruoka, T., Fischer, T. P., and Hattori, K. (2015). Sulphur geodynamic cycle. *Scientific Reports*, 5(1):8330.

Kalousová, K., Souček, O., Tobie, G., Choblet, G., and Čadek, O. (2014). Ice melting and downward transport of meltwater by two-phase flow in Europa's ice shell. *Journal of Geophysical Research: Planets*, 119(3):532–549.

Katz, R. F. (2008). Magma Dynamics with the Enthalpy Method: Benchmark Solutions and Magmatic Focusing at Mid-ocean Ridges. *Journal of Petrology*, 49(12):2099–2121.

Katz, R. F. (2010). Porosity-driven convection and asymmetry beneath mid-ocean ridges. *Geochemistry, Geophysics, Geosystems*, 11(11).

Katz, R. F., Knepley, M. G., Smith, B., Spiegelman, M., and Coon, E. T. (2007). Numerical simulation of geodynamic processes with the Portable Extensible Toolkit for Scientific Computation. *Physics of the Earth and Planetary Interiors*, 163(1):52–68.

Katz, R. F. and Weatherley, S. M. (2012). Consequences of mantle heterogeneity for melt extraction at mid-ocean ridges. *Earth and Planetary Science Letters*, 335-336:226–237.

Kaula, W. M. (1964). Tidal dissipation by solid friction and the resulting orbital evolution. *Reviews of Geophysics*, 2(4):661–685.

Keane, J. T., Ahern, A., Bagenal, F., Barr Mlinar, A., Basu, K., Becerra, P., Bertrand, T., Beyer, R., Bierson, C., Bland, M., Breuer, D., Davies, A., de Kleer, K., de Pater, I., DellaGiustina, D., Denk, T., Echevarria, A., Elder, C., Feafa, L., Grava, C., Gregg, P., Gregg, T., Hamilton, C., Harris, C., Harris, W., Hay, H., Hendrix, A., Horst, S., Huang, R., Hughes, A., Jessup, K., Jia, X., Jozwiak, L., Kerber, L., Keszthelyi, L., Khurana, K. K., Kiefer, W. S., Kirchoff, M. R., Kite, E., Klaiber, L., Klima, R., Kling, C., Lainey, V., Lopes, R. M. C., Lucchetti, A., Mandt, K., Matsuyama, I., McCarthy, C., McEwen, A., McGrath, M., Montesi, L., Moses, J., Moullet, A., Nenon, Q., Neumann, G., Neveu, M., Nimmo, F., Noonan, J., Pajola, M., Panning, M., Park, R., Pommier, A., Quick, L., Radebaugh, J., Rathbun, J. A., Retherford, K. D., Roberts, J., Roussos, E., Schenk, P., Schneider, N., Schools, J., Sood, R., Spencer, J. R., Spencer, D. C., Steinbrugge, G., Sulaiman, A., Sutton, S., Trinh, A., Tsang, C., Vertesi, J., Vorburger, A., Westlake, J., and Williams, D. A. (2020). The Science Case for Io Exploration. In *A White paper to the 2023-2032 Planetary Science and Astrobiology Decadal Survey.*

Kelemen, P. B., Shimizu, N., and Salters, V. J. M. (1995). Extraction of mid-ocean-ridge basalt from the upwelling mantle by focused flow of melt in dunite channels. *Nature*, 375(6534):747–753.

Keller, T. and Katz, R. F. (2016). The Role of Volatiles in Reactive Melt Transport in the Asthenosphere. *Journal of Petrology*, 57(6):1073–1108.

Keller, T., May, D. A., and Kaus, B. J. P. (2013). Numerical modelling of magma dynamics coupled to tectonic deformation of lithosphere and crust. *Geophysical Journal International*, 195(3):1406–1442.

Keszthelyi, L., Jaeger, W., Milazzo, M., Radebaugh, J., Davies, A. G., and Mitchell, K. L.

(2007). New estimates for Io eruption temperatures: Implications for the interior. *Icarus*, 192(2):491–502.

Keszthelyi, L., Jaeger, W. L., Turtle, E. P., Milazzo, M., and Radebaugh, J. (2004). A post-Galileo view of Io's interior. *Icarus*, 169(1):271–286.

Keszthelyi, L. and McEwen, A. (1997). Magmatic Differentiation of Io. *Icarus*, 130(2):437–448.

Keszthelyi, L., McEwen, A. S., and Taylor, G. J. (1999). Revisiting the Hypothesis of a Mushy Global Magma Ocean in Io. *Icarus*, 141(2):415–419.

Khurana, K. K., Jia, X., Kivelson, M. G., Nimmo, F., Schubert, G., and Russell, C. T. (2011). Evidence of a Global Magma Ocean in Io's Interior. *Science*, 332(6034):1186–1189.

Kirchoff, M. R. and McKinnon, W. B. (2009). Formation of mountains on Io: Variable volcanism and thermal stresses. *Icarus*, 201(2):598–614.

Kirchoff, M. R., McKinnon, W. B., and Bland, M. T. (2020). Effects of faulting on crustal stresses during mountain formation on Io. *Icarus*, 335:113326.

Kirchoff, M. R., McKinnon, W. B., and Schenk, P. M. (2011). Global distribution of volcanic centers and mountains on Io: Control by asthenospheric heating and implications for mountain formation. *Earth and Planetary Science Letters*, 301(1):22–30.

Kurz, M. D., Jenkins, W. J., and Hart, S. R. (1982). Helium isotopic systematics of oceanic islands and mantle heterogeneity. *Nature*, 297(5861):43–47.

Lainey, V. (2016). Quantification of tidal parameters from Solar System data. *Celestial Mechanics and Dynamical Astronomy*, 126(1):145–156.

Lainey, V., Arlot, J.-E., Karatekin, Ö., and Van Hoolst, T. (2009). Strong tidal dissipation in Io and Jupiter from astrometric observations. *Nature*, 459(7249):957–959.

Lammer, H., Zerkle, A. L., Gebauer, S., Tosi, N., Noack, L., Scherf, M., Pilat-Lohinger, E., Güdel, M., Grenfell, J. L., Godolt, M., and Nikolaou, A. (2018). Origin and evolution of the atmospheres of early Venus, Earth and Mars. *The Astronomy and Astrophysics Review*, 26(1):2.

Lichtenberg, T., Keller, T., Katz, R. F., Golabek, G. J., and Gerya, T. V. (2019). Magma ascent in planetesimals: Control by grain size. *Earth and Planetary Science Letters*, 507:154–165.

Lopes, R. M. C. and Spencer, J. R. (2007). *Io After Galileo - A New View of Jupiter's Volcanic Moon*. Springer, Berlin.

Lourenço, D. L., Rozel, A. B., Gerya, T., and Tackley, P. J. (2018). Efficient cooling of rocky planets by intrusive magmatism. *Nature Geoscience*, 11(5):322.

Mallik, A., Li, Y., and Wiedenbeck, M. (2018). Nitrogen evolution within the Earth's atmosphere–mantle system assessed by recycling in subduction zones. *Earth and Planetary Science Letters*, 482:556–566.

Manga, M. and Wang, C.-Y. (2007). Pressurized oceans and the eruption of liquid water on Europa and Enceladus. *Geophysical Research Letters*, 34(7).

McEwen, A. S., Keszthelyi, L., Spencer, J. R., Schubert, G., Matson, D. L., Lopes-Gautier, R., Klaasen, K. P., Johnson, T. V., Head, J. W., Geissler, P., Fagents, S., Davies, A. G., Carr, M. H., Breneman, H. H., and Belton, M. J. S. (1998). High-Temperature Silicate Volcanism on Jupiter's Moon Io. *Science*, 281(5373):87–90.

McGovern, P. J. and Schubert, G. (1989). Thermal evolution of the Earth: effects of volatile exchange between atmosphere and interior. *Earth and Planetary Science Letters*, 96(1):27–37.

McKenzie, D. (1984). The Generation and Compaction of Partially Molten Rock. *Journal of Petrology*, 25(3):713–765.

McKinnon, W. B., Schenk, P. M., and Dombard, A. J. (2001). Chaos on Io: A model for formation of mountain blocks by crustal heating, melting, and tilting. *Geology*, 29(2):103–106.

Moore, W. B. (2001). The Thermal State of Io. *Icarus*, 154(2):548–550.

Moore, W. B. (2003). Tidal heating and convection in Io. *Journal of Geophysical Research: Planets*, 108(E8):5096.

Moore, W. B., Schubert, G., Anderson, J. D., and Spencer, J. R. (2007). The Interior of Io. In *Io After Galileo: A New View of Jupiter's Volcanic Moon*, pages 89–108. Springer, Berlin.

Moore, W. B., Simon, J. I., and Webb, A. A. G. (2017). Heat-pipe planets. *Earth and Planetary Science Letters*, 474:13–19.

Moore, W. B. and Webb, A. A. G. (2013). Heat-pipe Earth. *Nature*, 501(7468):501–505.

Morabito, L. A., Synnott, S. P., Kupferman, P. N., and Collins, S. A. (1979). Discovery of Currently Active Extraterrestrial Volcanism. *Science*, 204(4396):972–972.

Moretti, R. and Baker, D. R. (2008). Modeling the interplay of fO2 and fS2 along the FeS-silicate melt equilibrium. *Chemical Geology*, 256(3):286–298.

Murray, C. D. and Dermott, S. F. (2000). *Solar System Dynamics.* Cambridge University Press, Cambridge.

Nimmo, F. (2004). Non-Newtonian topographic relaxation on Europa. *Icarus*, 168(1):205–208.

Nimmo, F. and Stevenson, D. J. (2001). Estimates of Martian crustal thickness from viscous relaxation of topography. *Journal of Geophysical Research: Planets*, 106(E3):5085–5098.

O'Reilly, T. C. and Davies, G. F. (1981). Magma transport of heat on Io: A mechanism allowing a thick lithosphere. *Geophysical Research Letters*, 8(4):313–316.

Pahlevan, K. and Stevenson, D. J. (2007). Equilibration in the aftermath of the lunar-forming giant impact. *Earth and Planetary Science Letters*, 262(3–4):438–449.

Peale, S. J., Cassen, P., and Reynolds, R. T. (1979). Melting of Io by Tidal Dissipation. *Science*, 203(4383):892–894.

Quick, L. C. and Marsh, B. D. (2016). Heat transfer of ascending cryomagma on Europa. *Journal of Volcanology and Geothermal Research*, 319:66–77.

Radebaugh, J., Keszthelyi, L. P., McEwen, A. S., Turtle, E. P., Jaeger, W., and Milazzo, M. (2001). Paterae on Io: A new type of volcanic caldera? *Journal of Geophysical Research: Planets*, 106(E12):33005–33020.

Rathbun, J. A., Lopes, R. M. C., and Spencer, J. R. (2018). The Global Distribution of Active Ionian Volcanoes and Implications for Tidal Heating Models. *The Astronomical Journal*, 156(5):207.

Rees Jones, D. W. and Katz, R. F. (2018). Reaction-infiltration instability in a compacting porous medium. *Journal of Fluid Mechanics*, 852:5–36.

Renaud, J. P. and Henning, W. G. (2018). Increased Tidal Dissipation Using Advanced Rheological Models: Implications for Io and Tidally Active Exoplanets. *The Astrophysical Journal*, 857(2):98.

Roberts, J. H. and Nimmo, F. (2008). Tidal heating and the long-term stability of a subsurface ocean on Enceladus. *Icarus*, 194(2):675–689.

Ross, M. N., Schubert, G., Spohn, T., and Gaskell, R. W. (1990). Internal structure of Io and the global distribution of its topography. *Icarus*, 85(2):309–325.

Roth, L., Saur, J., Retherford, K. D., Blöcker, A., Strobel, D. F., and Feldman, P. D. (2017). Constraints on Io's interior from auroral spot oscillations. *Journal of Geophysical Research: Space Physics*, 122(2):1903–1927.

Rubie, D. C., Laurenz, V., Jacobson, S. A., Morbidelli, A., Palme, H., Vogel, A. K., and Frost, D. J. (2016). Highly siderophile elements were stripped from Earth's mantle by iron sulfide segregation. *Science*, 353(6304):1141–1144.

Rudge, J. F. (2018). The Viscosities of Partially Molten Materials Undergoing Diffusion Creep. *Journal of Geophysical Research: Solid Earth*, 123(12):10,534–10,562.

Rudge, J. F., Bercovici, D., and Spiegelman, M. (2011). Disequilibrium melting of a two phase multicomponent mantle. *Geophysical Journal International*, 184(2):699–718.

Sabadini, R. and Vermeersen, B. (2004). *Global Dynamics of the Earth: Applications of Normal Model Relaxation Theory to Solid-Earth Geophysics*. Kluwer Academic Publishers, Dordrecht.

Sagan, C. (1979). Sulphur flows on Io. *Nature*, 280(5725):750–753.

Schenk, P. M. and Bulmer, M. H. (1998). Origin of Mountains on Io by Thrust Faulting and Large-Scale Mass Movements. *Science*, 279(5356):1514–1517.

Segatz, M., Spohn, T., Ross, M. N., and Schubert, G. (1988). Tidal dissipation, surface heat flow, and figure of viscoelastic models of Io. *Icarus*, 75(2):187–206.

Smith, B. A., Soderblom, L. A., Johnson, T. V., Ingersoll, A. P., Collins, S. A., Shoemaker, E. M., Hunt, G. E., Masursky, H., Carr, M. H., Davies, M. E., Cook, A. F., Boyce, J., Danielson, G. E., Owen, T., Sagan, C., Beebe, R. F., Veverka, J., Strom, R. G., Mccauley, J. F., Morrison, D., Briggs, G. A., and Suomi, V. E. (1979). The Jupiter System Through the Eyes of Voyager 1. *Science*, 204(4396):951–972.

Sohl, F., Spohn, T., Breuer, D., and Nagel, K. (2002). Implications from Galileo Observations on the Interior Structure and Chemistry of the Galilean Satellites. *Icarus*, 157(1):104–119.

Sparks, D. W. and Parmentier, E. M. (1991). Melt extraction from the mantle beneath spreading centers. *Earth and Planetary Science Letters*, 105(4):368–377.

Spencer, D. C., Katz, R. F., and Hewitt, I. J. (2020a). Magmatic Intrusions Control Io's Crustal Thickness. *Journal of Geophysical Research: Planets*, 125(6):e2020JE006443.

Spencer, D. C., Katz, R. F., and Hewitt, I. J. (2021). Tidal controls on the lithospheric thickness and topography of Io from magmatic segregation and volcanism modelling. *Icarus*, 359:114352.

Spencer, D. C., Katz, R. F., Hewitt, I. J., May, D. A., and Keszthelyi, L. P. (2020b). Compositional Layering in Io Driven by Magmatic Segregation and Volcanism. *Journal of Geophysical Research: Planets*, 125(9):e2020JE006604.

Spencer, J. R. and Nimmo, F. (2013). Enceladus: An Active Ice World in the Saturn System. *Annual Review of Earth and Planetary Sciences*, 41(1):693–717.

Spencer, J. R., Rathbun, J. A., Travis, L. D., Tamppari, L. K., Barnard, L., Martin, T. Z., and McEwen, A. S. (2000). Io's Thermal Emission from the Galileo Photopolarimeter-Radiometer. *Science*, 288(5469):1198–1201.

Spiegelman, M. (1993). Flow in deformable porous media. Part 2 Numerical analysis – the relationship between shock waves and solitary waves. *Journal of Fluid Mechanics*, 247:39–63.

Steinke, T., Hu, H., Höning, D., van der Wal, W., and Vermeersen, B. (2020). Tidally induced lateral variations of Io's interior. *Icarus*, 335:113299.

Stevenson, D. J. (2000). Limits on the variation of thickness of Europa's ice shell. In *31st Lunar and Planetary Science Conference*, volume 1506.

Tackley, P. J. (2001). Convection in Io's asthenosphere: Redistribution of nonuniform tidal heating by mean flows. *Journal of Geophysical Research: Planets*, 106(E12):32971–32981.

Tackley, P. J., Schubert, G., Glatzmaier, G. A., Schenk, P., Ratcliff, J. T., and Matas, J.-P. (2001). Three-Dimensional Simulations of Mantle Convection in Io. *Icarus*, 149(1):79–93.

Tobie, G., Mocquet, A., and Sotin, C. (2005). Tidal dissipation within large icy satellites: Applications to Europa and Titan. *Icarus*, 177(2):534–549.

Turcotte, D. and Schubert, G. (2014). *Geodynamics*. Cambridge University Press, Cambridge, 3 edition.

Turner, A. J., Katz, R. F., Behn, M. D., and Keller, T. (2017). Magmatic Focusing to Mid-Ocean Ridges: The Role of Grain-Size Variability and Non-Newtonian Viscosity. *Geochemistry, Geophysics, Geosystems*, 18(12):4342–4355.

Tyler, R. H., Henning, W. G., and Hamilton, C. W. (2015). Tidal Heating in a Magma Ocean within Jupiter's Moon Io. *The Astrophysical Journal Supplement Series*, 218(2):22.

Van Hoolst, T., Baland, R.-M., Trinh, A., Yseboodt, M., and Nimmo, F. (2020). The Librations, Tides, and Interior Structure of Io. *Journal of Geophysical Research: Planets*, 125(8):e2020JE006473.

Veeder, G. J., Davies, A. G., Matson, D. L., Johnson, T. V., Williams, D. A., and Radebaugh, J. (2012). Io: Volcanic thermal sources and global heat flow. *Icarus*, 219(2):701–722.

White, O. L., Schenk, P. M., Nimmo, F., and Hoogenboom, T. (2014). A new stereo topographic map of Io: Implications for geology from global to local scales. *Journal of Geophysical Research: Planets*, 119(6):1276–1301.

Williams, D. A., Keszthelyi, L. P., Crown, D. A., Yff, J. A., Jaeger, W. L., Schenk, P. M., Geissler, P., and Becker, T. L. (2011). Volcanism on Io: New insights from global geologic mapping. *Icarus*, 214(1):91–112.

Williams, D. A., Wilson, A. H., and Greeley, R. (2000). A komatiite analog to potential ultramafic materials on Io. *Journal of Geophysical Research: Planets*, 105(E1):1671–1684.

Zolotov, M. Y. and Fegley, B. (1999). Oxidation State of Volcanic Gases and the Interior of Io. *Icarus*, 141(1):40–52.